"A New and Generic Two-Dimensional Model for Studying Channeling Radiation with Relativistic Electron Beams"

By

Wade D. Rush

Submitted to the graduate degree program in the Department of Physics and the
Graduate Faculty of the University of Kansas
in partial fulfillment of the requirements for the degree of
Doctor of Philosophy

Committee members

Jack Shi, Chairperson

Graham Wilson

Siyuan Han

Wai-Lun Chan

James Miller, EECS

Date defended: April 28, 2017

The Dissertation Committee for Wade D. Rush certifies
that this is the approved version of the following dissertation :

"A New and Generic Two-Dimensional Model for Studying Channeling Radiation with Relativistic Electron Beams"

Jack Shi, Chairperson

Date approved: May 8, 2017

Abstract

In 2016, Fermilab Accelerator and Technology Facility (FAST) conducted an experiment to generate a discrete and potentially tunable hard X-ray channeling radiation emissions in the 40 - 150 KeV energy range using a new 50 MeV rated linear accelerator. There are two current models (one-dimensional (1-D) Planar and the two-dimensional (2-D) Axial model) that numerically simulate the physics involved in generating channeling radiation. FAST decided to use the 1-D Planar model in designing the experiment using a diamond crystal lattice with a (110) plane orientation. However, this study shows that the 1-D Planar model is fraught with inconsistencies and applies excessive approximations. Using this approach will obfuscate the analysis in properly identifying the mechanisms that generate these discrete energy emissions. The 2-D Axial model would be a much better model to properly predict spectrum emission energies. However, the 2-D Axial model is complex and appears to also contain unnecessary approximations as well. This study's goal was to develop a better 2-D Generic model for the experiment based on a more fundamental and accurate approach than the existing 2-D Axial model. Unfortunately, the FAST experiment was unable to generate channeling radiation data. Thus, this study had to compare its 2-D Generic model predictions with published experimental results that were based on the 2-D Axial model. Our 2-D Generic model produced a rich amount of spectrum. But, ultimately, it had poor agreement with these published experimental data results. On the other hand, the 2-D Axial model provided very good agreement with their published experimental data. The failure for this new 2-D Generic model indicates two possibilities. First, the accelerator's electron beam distribution of the transverse mo-

mentum to the beam direction directly impacts spectrum data. In all published results, this beam transverse momentum distribution is unknown. Therefore, if this transverse momentum distribution was published, then a more definitive conclusion can be made on whether this model agrees with the published experimental data or not. Second, since this model is based on a more fundamental concept, the 2-D Generic model should have very good agreement. However, since the model is unable to accurately predict discrete channeling emission energies, this discrepancy indicates that there are perhaps additional mechanisms unaccounted for in the generation of channeling radiation.

Acknowledgements

I want to thank my super wife, Sarah who is also a PhD Physic candidate, for all her help and patience with my idiosyncrasies. Thanks to my less than two year old daughter, Vera Irene Scout, who provides me the impetus to continue.

I would also like to extend my thanks to Tanaji Sen and Philippe Piot for allowing me to participate in the channeling experiment conducted at the FAST facility at Fermilab.

Without the integral support from Hume Feldman, Steve Sanders and Greg Rudnick from the KU Physics department, my successful completion of the PhD would not of occurred. To you three gentlemen, I thank you from the bottom of my heart.

And lastly and most importantly, Jack Shi, my advisor, for not giving up on me although his application of Socratic methods generated uncountably many heated arguments over various obscure physics problems. Jack, I feel very fortunate to have worked with you and to have learned from the very best. It has been a fun and challenging endeavor.

Contents

List of Figures

List of Tables

Chapter 1

Introduction

There has been over several years a push in physics in generating high energy light sources such as SLACs Linac Coherent Light Source and Jefferson Lab's Free-Electron Laser to name a few [11, 12]. The ability to generate such high energy light sources such as hard X-rays has a potential for numerous applications in industry. SLAC and Jefferson's facilities have large infrastructures to produce these light sources. However, other promising high energy light sources such as PXR [13] and Channeling radiation produced from an accelerated beam interacting with a crystal lattice at some specific orientation only require small compact infrastructure for prototype development. Potentially, these infrastructures that generate PXR or Channeling radiation could be reduced down in size to compact, portable high energy light sources. Because of the potential for having a high return for its value, Fermilab Accelerator Science and Technology (FAST) facility conducted an experiment to produce channeling radiation with beam energies at around 40 to 45 MeV using a diamond with a (110) planar orientation.

If a relativistic electron traveling along a direction is nearly aligned with a specific orientation of the crystal, it will channel through the crystal rather than generating Bremsstrahlung from random interactions with ions located within the crystal. This electron channeling through the crystal generates discrete energy emissions which is called channeling radiation. When the electron's alignment angle with the crystal's defined lattice orientation is small enough, the electron's

momentum can be projected into two components: $p_{\parallel}$ to $p_{\perp}$ where $p_{\parallel}$ is aligned exactly with the defined crystal lattice orientation. The transverse kinetic energy, $p_{\perp}^2/2\gamma m$, where gamma is the Lorentz relativistic factor and m is the mass of the electron, is small enough to become bounded within the transverse potential which is perpendicular to the crystal orientation. While transiting through the crystal, these transverse bounded electron eigenstates decay to lower energies which then generate hard X-rays in the 10KeV to 150KeV range and even higher depending on the electron's energy.

Through the course of this research, we have found that there are basically two existing models (one-dimensional Planar model and two-dimensional Axial model) that are based on Lindhard's explanation for channeling radiation [14]. The one-dimensional (1-D) Planar model is considered a separate and distinct model from the two-dimensional (2-D) Axial model. Both predict channeling radiation but the physics required to generate the transverse potential which bounds the electron's transverse motion are based on different phenomenological reasons.

Because there exist a working numerical Mathematica program that was based on the 1-D Planar model[15], the channeling experiment at FAST then based its design on the 1-D Planar model. However, this research submits that the 1-D Planar model is inconsistent an applies unnecessary approximations in predicting the discrete channeling radiation emission energies. In fact, in using the 1-D Planar model, it is unclear what specific mechanism is generating the discrete emissions. Hence, data collected and the subsequent data analysis viability are suspected. On the other hand, the 2-D Axial model is a much better model; but it is too complex and also incorporates unnecessary approximation although less severely then the 1-D Planar model. Because of this, the main goal of this research was to develop a more accurate 2-D Generic model in predicting channeling radiation.

Since the experiment at FAST was unable to generate channeling radiation data, this research had to use previous published experimental findings that were based on the 2-D Axial model. To measure the adequacy of our new model, we used these published data to compare with our model's prediction. The 2-D Generic Model was based on a more fundamental approach and also a more

accurate calculation as compared to the existing 2-D Axial approach. Therefore, we expected to see very good agreements with published experimental data. However, this was found not to be true. In fact, compared to our 2-D Generic model, the legacy 2-D Axial model had very good agreement to experimental data. Our model appeared to have very poor to inadequate agreements to these same published experimental data.

There are possibly two general reasons for this new 2-D Generic model failing to agree with experimental data. The 2-D Generic model produced a rich spectrum. However, for channeling radiation, the spectrum is highly dependent on the accelerator's electron beam momentum distribution. Specifically, the distribution of the transverse momentum to the beam's direction directly impacts the probability that the beam occupies certain bound channeling states. In all the public data, the beam's transverse momentum distribution is unknown. Hence, without knowing this distribution, it is not clear yet whether our 2-D Generic model is valid or not. Second, assuming that beam transverse momentum distribution is not the problem, it is surprising that this 2-D Generic model fails to agree with the experimental data. This new model is based on very fundamental physics and avoids unnecessary approximations. Yet, the legacy 2-D Axial model is apparently the better model. This discrepancy implies that some additional physics in generating channeling radiation is perhaps missing.

Finally, during this research, this study also focused on calibrating the high energy photon detector, X123CdTe made by AMPTEK. The procedures used and the problems that arose with calibrating the detector for channeling experiments maybe relevant for other experimentalist in this area. In particular, characterizing this particular detector's saturation as it relates to channeling or similar PXR experiments may also be useful.

Chapter 2

Background

2.1 Background

This study is about electrons, transported within an accelerator beam moving in a specific beam direction with relativistic speeds, colliding with a crystal lattice located in the beam path. Since the crystal lattice has a specific structure, the ions located within the structure can have a common axis or a common plane. Since the lattice is also periodic, a specifically defined plane of ions or a specifically defined axis of ions are nearly infinite in number. Consequently, the infinite number of planes are periodic in position with each other. This periodicity structure also applies to the axis of ions or just individual ions within the lattice. Since these planes or axes are well known and defined, we can align the beam direction to be parallel to a specific axis direction within the lattice structure. The specific crystal lattice axis or plane alignment with the beam's direction is called the crystal orientation. If the beam direction is nicely aligned with certain lattice orientations and the electron's transverse momentum perpendicular to the beam direction is small enough, then the beam electrons, called a bunch, will channel through the crystal rather than colliding with the ions and creating Bremsstrahlung radiation. Instead, the electrons channeling through the crystal create discrete, highly coherent and energetic photon radiation emissions called channeling radiation. Lindhard's paper in the 1960s provided an initial classical approach in explaining these coherent radiation emissions [14]. However, later studies have shown that quantum mechanisms better

explains the physics in producing the channeling radiation spectrum's specific line energies and width.

Within a crystal lattice, depending on the lattice structure's geometry, a number of ions within that unit lattice can lie on a common plane. Or, more specifically, a number of ions could lie on a common line, generally called a Single-String of ions, with a specific direction designated as an 2-D Axial direction $[hkl]$. Figure 2.1 illustrates three lattice plane orientations of interest in this study: (100), (110), and (111) planes that these ions could lie on. Or, more specifically, the ions could lie on specific lines having directions $[hkl]$ as depicted in Figure 2.2.

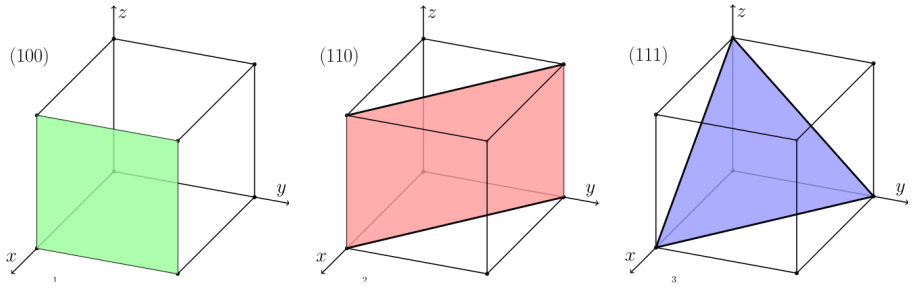

Figure 2.1: Using the miller indices, these three plots describe (hkl) plane. The three most important planes of interest in this study and depicted in this figure are the (100), (110) and the (111) planes.

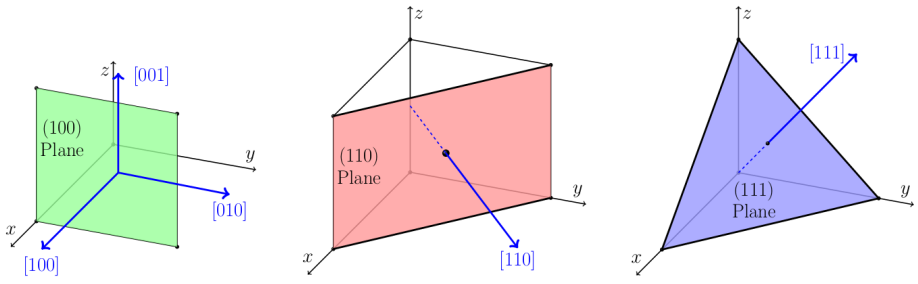

Figure 2.2: Using the miller indices, these three plots describe which [hkl] axis or 2-D Axial vectors is perpendicular to the (hkl) plane. The three most important 2-D Axial vectors of interest in this study and depicted in this figure are the [100], [110] and the [111] axial vectors. Note, the axial vector [001] depicted above would be perpendicular to the (001) plane.

Per convention, a plane is defined as (hkl) and a line with a direction is defined as $[hkl]$ where h, k, and l are integers. The symbol [hkl] is also called and axial vector.

In order to understand the merits of this study's approach in determining channeling radiation, this chapter requires a review of the conventional thoughts and approaches that explain the underlying physics of explaining channeling radiation. Unfortunately, these explanations may have shackled any further progress in this area. In our study, we are not shackled by conventional thought. Consequently, we can provide a more precise approach in explaining the physics and in numerically solving the channeling radiation. This review of the background specifically focuses on the well known and often used two-dimensional axial channeling model method which is both applied and explained in Andersen, Klein and Chouffani's papers. This study specifically compares its model, the two-dimensional model, against the 2-D Axial channeling models approach.

2.2 2D Axial Model Methodology in Determining Channeling Radiation [1], [2], [3]

Before discussing this study's approach for calculating channeling radiation, a short discussion is required to illustrate the 2D axial model view towards solving channeling radiation. Linhard's hypothesis initially revolved around the affects on an incident electron interacting with a single-string of ion's that lie on a common line with an axial direction $[hkl]$ [14]. The string of ion charges is approximated as a continuous charge along the string's axial direction. If the electron's direction of motion was primarily parallel to the single-string axial direction, the transverse motion of the electron could be in a bound state from the potential generated from the continuous line charge. This continuous positively charged axial line generates what is conventionally called the axial continuum potential. More precisely, the single-string axial potential is a radially symmetric potential perpendicular to the axial line charge. Figure 2.3 shows the string of blue ion positions along a line direction $[hkl]$ conventionally called an axial direction. The blue hash marks simulate the positive ion charges that are smeared along the line containing the single-string of ions to create a continuum line charge. The potential V, generated from this continuum charged line is a field transverse to the axial direction. V can be expressed as $V(x,y)$ where x, y are such that $\hat{x}$ and $\hat{y}$

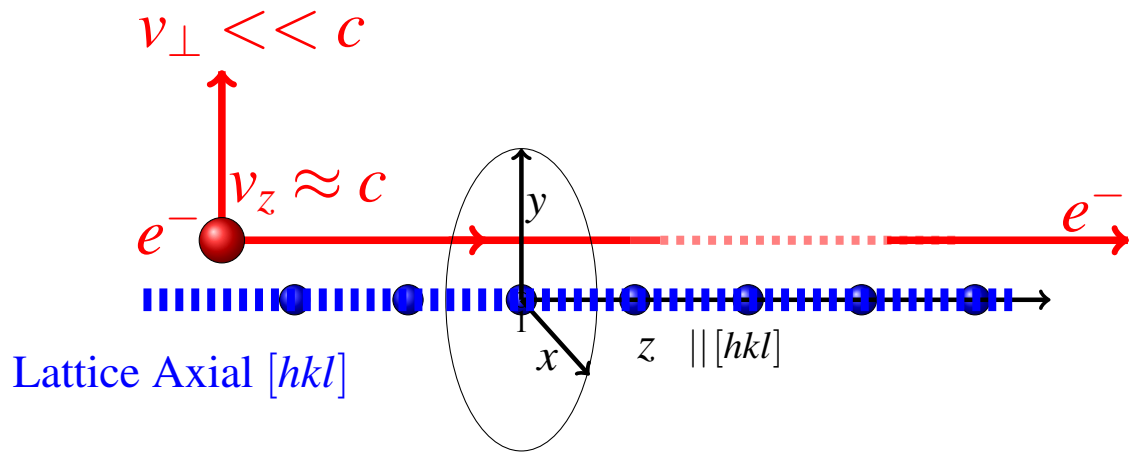

Figure 2.3: The blue circles represents a string of ions along a line or Single-String of Ions. The hashed blue line which overlays on top of the ions approximates the continuum charge of the line if all the ion charges were smeared along the line having an axial [hkl] direction. This continuum charge along the [hkl] lines creates a rotationally symmetric potential transverse to [hkl]. The electron with $V_z \parallel [hkl]$ and a transverse velocity $V_\perp$ which is perpendicular to [hkl] interacts with the rotationally symmetric potential generated by the continuum charge.

are perpendicular to $[hkl]$. Or, V is expressed in polar coordinates as $V(\vec{r}_\perp, \theta)$ where $\vec{r}_\perp(x,y)$ is perpendicular to $[hkl]$. Since the electron beam direction, $\hat{z}$ is parallel to the defined axial direction, the potential's z dependency is insignificant when compared to the projected relativistic beam's kinetic energy along the z-axis. This dependency is then conveniently averaged out along the z-axis.

A key parameter used in Lindhard's approach is the critical angle between the incident electron direction and the axial Single-String (S-S) direction $[hkl]$. In order for the electron's motion in the transverse direction to be bounded, the transverse kinetic energy of the electron, $\frac{m|\vec{v}_\perp|^2}{2}$, must be less than the magnitude of the axial S-S transverse potential. Expressed in terms of the electron momentum's magnitude $P = |\vec{P}|$ and the critical angle, θ_c, the bounded states must satisfy

$$\frac{P^2\theta_c^2}{2m} \leq |V(x,y)| = |V(r,\phi)| \tag{2.1}$$

where $\tan(\theta) \approx \theta \approx P_\perp / P_\parallel$ and θ is the angle between $vecP$ and $\vec{P}_\parallel$. The electron momentum is $\vec{P} = \vec{P}_\perp + \vec{P}_\parallel$ where $\vec{P}_\perp$ is the transverse component and $\vec{P}_\parallel$ is the longitudinal component relative to the $[hkl]$ axial direction. Since only the electron momentum's longitudinal component is relativistic,

$P_\perp << P_\parallel \approx P$ is satisfied. Therefore, the critical angle,

$$\theta_c \approx \frac{P_\perp}{P} \tag{2.2}$$

must be small enough to ensure a transverse state is bound for channeling condition. The radiation induced from the decay from a higher bound state to a lower bound state is referred to as the two dimensional (2-D) $[hkl]$ Axial model approximation of channeling radiation. From this two dimensional (2-D) $[hkl]$ axial potential, the decay from a higher bound state to a lower bound state is the generated discrete channeling radiation.

Since this is a lattice structure, there naturally exist multiple S-S continuous line charges located within a cubic lattice cell. Figure 2.4 illustrates multiple axial S-S in a cubic cell and the geometry between adjacent S-S's and electron beam direction. Note, the electron beam's $\hat{z}$ component or longitudinal direction is defined as the beam direction and is parallel to $[hkl]$. In this 2-D Axial model approach, they chose to construct a new coordinate system based on the $[hkl]$ lattice orientation to describe the lattice and its corresponding potential. From this new coordinate construction, determining the periodicity lengths and subsequently the reciprocal lattice vectors is not a trivial process.

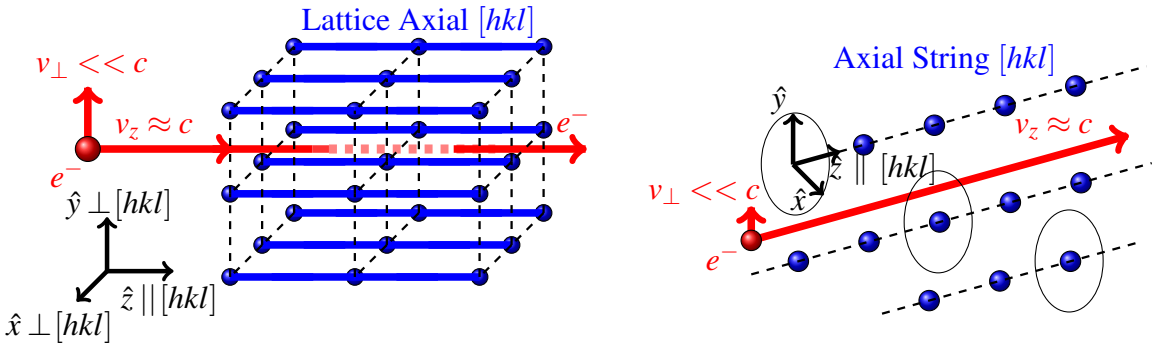

Figure 2.4: On the left figure, the electron depicted in red is entering a lattice of continuum charge of Single-String of ions with a relativistic $v_z \perp [hkl]$. The right figure shows how this same electron, in red, must interact with three of the Single-String ions within the lattice which are each generating rotational symmetric potentials.

A similar approach is applied for ions that lie on the same (hkl) plane. The ions' positive charge are smeared uniformly over the plane within the cubic cell. The positively charged plane in turn generates a potential field dependent only on the coordinate axis which is perpendicular to that (hkl) plane. Again, relative to the plane's orientation, the new coordinate system is constructed and the determination of periodicity lengths and reciprocal lattice vectors suffer the same nontrivial difficulties as the 2-D Axial model. Like the S-S axial $[hkl]$ configuration, Figure 2.5 depicts an

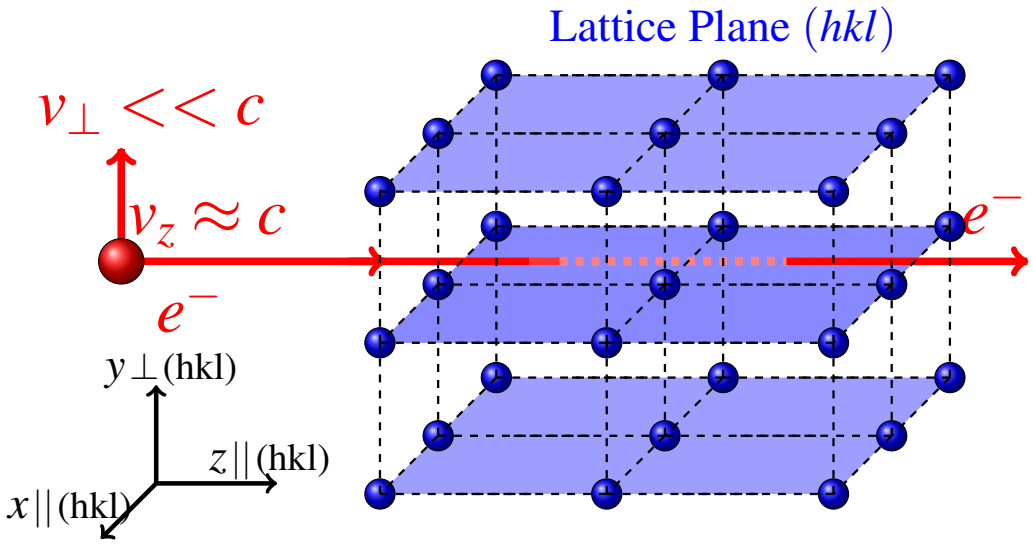

Figure 2.5: The red ball represents the electron traveling along relativistic $v_z \parallel (hkl)$ plane. The blue ba
sents ions located on a common blue plane. The blue plane represents the ions charged smeared uniform
plane to approximate a continuum charged (hkl) plane. The potential generated from a plane is only d
on the perpendicular distance from the plane.

electron incident on a crystal relative to a specific (hkl) plane containing ions. Using the same line of reasoning, if the critical angle parameter, θ_c is small enough to satisfy $\frac{P^2\theta_c^2}{2m} \leq |V(y)|$, then existing transverse bound electron states will eventually decay thus generating channeling radiation. Since the crystal is a lattice, there are also multiple approximated charge planes set periodically which the electron must also interact with collectively. The radiation induced from the decay from a higher bound state to a lower bound state is referred to as the one-dimensional (1D) planar approximation of channeling radiation.

In both the 1-D Planar and 2-D Axial model approximations, the 2-D Axial model approximation should be the more accurate model. In the 2-D Axial approximation, the lattice interaction

potential with the electron beam is a function of the transverse coordinates x and y, V(x,y). On the other hand, the planar potential is a function of a single coordinate, y, V(y). Reducing to just one coordinate indicates loss of information and thus a less accurate approximation of the channeling radiation production. Therefore, the focus of this paper is primarily to construct a two-dimensional potential that recognizes the value of the lattice orientation but dispenses with the artificial construction of Single String lattice or planar lattices to generate channeling radiation.

For clarity, this study identifies five authors that basically apply the same approach in numerically calculating both the planar and 2-D Axial approximation of channeling radiation. In the 1960s, Lindhard developed a classical approach for approximating both 2-D Axial and 1-D Planar radiation using the physical constructs discussed earlier. Later, in the 1970's, this 2-D Axial/1-D Planar construct could be more properly modeled using quantum mechanics to predict channeling radiation's discrete emissions at low beam energies. From 1981 to 1999, several papers applying nearly the same numerical quantum mechanics calculation have successfully approximated both planar and 2-D Axial channeling radiation. Specifically, Andersen papers [1, 16, 17], Klein's paper [2] which cites Andersen's works, Chouffani paper [9], which also cites Andersen's papers and Genz paper [5] which cites Kleins paper, all developed what this dissertation refers to as the 2-D Axial-Planar model approach in numerically calculating both planar and 2-D Axial approximation of channeling radiation. As recently as in 2006, Azadegan [4] applied successfully this same planar approach in calculating the planar approximation of the channeling radiation.

Although the 2-D Axial model approximation should reflect the physics of the channeling radiation production more accurately, planar approximations appear to be utilized more often. There are by far more papers that discuss planar calculations than 2-D Axial calculations. As recently as 2016, Fermilab's FAST facility relied on 1-D Planar approximation to guide the analysis of their experiment's channeling radiation spectrum. This study suggests that our two dimensional approximation should be the algorithm of choice in calculating channeling radiation spectrum. However, the 2-D Axial channeling model approximation referred to in this paper is overly structured, inflexible, and contains inadequate approximations. Our study's two dimensional approach is not

shackled by these limitations.

2.3 Proposed More Fundamental and Universal 2D Approach towards Determining Channeling Radiation

Lattice crystalsstructure, periodicity, lattice constants and etc. are well defined in the original coordinate system. In turn, with these well defined parameters, the calculation of the lattice's three dimensional interaction potential in its original coordinates is straight forward and simple. Since lattices are periodic, we can easily Fourier expand the lattice potential in terms of the lattice's well defined reciprocal lattice vectors in the original coordinate system. However, the lattice 3-D potentials expressed in the original coordinate system are generally not posed to adequately determine the transverse potential relative to the beam's direction. Generally, the beam's direction is out of alignment with the original lattice coordinate system such as figure 2.6 (a). But, the beam direction by design, is aligned with a specific plane or axial alignment of ions, Fig. 2.6 (b). Therefore, to get the beam coordinates aligned with the specific lattice plane or axial direction, we apply rotations to the original lattice coordinate system to align with the beam's curvilinear coordinate system.

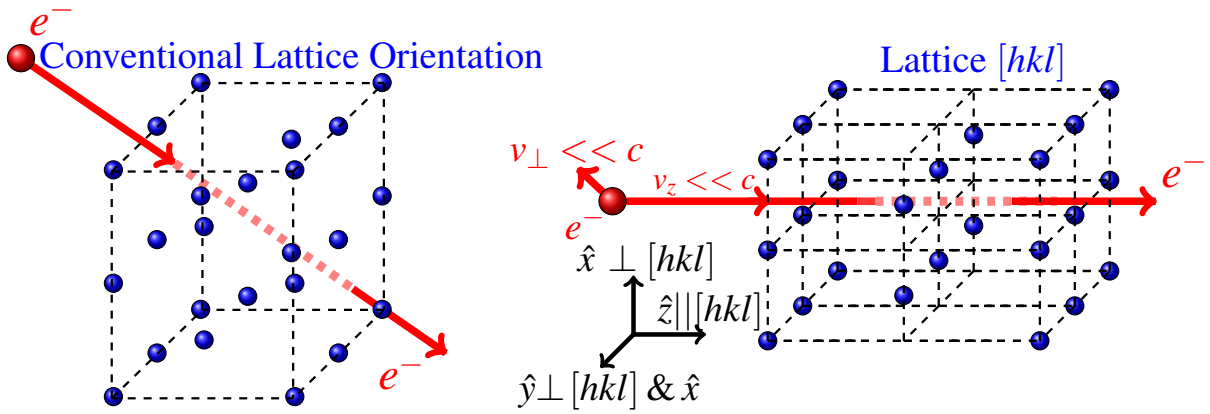

Figure 2.6: Fig. 2.6(a) depicts the incident electron depicted in red arriving out of alignment with the original lattice coordinate axes. Fig. 2.6(b) shows after rotation, the electron direction, the new lattice coordinates, and the ion structure are all conveniently aligned. In both figures 2.6(a) and 2.6(b), blue balls indicate ions at fixed locations within the lattice.

As Lindhard recognized, the structure of ions within the lattice can generate unique transverse potentials relative to the electron beam's direction.

At this point we modify slightly on how to look at the physics of channeling radiation. At relativistic speeds along the z direction $[hkl]$, the crystal length along the z-axis contracts from the electron's perspective. Figures 2.7a through 2.7d describes this Lorentz contraction of the crystal lengths along $z_{[hkl]}$ as the electron approaches the speed of light, c. Eventually, the three dimensional lattice pancakes down into a two dimensional lattice which is transverse to $z_{[hkl]}$ direction. In figure 2.7.a, we can see that both the left and right vertical planes have the same periodicity of ions in both the x and y direction. On the other hand, the center plane exhibits a larger ion periodicity in the y direction. As the beam approaches c, the lattice contracts along the $z_{[hkl]}$ until all three planes merge into one single plane, Fig. 2.7.d. The contracted ions either merge into a larger ion or create a fundamental change in the traverse lattice periodicity. And, based on the same constraints discussed earlier, the lab frame generated potential's z dependency has negligible affects on the electron's motion in the $z_{[hkl]}$. Therefore, the potential of interest that generates channeling

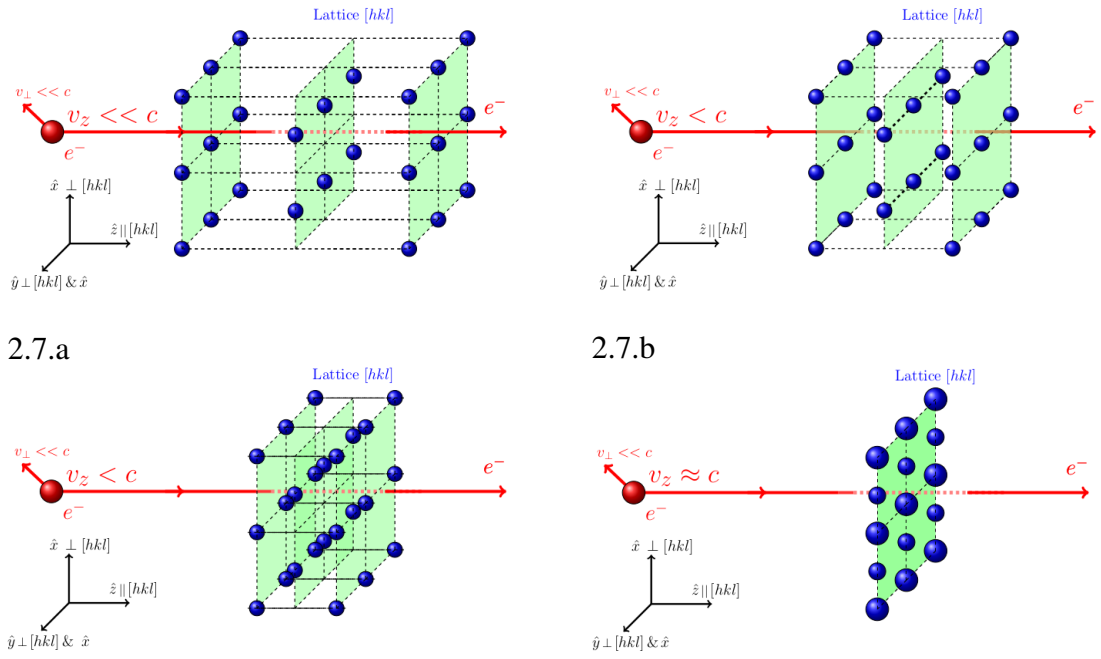

Figure 2.7: Blue dots represents the ions with the crystal. The green planes represent the transverse plane that these ions would perhaps lie on. The electron's velocity is depicted in red as a relativistic component along the longitudinal direction, $\hat{z} \parallel [hkl]$ and its perpendicular component $v_\perp \perp [hkl]$. As the electron's longitudinal [hkl] speed increases toward the speed of light from a to d, the cell contracts along [hkl] and eventually pancakes into a single transverse plane of ions. You can see that before the cell pancaked, each transverse plane had its own transverse periodicity. After cell pancakes into a single transverse plane, the periodicity has changed due to contributions from the other planes.

radiation is the transverse potential generated from pancaked lattice, $V_{[hkl]}(x,y)$. When solving the Schrödinger equation's energy band structure having this transverse potential, the fundamental periodicity of the potential defines the structure of the eigenwave functions and eigenenergies. These transverse eigenwave functions, $\psi^n(x,y)$ are Bloch waves where n represents the n_{th} eigenstate and reside within this pancaked periodic transverse structured plane, depicted in Fig. 2.8

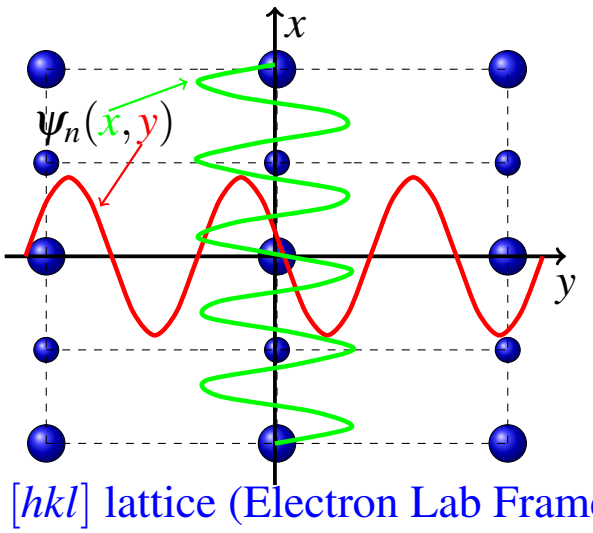

Figure 2.8: The beam electron's state functions $\Phi_n(x,y)$ operating within the Lorentz Contracted Crystal to approximately a transverse plane, (hkl) which is perpendicular to the beam's direction [hkl]. The blue balls are the ions or contracted ion locations along the transverse plane. In this construct, each ion is a point charge. The wave which interacts with these ion point charge lattice operates transversely to the beam's direction [hkl].

In this general review on two different outlooks about the physics of channeling radiation, there are some clear similarities between these approaches. The electron beam's transverse motion to $[hkl]$ relates to the interaction with the transverse potential of the lattice $[hkl]$ orientation. In the 2-D Axial model method, it views that the electron is actually interacting with an axis of ions that approximate a continuum line charge in the direction $[hkl]$. This requires one to construct a lattice of Axial single-string of Ions to represent a lattice of line charges which generates a two-Dimensional potential. Or, for a one-dimensional approximation of the potential, the convention is to construct a lattice of planes with a continuum charge approximation in lieu of the ions located within these planes. If the electron's transverse momentum is small enough, the transverse potential will bound the electron at specific energy states. But, as we shall see, this construction of either the 2-D Axial or planar lattice to generate a transverse potential is not trivial.

In this study, as in the work of Lindhard, orientation matters. Like the 2-D Axial model approach, the orientation of the lattice relative to $[hkl]$ is critical in generating transverse potentials that are large enough to effectively interact with the electron to create bound states. But, instead of constructing a new coordinate system for the lattice for each $[hkl]$ defined, this approach uses the

well defined original coordinates of the lattice to calculate how each ion contributes to the lattice's overall three-dimensional potential. The contributions of each ion's potential to the overall potential are exact. Therefore, determining the lattice potential is relatively simple within its original coordinates. We then just rotate the coordinates to align the new coordinates with the lattice orientation of interest. Rotating the coordinates effectively aligns the beam direction with the lattice orientation of interest. Consequently, the transverse potential relative to this orientation generates the channeling radiation specific to this lattice orientation and beam energy. This method in generating the transverse potential is simple, direct and almost trivial when compared to the conventional practices.

Although not specifically discussed in this chapter, this study's approach readily identifies the correct primitive cells to ensure that the Schrödinger equation is constructed properly with the Bloch waves based on the potential's fundamental periodicity. Our study does not use critical angle θ_c directly as a parameter. Instead, it uses the beam's emittance and twist parameters as the natural approach towards determining the probability that an electron within the beam is in a bound transverse state or not. Consequently, based on the emittance structure rather than the critical angle, this approach can use the parameters of the beam which are well known and familiar to determine whether channeling conditions are met and predict specific channeling energy emission lines and intensities.

Chapter 3

Potential

To study the channeling radiation spectrum theoretically and computationally, the first task is to construct a lattice potential on the two-dimensional beam transverse plane that is parallel to a crystal plane (hkl) for an ultra-relativistic beam channeling along [hkl] crystal direction. Note that this lattice potential is the result of a Lorentz contraction of the original three-dimensional crystal lattice in the beam rest frame, where the crystal travels with near the speed of light along $[hk\bar{l}]$ direction and the three-dimensional crystal lattice is pancaked into a two-dimensional lattice on the (hkl) crystal plane. An accurate lattice potential is crucial in the calculation of energy eigenstates of beam electrons in a crystal for the radiation spectrum. With a given model for the interaction between a beam electron and individual ion in a crystal, such as the Born approximation for scattering with Doyle-Turner fitting parameters, the question is what is the best approach, in terms of accuracy, mathematical simplicity, and generally applicable to any crystal structure and channeling orientation, for the construction of this lattice potential on the two-dimensional plane. In this chapter, we will introduce a new and (we believe) the best approach for this lattice potential calculation.

In previous studies of channeling radiation, the lattice potential is traditionally calculated using an axial channeling model [1, 2, 9, 14] in which each string of crystal ions that is along the beam channeling direction has to be identified and the lattice potential is calculated through a summation

over the strings of the ions. In this direct calculation of the lattice potential, the identification of all the strings of the ions and the geometric relationships among the strings is cumbersome and in some cases very difficult due to a complicated geometric relationship among lattice ions along the channeling direction and, moreover, the calculation developed for a specific channeling direction of a certain crystal can hardly be applied to other cases because the strings of the ions are very different with different crystal structure and different channeling direction. Therefore, only limited cases of the channeling along certain crystal direction have been studied so far using the axial channeling model without substantial approximations. In our approach, a lattice potential of the original three-dimensional crystal is first calculated from the individual electron-ion interaction potential in the original unit-cell coordinate of the crystal by taking the advantage of the native periodicity of the crystal lattice. This potential for the three-dimensional lattice in the unit-cell coordinate is then transferred into a beam coordinate that is aligned with the beam longitudinal and transverse directions using a series of rotational coordinate transformations. Lastly, the Lorentz contraction of the lattice can be easily accomplished mathematically by averaging the three-dimensional lattice potential in the beam coordinate along the beam longitudinal direction. In this approach, the calculation of the lattice potential is mathematically clean, systematic, and can be easily applied to any crystal and any channeling direction. In summary, with both our method and the previous axial channeling model, the lattice potential in the beam transverse plane is calculated in a Fourier expansion of

$$V(x,y) = \sum_{k_1=-\infty}^{\infty} \sum_{k_2=-\infty}^{\infty} v_{k_1 k_2} \, e^{i2\pi\left(k_1 x/a_x + k_2 y/a_y\right)} \tag{3.1}$$

where a_x and a_y are the lattice constants of the primitive unit cell of the two-dimensional lattice on the transverse plane and (x,y) are the coordinate based on the unit cell. With a given model for the electron-ion interaction, in our approach the expansion coefficients $v_{k_1 k_2}$ are calculated systematically and exactly without any approximation, while in the axial channeling model $v_{k_1 k_2}$ are calculated approximately and the approximation depends on the crystal structure and the channeling orientation. Moreover, in our approach the calculation is generic to any crystal structure and channeling orientation while in axial model the calculation and approximation have to be specifi-

cally tailored for a specific crystal structure and channeling orientation. Our approach is therefore much more accurate, flexible, and less complex in constructing the lattice potential on the beam transverse plane as compared with the previous methods.

3.1 Formulation of the Lattice Potential in the Transverse Plane of a Ultra-Relativistic Beam Channeling Through a Crystal

3.1.1 Interaction Between an Electron Passing by and an Ion inside a Crystal

When an electron passes by an ion in a crystal, the electron is scattered by the ion due to the interaction between the electron and ion. With the Born approximation, the scattering amplitude can be written as [18]

$$f_{el}(\vec{Q}) = -\frac{m_e}{2\pi\hbar^2}\int_{-\infty}^{\infty} V_{atom}(\vec{r})e^{i\vec{Q}\cdot\vec{r}}d\vec{r} \tag{3.2}$$

where m_e is the electron rest mass, $\vec{Q} = \vec{k} - \vec{k}'$ with $\vec{k}$ and $\vec{k}'$ being the incident and scattered wave vectors, respectively, and $V_{atom}(\vec{r})$ is the interaction potential between the electron and ion. Note that f_{el} is proportional to the Fourier transformation of $V_{atom}(\vec{r})$ and Eq. (3.2) provides a means to calculate the electron-ion interaction from experimental measurements of $f_{el}(\vec{Q})$,

$$V_{atom}(\vec{r}) = -\frac{\hbar^2}{(2\pi)^2 m_e}\int_{-\infty}^{\infty} f_{el}(\vec{Q})e^{-i\vec{Q}\cdot\vec{r}}d\vec{Q} \tag{3.3}$$

If the electron is not too close to the core of the ion, the interaction between the electron and ion is approximately spherically symmetric and $f_{el}(\vec{Q})$ depends only on $Q = |\vec{Q}|$. Therefore,

$$V_{atom}(\vec{r}) = -\frac{\hbar^2}{m_e\pi r}\int_{0}^{\infty} f_{el}(Q)\sin(Qr)QdQ \tag{3.4}$$

Table 3.1: Doyle-Turner's fit parameters are α_i and β_i where $i \in \{1,2,3,4\}$ [8] and a is the atom-/ion's Lattice Constant and the ion's one dimensional atomic vibrational is $\langle u \rangle$ [4, 9, 10] .

Ion	α_1 [Å]	α_2 [Å]	α_3 [Å]	α_4 [Å]	a [Å]	$\langle u \rangle$[Å]
C	0.7307	1.1951	0.4563	0.1247	3.57	0.042
Si	2.1293	2.5333	0.8349	0.3216	5.4307	0.075
Ge	2.4467	2.7015	1.6157	0.6009	5.658	0.085
	β_1 [Å^2]	β_2 [Å^2]	β_3 [Å^2]	β_4 [Å^2]		
C	36.9951	11.2966	2.8139	0.3456		
Si	57.7748	16.4756	2.8796	0.3860		
Ge	55.8930	14.3930	2.4461	0.3415		

In the case of carbon, silicon, or germanium, which are the crystals usually used for the electron channeling, the experimental data fitting of $f_{el}(Q)$ can be calculated with a Gaussian function as

$$f_{el}(Q) = \sum_{i=1}^{4} \alpha_i e^{-\beta_i Q^2/(4\pi)^2} \tag{3.5}$$

where α_i and β_i are the Doyle-Turner fitting parameters [8], (see Table 3.1). The electron-ion interaction potential can then be calculated by substituting Eq. (3.5) into Eq. (3.4) as

$$V_{atom}(\vec{r}) = -\frac{16\pi\hbar^2}{m_e} \sum_{i=1}^{4} \frac{\alpha_i}{(\beta_i/\pi)^{3/2}} e^{-4\pi^2 r^2/\beta_i} \tag{3.6}$$

3.1.2 Lattice Potential for an Electron Channeling Through a Crystal

Consider an electron channeling through a crystal with orthorhombic lattice and each unit cell of the lattice containing n ions. Let $\vec{r}_j$ with $j = 1, \cdots, n$ be the local coordinates of the ions in a unit cell, where the origin of the local coordinate is at a corner of a unit cell, and $\vec{r}_m = (m_1 a_1, m_2 a_2, m_3 a_3)$ be the global coordinate of a unit cell, where (a_1, a_2, a_3) are lattice constants of the crystal and (m_1, m_2, m_3) are integers. Table 3.2 lists the values of $\vec{r}_j$ for cubic diamond

lattice. Let $\vec{X} = (X_1, X_2, X_3)$ be a global coordinate, referred as lattice coordinate, with the axes of X_1, X_2, and X_3 aligned with the [100], [010], and [001] crystal direction, respectively. When an electron channels through the crystal, the interaction between the electron and the crystal lattice can be calculated by a superposition of the interactions between the electron and each individual ion as

$$\begin{aligned} V_{3D}(\vec{X}) &= \sum_{\vec{m}=-\infty}^{\infty} \sum_{j=1}^{n} V_{atom}(\vec{X} - \vec{r}_m - \vec{r}_j) \\ &= -\frac{16\pi\hbar^2}{m_e} \sum_{\vec{m}=-\infty}^{\infty} \sum_{j=1}^{n} \sum_{i=1}^{4} \frac{\alpha_i}{(\beta_i/\pi)^{3/2}} \exp\left(-\frac{4\pi^2}{\beta_i} \left|\vec{X} - \vec{r}_m - \vec{r}_j\right|^2\right) \end{aligned} \tag{3.7}$$

where $\vec{m}$ is the lattice coordinate of a unit cell in the crystal and n is the number of ions in a unit cell. It is obvious from Eq. (3.7) that $V_{3D}(\vec{X})$ is periodic in the crystal, *i.e.* $V_{3D}(\vec{X} + \vec{r}_l) = V_{3D}(\vec{X})$, where $\vec{r}_l = (l_1 a_1, l_2 a_2, l_3 a_3)$ and (l_1, l_2, l_3) is any combination of integers. With the lattice periodicity periodicity, $V_{3D}(\vec{X})$ can be rewritten into a Fourier expansion

$$V_{3D}(\vec{X}) = \sum_{\vec{k}=-\infty}^{\infty} V_{\vec{k}}\, e^{i\vec{G}\cdot\vec{X}} \tag{3.8}$$

where

$$\vec{G} = (G_1, G_2, G_3) = 2\pi\,(k_1/a_1\,, k_2/a_2\,, k_3/a_3) \tag{3.9}$$

is the reciprocal lattice vector of the crystal and

$$\begin{aligned} V_{\vec{k}} &= \frac{1}{a_1 a_2 a_3} \int_0^{a_1}\int_0^{a_2}\int_0^{a_3} V_{3D}(\vec{X})\, e^{-i\vec{G}\cdot\vec{X}}\, d\vec{X} \\ &= -\frac{16\pi\hbar^2}{m_e v_0} \sum_{\vec{m}=-\infty}^{\infty} \sum_{j=1}^{N} \sum_{i=1}^{4} \frac{\alpha_i}{(\beta_i/\pi)^{3/2}} \int_0^{a_1} dX_1 \int_0^{a_2} dX_2 \int_0^{a_3} dX_3 \\ &\qquad \times \exp\left[-\frac{4\pi^2}{\beta_i}\left|\vec{X} - \vec{r}_m - \vec{r}_j\right|^2 - i\vec{G}\cdot\vec{X}\right] \\ &= -\frac{16\pi\hbar^2}{m_e v_0} \sum_{\vec{m}=-\infty}^{\infty} \sum_{j=1}^{N} \sum_{i=1}^{4} \frac{\alpha_i}{(\beta_i/\pi)^{3/2}} I(G_1, \beta_i, x_j) I(G_2, \beta_i, y_j) I(G_3, \beta_i, z_j) \end{aligned} \tag{3.10}$$

with $v_0 = a_1 a_2 a_3$. In Eq. (3.10),

$$I(G_l,\beta_i,x_j) \;=\; \int_0^{a_l} e^{-4\pi^2\left(X-m_l a_l-x_j\right)^2/\beta_i - iG_l X}\,dX \;\overset{X=a_l\xi}{=}\; a_l \int_0^{1} e^{-(\xi-m_l-x_j/a_l)^2/2\sigma_l^2} e^{-i2\pi k_l \xi}\,d\xi$$

$$\overset{x=\xi-m_l-x_j/a_l}{=}\; a_l e^{-i2\pi k_l (x_j/a_l)} \int_{-(m_l+x_j/a_l)}^{1-(m_l+x_j/a_l)} e^{-x^2/2\sigma_l^2} e^{-i2\pi k_l x}\,dx$$

where $\sigma_l^2 = \beta_i/(8\pi^2 a_l^2)$, and

$$\begin{aligned}
&\sum_{\vec{m}=-\infty}^{\infty} I(G_1,\beta_i,x_j) I(G_2,\beta_i,y_j) I(G_3,\beta_i,z_j) \\
&= v_0 \sum_{\vec{m}=-\infty}^{\infty} \exp\left[-i2\pi\left(\frac{k_1 x_j}{a_1}+\frac{k_2 y_j}{a_2}+\frac{k_3 z_j}{a_3}\right)\right] \\
&\quad \times \int_{-(m_1+x_j/a_1)}^{1-(m_1+x_j/a_1)} dx \int_{-(m_2+y_j/a_2)}^{1-(m_2+y_j/a_2)} dy \int_{-(m_3+z_j/a_3)}^{1-(m_3+z_j/a_3)} dz \exp\left(-\frac{x^2}{2\sigma_1^2}-\frac{y^2}{2\sigma_2^2}-\frac{z^2}{2\sigma_3^2}-i2\pi\vec{k}\cdot\vec{r}\right) \\
&= v_0 \exp\left[-i2\pi\left(\frac{k_1 x_j}{a_1}+\frac{k_2 y_j}{a_2}+\frac{k_3 z_j}{a_3}\right)\right] \left(\sum_{m_1=-\infty}^{\infty} \int_{-(m_1+x_j/a_1)}^{1-(m_1+x_j/a_1)} e^{-x^2/2\sigma_1^2 - i2\pi k_1 x}\,dx\right) \\
&\quad \times \left(\sum_{m_2=-\infty}^{\infty} \int_{-(m_2+y_j/a_2)}^{1-(m_2+y_j/a_2)} e^{-y^2/2\sigma_2^2 - i2\pi k_2 y}\,dy\right) \left(\sum_{m_3=-\infty}^{\infty} \int_{-(m_3+z_j/a_3)}^{1-(m_3+z_j/a_3)} e^{-z^2/2\sigma_3^2 - i2\pi k_3 z}\,dz\right)
\end{aligned}$$

Since

$$\sum_{m=-\infty}^{\infty} \int_{-(m+x_j/a_1)}^{1-(m+x_j/a_1)} \exp\left(-\frac{x^2}{2\sigma_1^2} - i2\pi k_1 x\right) dx = \sum_{m=\infty}^{-\infty} \int_{-m-x_j/a_1}^{1-m-x_j/a_1} \exp\left(-\frac{x^2}{2\sigma_1^2} - i2\pi k_1 x\right) dx$$

$$\stackrel{N\to\infty}{=} \left(\int_{-N-x_j/a_1}^{-N+1-x_j/a_1} + \int_{-N+1-x_j/a_1}^{-N+2-x_j/a_1} + \cdots \int_{-2-x_j/a_1}^{-1-x_j/a_1} + \int_{-1-x_j/a_1}^{-x_j/a_1} + \int_{-x_j/a_1}^{1-x_j/a_1} + \cdots \int_{N-x_j/a_1}^{N+1-x_j/a_1} \right)$$

$$\times \exp\left(-\frac{x^2}{2\sigma_1^2} - i2\pi k_1 x\right) dx$$

$$= \int_{-N-x_j/a_1}^{N+1-x_j/a_1} e^{-x^2/2\sigma_1^2 - i2\pi k_1 x} dx \stackrel{N\to\infty}{=} \int_{-\infty}^{\infty} e^{-x^2/2\sigma_1^2} e^{-i2\pi k_1 x} dx = \sqrt{2\pi}\sigma_1 e^{-(2\pi k_1\sigma_1)^2/2},$$

We have

$$\sum_{\vec{m}=-\infty}^{\infty} I(G_1,\beta_i,x_j) I(G_2,\beta_i,y_j) I(G_3,\beta_i,z_j)$$

$$= (2\pi)^{3/2}\sigma_1\sigma_2\sigma_3 \exp\left\{-i2\pi\left(\frac{k_1x_j}{a_1} + \frac{k_2y_j}{a_2} + \frac{k_3z_j}{a_3}\right) - 2\pi^2\left[(k_1\sigma_1)^2 + (k_2\sigma_2)^2 + (k_3\sigma_3)^2\right]\right\}$$

$$= \left(\frac{\beta_i}{4\pi}\right)^{3/2} \exp\left\{-i2\pi\left(\frac{k_1x_j}{a_1} + \frac{k_2y_j}{a_2} + \frac{k_3z_j}{a_3}\right) - \beta_i\left[\left(\frac{k_1}{2a_1}\right)^2 + \left(\frac{k_2}{2a_2}\right)^2 + \left(\frac{k_3}{2a_3}\right)^2\right]\right\}$$

and

$$V_{\vec{k}} = -\frac{2\pi\hbar^2}{m_e v_0} \sum_{i=1}^{4} \alpha_i \exp\left\{-\beta_i\left[\left(\frac{k_1}{2a_1}\right)^2 + \left(\frac{k_2}{2a_2}\right)^2 + \left(\frac{k_3}{2a_3}\right)^2\right]\right\}$$

$$\times \sum_{j=1}^{N} \exp\left\{-i2\pi\left(\frac{k_1x_j}{a_1} + \frac{k_2y_j}{a_2} + \frac{k_3z_j}{a_3}\right)\right\} \tag{3.11}$$

For crystals with a cubic lattice such as silicon, germanium and diamond, $a_1 = a_2 = a_3 = a$ and

$$V_{\vec{k}} = -\frac{2\pi\hbar^2}{m_e v_0} \sum_{i=1}^{4} \alpha_i e^{-k^2\beta_i/(4a^2)} \sum_{j=1}^{N} e^{-i2\pi\vec{k}\cdot(\vec{r}_j/a)} \tag{3.12}$$

where $k^2 = k_1^2 + k_2^2 + k_3^2$. Including the Debye-Waller factor effects of lattice vibrations $\exp\left(-2\pi^2 k^2 \left\langle \mu^2 \right\rangle / a^2\right)$ where $\langle \mu \rangle$ is the average one dimensional ion vibration for diamond, silicon, and germanium listed in Table 3.1. The Fourier transformation of the electron-lattice interaction potential can be calculated as

$$V_{\vec{k}} = -\frac{2\pi\hbar^2}{m_e v_0} \sum_{i=1}^{4} \alpha_i e^{-k^2\lambda_i^2} \sum_{j=1}^{N} \exp\left[-i\frac{2\pi}{a}\left(k_1 x_j + k_2 y_j + k_3 z_j\right)\right] \tag{3.13}$$

where $\lambda_i^2 = \left(\beta_i + 8\pi^2 \left\langle \mu^2 \right\rangle\right)/(2a)^2$, and α_i and β_i are the Doyle-Turner fitting parameters for electron scattering amplitude from a single ion[8] (see Table 3.1). Note that the lattice potential calculated from Eqs. (3.8) and (3.13) includes exactly the contributions of all the ions in a crystal and only approximation involved is the calculation of the interaction between an electron and a single ion using the Born approximation with the Doyle-Turner fitting parameters in Eq. (3.6). To calculate the lattice potential $V_{3D}(\vec{X})$ numerically, the summations over $\vec{k}$ have to be truncated. Note that $V_{\vec{k}}$ decays exponentially with k^2. For cubic diamond lattice, however, $\beta_i/4a^2 = 0.726$, 0.222, 0.055, and 0.00068 and the truncation has to be done at sufficiently larger k^2 to ensure the convergence.

Table 3.2: Ion position $\vec{r}_j$ in a unit cell of diamond where the origin of the coordinate is at a corner of the unit cell and a is the lattice constant of diamond [4].

j	1	2	3	4	5	6	7	8
x_j/a	0	1/4	0	1/4	1/2	3/4	1/2	3/4
y_j/a	0	1/4	1/2	3/4	0	1/4	1/2	3/4
z_j/a	0	1/4	1/2	3/4	1/2	3/4	0	1/4

3.1.3 Lattice Potential in the Beam Transverse Plane

Consider an electron beam channeling through a crystal as the beam travels near the speed of light along the beam longitudinal direction while the beam electrons oscillate non-relativistically in the beam transverse plane. The lattice potential $V_{3D}(\vec{X})$ in Eqs. (3.8) and (3.13) is expressed in the lattice coordinate $\vec{X}$ that is aligned with the primary crystal axes but not in the direction of the beam.

In order to study the transverse motion of the beam electrons under the influence of the lattice potential, however, the lattice potential in the beam transverse plane is needed. As the beam is ultra-relativistic, moreover, the interaction between a beam electron channeling through the crystal and the ions in the crystal is too weak to have a significant effect on the longitudinal motion of the electron and the dependence of the lattice potential on the longitudinal coordinate of the electron can be neglected by averaging the potential over the longitudinal direction. It is therefore necessary to have the lattice potential expressed in the beam coordinate that is aligned with the motion of the beam. Let $\vec{r} = (x, y, z)$ be the beam coordinate where z is along the longitudinal direction of the beam and (x, y) are two orthogonal coordinates in the beam transverse plane. In order to solve the Bloch eigenfunctions and eigenenergies for the transverse motion of beam electrons in the crystal, x and y should be along the axes of a two-dimensional primitive unit cell in the transverse plane which has to be determined based on the periodicity of the lattice potential in the transverse plane and may not be the same as the periodicity of the original three-dimensional lattice in that plane. The transformation from the lattice coordinate $\vec{X}$ to the beam coordinate $\vec{r}$ can be accomplished by a 3×3 rotational matrix $\mathbf{R}$,

$$\vec{r} = \mathbf{R}\vec{X} \tag{3.14}$$

and lattice potential $V_{3D}(\vec{X})$ in Eq. (3.8) can be rewritten in the beam coordinate as

$$V_{3D}(\vec{r}) = \sum_{\vec{k}=-\infty}^{\infty} V_{\vec{k}} \exp\left[i\vec{G}^T \left(\mathbf{R}^{-1}\mathbf{R}\right)\vec{X}\right] = \sum_{\vec{k}=-\infty}^{\infty} V_{\vec{k}} \exp\left[i(\vec{G}^T\mathbf{R}^{-1})\cdot\vec{r}\right] \tag{3.15}$$

Note that $V_{3D}(\vec{r})$ is a different function from $V_{3D}(\vec{X})$ in general. We re-used V_{3D} for the potential expressed in $\vec{r}$ to simplify the notation. Since the crystal has also a periodic structure along the orientations of the beam coordinate, $V_{3D}(\vec{r})$ is periodic,

$$V_{3D}(x + n_1 b_1\,,\, y + n_2 b_2\,,\, z + n_3 b_3) = V_{3D}(x, y, z)$$

where (b_1, b_2, b_3) is the periodicities of the crystal lattice along the (x, y, z) direction, respectively, and (n_1, n_2, n_3) is any combination of integers. The periodicity of $V_{3D}(\vec{r})$ requires

$$e^{ib_1(\vec{G}^T\mathbf{R}^{-1})_1} = e^{ib_2(\vec{G}^T\mathbf{R}^{-1})_2} = e^{ib_3(\vec{G}^T\mathbf{R}^{-1})_3} = 1$$

or

$$\vec{G}^T\mathbf{R}^{-1} = 2\pi\,(\,n_1/b_1\,,\,n_2/b_2\,,\,n_3/b_3\,) \tag{3.16}$$

The transformation of the reciprocal lattice vector can thus be written as

$$(\,k_1/a_1\,,\,k_2/a_2\,,\,k_3/a_3\,)\,\mathbf{R}^{-1} = (\,n_1/b_1\,,\,n_2/b_2\,,\,n_3/b_3\,) \tag{3.17}$$

The relationships between (b_1, b_2, b_3) and (a_1, a_2, a_3) and between (n_1, n_2, n_3) and (k_1, k_2, k_3) can be solved from Eq. (3.17) with the fact that (n_1, n_2, n_3) and (k_1, k_2, k_3) are integers. With the coordinate correctly aligned with the beam directions, the average of the lattice potential along the beam longitudinal (z) direction can be calculated as

$$\begin{aligned} V(x,y) &= \frac{1}{b_3}\int_0^{b_3} V_{3D}(\vec{r})\,dz \\ &= \sum_{\vec{k}=-\infty}^{\infty} V_{\vec{k}}\exp\left[i2\pi\left(\frac{n_1 x}{b_1}+\frac{n_2 y}{b_2}\right)\right]\left[\frac{1}{b_3}\int_0^{b_3}\exp\left(i\frac{2\pi n_3 z}{b_3}\right)dz\right] \\ &= \sum_{\vec{k}=-\infty}^{\infty} V_{\vec{k}}\exp\left\{i2\pi\left[\frac{x}{b_1}n_1(\vec{k})+\frac{y}{b_2}n_2(\vec{k})\right]\right\}\delta_{n_3(\vec{k})0} \end{aligned} \tag{3.18}$$

where n_1, n_2, and n_3 are functions of $\vec{k}$ given in Eq. (3.17) and

$$\frac{1}{b_3}\int_0^{b_3}\exp\left(i\frac{2\pi n_3 z}{b_3}\right)dz = \delta_{n_3 0} \tag{3.19}$$

is the Kronecker delta for $n_3(\vec{k}) = 0$. It should be noted that the periodicity of the projected lattice potential $V(x,y)$ on the transverse plane could be smaller than b_1 and b_2 of the original three-dimensional lattice due to the averaging of $V_{3D}(\vec{r})$ along the longitudinal direction of the

beam. The change of the periodicity occurs when the summation over the ions in a unit cell in Eq. (3.13) zeros $V_{\vec{k}}\big|_{n_3(\vec{k})=0}$ periodically for a certain combinations of (k_1,k_2,k_3) with $n_3(\vec{k})=0$. As the periodicity of $V(x,y)$ is important to the calculation of the energy states of the Bloch waves for the beam electrons, the existence of the periodic zero points of

$$S_{ions}(n_1(\vec{k}),n_2(\vec{k}))=\sum_{j=1}^{N}\exp\left[-i\frac{2\pi}{a}\left(k_1x_j+k_2y_j+k_3z_j\right)\right]\Bigg|_{n_3(\vec{k})=0} \tag{3.20}$$

needs to be examined for each case.

3.2 Beam Channeling Along [001] Crystal Direction

3.2.1 Beam horizontal (x) axis is aligned with [100] crystal direction

Consider an electron beam channeling through a crystal with cubic diamond lattice along the [001] crystal direction. The horizontal (x) and vertical (y) beam axes are aligned with the [100] and [010] crystal direction, respectively. In this case, the beam coordinate (x,y,z) is aligned with the lattice coordinate (X_1,X_2,X_3) and no coordinate transformation is needed. After averaging over the beam longitude direction, the lattice potential in the beam transverse plane is

$$V(x,y)=\sum_{k_1=-\infty}^{\infty}\sum_{k_2=-\infty}^{\infty}V_{k_1k_2}\exp\left[i\frac{2\pi}{a}\left(k_1x+k_2y\right)\right] \tag{3.21}$$

where

$$V_{k_1k_2}=V_{\vec{k}}\big|_{k_3=0}=-\frac{2\pi\hbar^2}{mv_0}\sum_{i=1}^{4}\alpha_i e^{-\lambda_i^2(k_1^2+k_2^2)}\sum_{j=1}^{N}\exp\left[-i\frac{2\pi}{a}\left(k_1x_j+k_2y_j\right)\right] \tag{3.22}$$

With x_j and y_j given in Table 3.2, it can easily be checked that the summation over j in Eq. (3.22) is nonzero only when both k_1 and k_2 are even. Let $k_1=2n_1$ and $k_2=2n_2$. Then

$$V(x,y)=\sum_{n_1=-\infty}^{\infty}\sum_{n_2=-\infty}^{\infty}v_{n_1n_2}\exp\left[i\frac{2\pi}{a/2}\left(n_1x+n_2y\right)\right] \tag{3.23}$$

where

$$v_{n_1 n_2} = V_{(2n_1)(2n_2)} = -\frac{2\pi\hbar^2}{m v_0} \sum_{i=1}^{4} \alpha_i e^{-4(n_1^2+n_2^2)\lambda_i^2} \sum_{j=1}^{N} \exp\left[-i\frac{2\pi}{a/2}\left(n_1 x_j + n_2 y_j\right)\right] \tag{3.24}$$

The periodicity of $V(x,y)$ is therefore $a/2$ in both x and y direction when x and y are along the [100] and [010] crystal direction. The contour plot of $V(x,y)$ potential is given in Fig. 3.1.

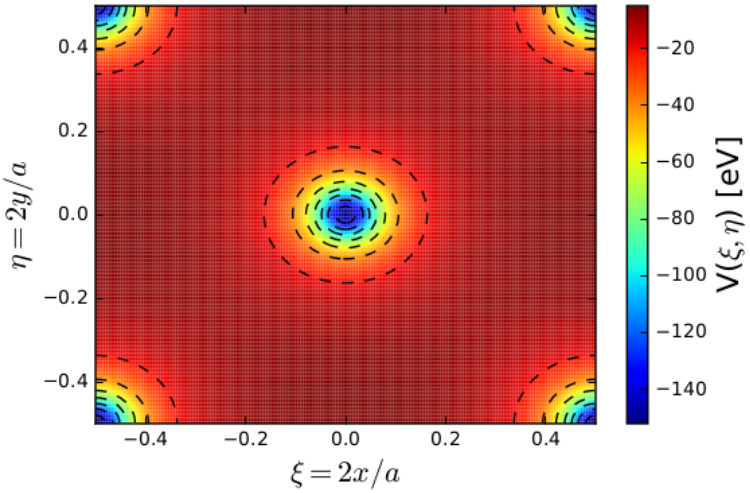

Figure 3.1: Contour plot of lattice potential $V(\xi,\eta)$ on beam transverse plane for channeling of germanium with 9 MeV electron beam along [001] crystal direction, where ξ and η are aligned with [100] and [010] crystal direction, respectively.

3.2.2 Beam horizontal (x) axis is aligned with [110] crystal direction

The coordinate in the transverse plane used for $V(x,y)$ in Eq. (3.23) is aligned with [100] and [010] crystal axes but not along the primitive unit cell of the two-dimensional lattice based on the periodicity of the lattice potential in the beam transverse plane as shown in the contour plot of $V(x,y)$ in Fig. 3.1, where the periodicity of $V(x,y)$ is $a/2$ in both [100] and [010] direction, while the smallest periodicity of $V(x,y)$ is $a/(2\sqrt{2})$ along [110] or $[\bar{1}10]$ direction (see Fig. 3.2). Note that on the original (001) crystal plane of three-dimensional diamond lattice, the ions are in body centered cubic structure with two unit-cell axes along [100] and [010] direction and, within every four planes as a group, the (001) planes rotate 45° and shift by $a/4$ along both [100] and [010] crystal direction with respect to each other. Due to the Lorentz contraction of the three-dimensional

lattice along the [001] direction, all the ions in the three-dimensional lattice are projected onto a two-dimensional plane parallel to the (001) plane and, consequently, extra ions appear on the (001) plane and results in a reduction of the period as shown in Fig. 3.2. A coordinate transformation is therefore needed to rotate x and y axes in Eq. (3.23) to align with [110] and $[\bar{1}10]$ crystal axes, *i.e.*

$$\begin{pmatrix} x_{[100]} \\ y_{[010]} \end{pmatrix} = \begin{pmatrix} \cos(\pi/4) & -\sin(\pi/4) \\ \sin(\pi/4) & \cos(\pi/4) \end{pmatrix} \begin{pmatrix} x_{[110]} \\ y_{[\bar{1}10]} \end{pmatrix} \tag{3.25}$$

where $\left(x_{[100]}, y_{[010]}\right)$ and $\left(x_{[110]}, y_{[\bar{1}10]}\right)$ are the coordinate aligned with ([100], [010]) and $\left([110], [\bar{1}10]\right)$, respectively. To simplify the notation, we will use (x,y) for the primitive coordinate $\left(x_{[110]}, y_{[\bar{1}10]}\right)$ and $V_{[001]}(x,y)$ for the potential expressed with $(x,y) = \left(x_{[110]}, y_{[\bar{1}10]}\right)$. The lattice potential with x and y coordinate aligned with [110] and $[\bar{1}10]$ crystal axes is then

$$\begin{aligned} V(x,y) &= \sum_{n_1=-\infty}^{\infty} \sum_{n_2=-\infty}^{\infty} v_{n_1 n_2} \exp\left\{ i \frac{2\pi}{(a/2)\sqrt{2}} \left[n_1(x-y) + n_2(x+y) \right] \right\} \\ &= \sum_{k_1=-\infty}^{\infty} \sum_{k_2=-\infty}^{\infty} \tilde{v}_{k_1 k_2} \exp\left[i \frac{2\pi}{a/(2\sqrt{2})} \left(k_1 x + k_2 y \right) \right] \end{aligned} \tag{3.26}$$

where $n_1 = k_1 - k_2$, $n_2 = k_1 + k_2$, and with (x_j, y_j) in a cubic diamond lattice given in Table (3.2)

$$\begin{aligned} \tilde{v}_{k_1 k_2} &= -\frac{2\pi\hbar^2}{m v_0} \sum_{i=1}^{4} \alpha_i e^{-8\lambda_i^2 (k_1^2 + k_2^2)} \sum_{j=1}^{N} \exp\left\{ -i \frac{2\pi}{a/2} \left[k_1 (x_j + y_j) + k_2 (y_j - x_j) \right] \right\} \\ &= -\frac{16\pi\hbar^2}{m v_0} \sum_{i=1}^{4} \alpha_i e^{-8\lambda_i^2 (k_1^2 + k_2^2)} \end{aligned} \tag{3.27}$$

The periodicity of $V(x,y)$ in Eq. (3.26) is therefore $a_x = a_y = a/(2\sqrt{2})$ in both x and y direction which are along the [110] and $[\bar{1}10]$ crystal axes, respectively. Figure 3.2 plots $V(x,y)$ in the correct primitive cell and the relationship between primitive and non-primitive cell on the beam transverse plane is sketched in Fig. 3.2.

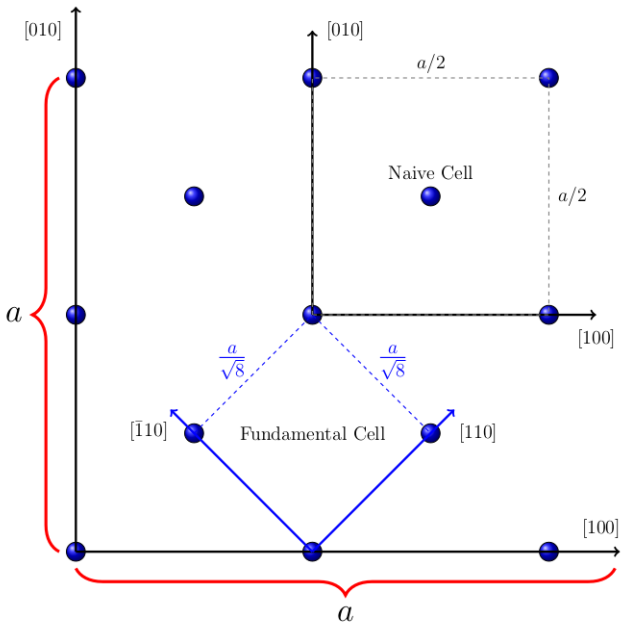

Figure 3.2: Projection of all the ions in a unit cell of diamond onto (001) plane that is the beam transverse plane for channeling along [001] crystal direction. Two axes of the primitive cell are along [110] abd [$\bar{1}$10] direction with the lattice constant $a_x = a_y = a/\sqrt{8}$.

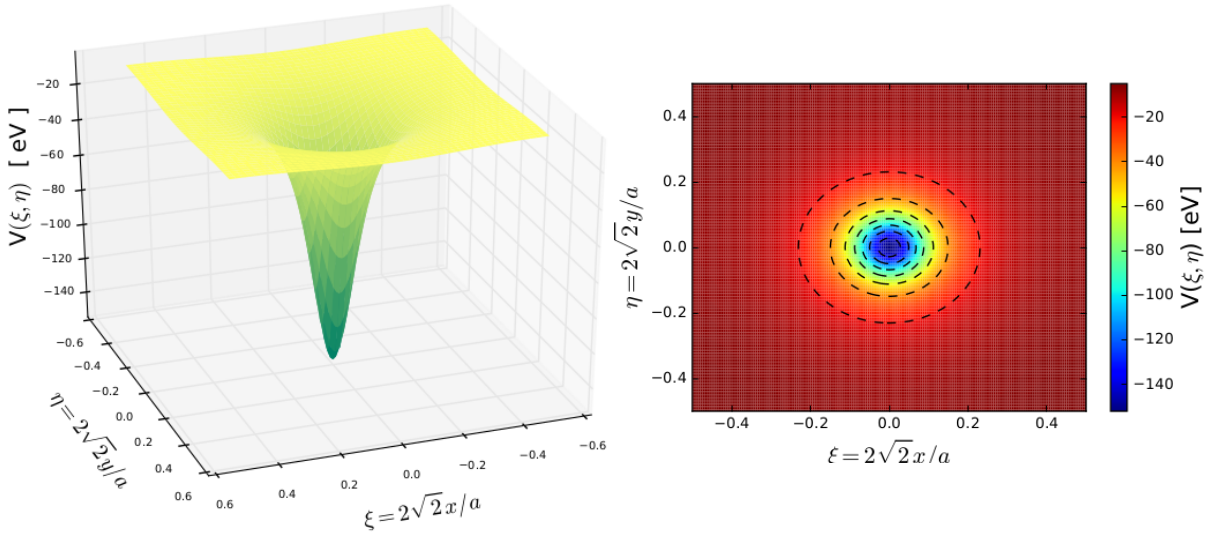

Figure 3.3: Same as Fig. 3.1 but $\xi$and η are aligned with [110] and [$\bar{1}$10] crystal direction, respectively.

3.3 Beam Channeling Along [110] Crystal Direction

Consider that a beam is channeling along the [110] crystal axis and the beam transverse plane is parallel to the (110) crystal plane. The transformation $\mathbf{R}$ from the lattice coordinate (X_1, X_2, X_3) to the beam coordinate (x, y, z) can be constructed with two coordinate transformations. The first is to rotate the (X_1, X_2, X_3)-coordinate in the $X_1 - X_2$ plane by an angle of $\pi/4$ and the resulting coordinate is labeled as (X_1', X_2', X_3). The second transformation is to switch coordinate axes such that $x = X_2'$, $y = X_3$, and $z = X_1'$. In the final coordinate (x, y, z), x and y are along the $[\bar{1}10]$ and $[001]$ crystal axes, respectively, and z is the beam longitudinal direction and along the $[\bar{1}10]$ crystal axis. The combined coordinate transformation can be obtained as

$$\begin{aligned}
\begin{pmatrix} X_1 \\ X_2 \\ X_3 \end{pmatrix} &= \frac{1}{\sqrt{2}} \begin{pmatrix} 1 & -1 & 0 \\ 1 & 1 & 0 \\ 0 & 0 & \sqrt{2} \end{pmatrix} \begin{pmatrix} 0 & 0 & 1 \\ 1 & 0 & 0 \\ 0 & 1 & 0 \end{pmatrix} \begin{pmatrix} x \\ y \\ z \end{pmatrix} \\
&= \frac{1}{\sqrt{2}} \begin{pmatrix} -1 & 0 & 1 \\ 1 & 0 & 1 \\ 0 & \sqrt{2} & 0 \end{pmatrix} \begin{pmatrix} x \\ y \\ z \end{pmatrix} = \mathbf{R}^{-1} \begin{pmatrix} x \\ y \\ z \end{pmatrix}
\end{aligned} \tag{3.28}$$

The reciprocal lattice vector $\vec{G} = (2\pi/a)(k_1, k_2, k_3)$ is transformed, from Eq. (3.17), as

$$\left(\frac{n_1}{b_1}, \frac{n_2}{b_2}, \frac{n_3}{b_3} \right) = \left(\frac{k_1}{a}, \frac{k_2}{a}, \frac{k_3}{a} \right) \cdot \mathbf{R}^{-1} = \left(\frac{k_2 - k_1}{\sqrt{2}a}, \frac{k_3}{a}, \frac{k_1 + k_2}{\sqrt{2}a} \right) \tag{3.29}$$

Since (k_1, k_2, k_3) and (n_1, n_2, n_3) are integers, the minimal periodicity of $V(x, y, z)$ is

$$(b_1, b_2, b_3) = \left(\sqrt{2}a, a, \sqrt{2}a \right) \tag{3.30}$$

and

$$(n_1, n_2, n_3) = (k_2 - k_1, k_3, k_1 + k_2) \tag{3.31}$$

The average of $V(x,y,z)$ over z in Eq. (3.18) leads to $n_3 = k_1 + k_2 = 0$ and, therefore,

$$n_1 = 2k_2\,, \qquad n_2 = k_3 \qquad \text{with} \qquad k_1 = -k_2$$

The lattice potential on the beam transverse plane calculated from Eqs. (3.13) and (3.18) is then

$$V(x,y) = \sum_{k_2=-\infty}^{\infty} \sum_{k_3=-\infty}^{\infty} V_{k_2k_3} \exp\left[i2\pi\left(2k_2\frac{x}{b_1} + k_3\frac{y}{b_2}\right)\right] \tag{3.32}$$

where

$$V_{k_2k_3} = V_{\vec{k}}\big|_{k_1=-k_2} = -\frac{2\pi\hbar^2}{mv_0}\sum_{i=1}^{4}\alpha_i e^{-\lambda_i^2\left(2k_2^2+k_3^2\right)}\sum_{j=1}^{N} e^{-i2\pi[k_2(y_j-x_j)+k_3z_j]/a} \tag{3.33}$$

Relabeling the summation indices in Eq. (3.32) as $n_1 = k_2$ and $n_2 = k_3$, the lattice potential on the (110) crystal plane with x and y aligned with the $[\bar{1}10]$ and $[001]$ crystal axes can be written as

$$V(x,y) = \sum_{n_1=-\infty}^{\infty} \sum_{n_2=-\infty}^{\infty} v_{n_1n_2} \exp\left[i2\pi\left(\frac{n_1x}{a/\sqrt{2}} + \frac{n_2y}{a}\right)\right] \tag{3.34}$$

where

$$v_{n_1n_2} = -\frac{2\pi\hbar^2}{mv_0}\sum_{i=1}^{4}\alpha_i\, e^{-\lambda_i^2\left(2n_1^2+n_2^2\right)}\sum_{j=1}^{N} e^{-i2\pi[n_1(y_j-x_j)+n_2z_j]/a} \tag{3.35}$$

Since there is no additional periodic zero points in $S_{ions}(n_1,n_2)$, the period of $V(x,y)$ are

$$(a_x, a_y) = (a/\sqrt{2}\,, a)$$

for the x and y direction, respectively. As shown in Fig. 3.4, a_x and a_y are the smallest periods of $V(x,y)$ along two orthogonal directions in the transverse plane and, therefore, the $[\bar{1}10]$ and $[001]$ crystal axes are the axes of the primitive unit cell of the two-dimensional direct lattice in the transverse plane when the beam is channeling along the $[110]$ direction.

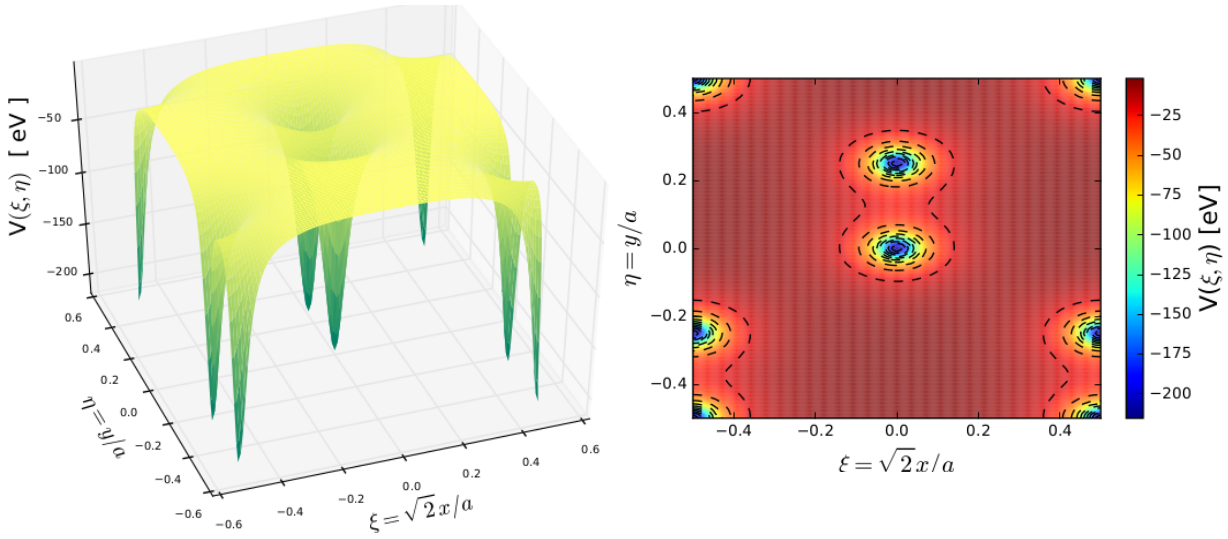

Figure 3.4: Lattice potential $V(x,y)$ on beam transverse plane for channeling of germanium with 9 MeV electron beam along [110] crystal direction.

3.4 Beam Channeling Along [111] Crystal Direction

Consider that the beam is channeling along the [111] crystal direction and the beam transverse plane is parallel to the (111) crystal plane. The transformation matrix $\mathbf{R}$ in Eq. (3.14) can be constructed with three consecutive transformations. The first transformation rotates the lattice coordinate (X_1, X_2, X_3) in the $X_1 - X_2$ plane by an angle of $\theta_1 = \pi/4$ and the transformed coordinate is labeled as (X_1', X_2', X_3). The axes of X_1' and X_2' are aligned with the $[110]$ and $[\bar{1}10]$ crystal direction, respectively. The second transformation is rotating (X_1', X_2', X_3) in the $X_1' - X_3$ plane by an angle of $\theta_2 = \arctan(1/\sqrt{2})$ and the transformed coordinate is labeled as (X_1'', X_2', X_3'). The axes of X_1'', X_2', and X_3' are aligned with $[111]$,$[\bar{1}10]$, and $[\bar{1}\bar{1}2]$ direction, respectively. The third transformation is to switch the coordinate axes such that $x = X_2'$, $y = X_3'$, and $z = X_1''$, where z is the beam longitudinal coordinate and (x,y) are two orthogonal coordinates in the beam transverse

plane. These three coordinate transformations can be expressed as

$$\begin{pmatrix} X_1 \\ X_2 \\ X_3 \end{pmatrix} = \begin{pmatrix} \cos\theta_1 & -\sin\theta_1 & 0 \\ \sin\theta_1 & \cos\theta_1 & 0 \\ 0 & 0 & 1 \end{pmatrix} \begin{pmatrix} \cos\theta_2 & 0 & -\sin\theta_2 \\ 0 & 1 & 0 \\ \sin\theta_2 & 0 & \cos\theta_2 \end{pmatrix} \begin{pmatrix} 0 & 0 & 1 \\ 1 & 0 & 0 \\ 0 & 1 & 0 \end{pmatrix} \begin{pmatrix} x \\ y \\ z \end{pmatrix}$$
$$= \frac{1}{\sqrt{6}} \begin{pmatrix} -\sqrt{3} & -1 & \sqrt{2} \\ \sqrt{3} & -1 & \sqrt{2} \\ 0 & 2 & \sqrt{2} \end{pmatrix} \begin{pmatrix} x \\ y \\ z \end{pmatrix} = R^{-1} \begin{pmatrix} x \\ y \\ z \end{pmatrix} \tag{3.36}$$

where $\sin\theta_2 = 1/\sqrt{3}$ and $\cos\theta_2 = \sqrt{2/3}$. The reciprocal lattice vector $\vec{G} = (2\pi/a)(k_1, k_2, k_3)$ is transformed in accordance to Eq.(3.17) as

$$\begin{aligned} \left(\frac{n_1}{b_1}, \frac{n_2}{b_2}, \frac{n_3}{b_3}\right) &= \left(\frac{k_1}{a}, \frac{k_2}{a}, \frac{k_3}{a}\right) \cdot \mathbf{R}^{-1} \\ &= \left(\frac{k_2 - k_1}{\sqrt{2}a}, \frac{2k_3 - k_1 - k_2}{\sqrt{6}a}, \frac{k_1 + k_2 + k_3}{\sqrt{3}a}\right) \end{aligned} \tag{3.37}$$

Since (k_1, k_2, k_3) and (n_1, n_2, n_3) are integers, the minimal periodicity of $V(x,y,z)$ is

$$(b_1\,, b_2\,, b_3) = \left(\sqrt{2}a\,, \sqrt{6}a\,, \sqrt{3}a\right) \tag{3.38}$$

and

$$(n_1\,, n_2\,, n_3) = (\,k_2 - k_1\,, 2k_3 - k_1 - k_2\,, k_1 + k_2 + k_3\,) \tag{3.39}$$

The average of $V(x,y,z)$ over z in Eq. (3.18) leads to $n_3 = k_1 + k_2 + k_3 = 0$ and, therefore,

$$n_1 = 2k_2 + k_3 \qquad \text{and} \qquad n_2 = 3k_3 \qquad \text{with} \qquad k_1 = -(k_2 + k_3)$$

The lattice potential on the beam transverse plane calculated from Eq. (3.18) is then

$$V(x,y) = \sum_{n_1=-\infty}^{\infty} \sum_{n_2=-\infty}^{\infty} v_{n_1 n_2} \exp\left[i2\pi\left(\frac{n_1 x}{b_1} + \frac{n_2 y}{b_2}\right)\right] \tag{3.40}$$

where $v_{n_1 n_2}$ is obtained from Eq. (3.13) as

$$\begin{aligned} v_{n_1 n_2} &= \sum_{\vec{k}} V_{\vec{k}}\, \delta_{-(k_2+k_3),k_1}\, \delta_{(2k_2+k_3),n_1}\, \delta_{3k_3,n_2} \\ &= -\frac{2\pi\hbar^2}{m v_0} \sum_{k_1} \sum_{k_2} \delta_{(2k_2+k_3),n_1}\, \delta_{3k_3,n_2} \\ &\qquad \times \sum_{i=1}^{4} \alpha_i e^{-2\lambda_i^2 (k_2^2+k_3^2+k_2 k_3)} \sum_{j=1}^{N} e^{-i(2\pi/a)[k_2(y_j-x_j)+k_3(z_j-x_j)]} \end{aligned} \tag{3.41}$$

where $\delta_{m,n}$ is the Kronecker delta. With the ion positions (x_j, y_j, z_j) in a cubic diamond lattice given in Table 3.2,

$$\sum_{j=1}^{N} e^{-i(2\pi/a)[k_2(y_j-x_j)+k_3(z_j-x_j)]} = \begin{cases} 0\,, & \text{for } k_2 = \text{odd} \quad \text{or} \quad k_3 = \text{odd} \\ 8\,, & \text{for } k_2 = \text{even and } k_3 = \text{even} \end{cases} \tag{3.42}$$

Let $k_2 = 2l_1$ and $k_3 = 2l_2$ and Eq. (3.41) becomes

$$v_{n_1 n_2} = -\frac{16\pi\hbar^2}{m v_0} \sum_{l_1=-\infty}^{\infty} \sum_{l_2=-\infty}^{\infty} \delta_{2(2l_1+l_2),n_1}\, \delta_{6l_2,n_2} \sum_{i=1}^{4} \alpha_i e^{-8\lambda_i^2 (l_1^2+l_2^2+l_1 l_2)} \tag{3.43}$$

where $v_{n_1 n_2} \neq 0$ only when $n_1 = 2(2l_1 + l_2)$ and $n_2 = 6l_2$, where l_2 and $2l_1 + l_2$ are any positive or negative integers. Because the periodicity of $v_{n_1 n_2} \neq 0$ is 2 for n_1 and 6 for n_2, the periodicity of the lattice potential on the beam transverse plane is reduced from the original (b_1, b_2) in Eq. (3.38) to

$$a_x = b_1/2 = a/\sqrt{2} \qquad \text{and} \qquad a_y = b_2/6 = a/\sqrt{6} \tag{3.44}$$

and

$$V(x,y) = \sum_{m_1=-\infty}^{\infty} \sum_{m_2=-\infty}^{\infty} \tilde{v}_{m_1 m_2} \exp\left[i2\pi \left(\frac{m_1 x}{a_x} + \frac{m_2 y}{a_y} \right) \right] \tag{3.45}$$

where

$$
\begin{aligned}
\tilde{v}_{m_1 m_2} &= -\frac{16\pi\hbar^2}{m v_0} \sum_{l_1=-\infty}^{\infty} \sum_{l_2=-\infty}^{\infty} \delta_{(2l_1+l_2),m_1}\, \delta_{l_2,m_2} \sum_{i=1}^{4} \alpha_i e^{-8\lambda_i^2 (l_1^2+l_2^2+l_1 l_2)} \\
&= -\frac{16\pi\hbar^2}{m v_0} \sum_{l_1=-\infty}^{\infty} \delta_{2l_1,(m_1-m_2)} \sum_{i=1}^{4} \alpha_i e^{-2\lambda_i^2 (m_1^2+3m_2^2)} \\
&= \begin{cases} -\dfrac{16\pi\hbar^2}{m v_0} \displaystyle\sum_{i=1}^{4} \alpha_i e^{-2\lambda_i^2 (m_1^2+3m_2^2)}, & \text{for } \mod(m_1-m_2,2)=0 \\ 0, & \text{otherwise} \end{cases}
\end{aligned}
\tag{3.46}
$$

As shown in Fig.3.5, there are two identical potential wells that are centered at a diagonal line of a unit cell of $V(x,y)$ in the transverse plane. Since the periodicity of $V(x,y)$ along x and y direction are different in this case, a_x and a_y are the smallest periods of $V(x,y)$ along two orthogonal directions on the transverse plane and, therefore, $[\bar{1}10]$ and $[\bar{1}\bar{1}2]$ crystal axes are two orthogonal axes of the unit cell of the direct lattice in the transverse plane when the beam is channeling along the $[111]$ crystal direction.

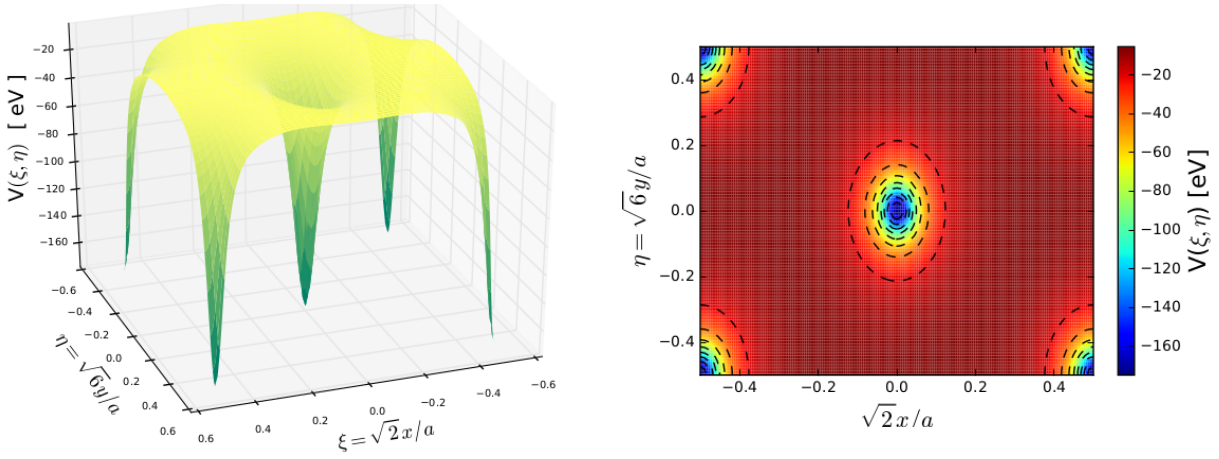

Figure 3.5: Lattice potential $V(x,y)$ on beam transverse plane for channeling of germanium with 9 MeV electron beam along [111] crystal direction.

3.5 Convergence in the Truncation of Fourier Series of $V(x,y)$ and Comparison with the Results from Axial Channeling Model

In all the cases, the lattice potential on the transverse plane is calculated in the form of

$$V(x,y) = \sum_{k_1=-\infty}^{\infty} \sum_{k_2=-\infty}^{\infty} v_{k_1 k_2} e^{i2\pi\left(k_1 x/a_x + k_2 y/a_y\right)} \tag{3.47}$$

where $v_{k_1 k_2}$ decays exponentially with k_1^2 and k_2^2 as

$$v_{k_1 k_2} \sim e^{-\gamma_1^2 k_1^2 - \gamma_2^2 k_2^2}$$

and γ_1 and γ_2 are constant. It is thus possible and numerically necessary to truncate the summations in Eq. (3.47) as

$$V(x,y) = \sum_{k_1=-k_{max}}^{k_{max}} \sum_{k_2=-k_{max}}^{k_{max}} v_{k_1 k_2} e^{i2\pi\left(k_1 x/a_x + k_2 y/a_y\right)} \tag{3.48}$$

The convergence of the truncation needs to be checked to ensure the accuracy of the calculated potential. To study the convergence, we calculated the difference of the potential calculated based on two difference truncations k_{max},

$$\text{Error-in-}V(k_{max}) = \frac{1}{a_x a_y} \int_0^{a_y} \int_0^{a_x} \left| \frac{V(x,y,k_{max})}{V(x,y,k_{max}+\Delta k_{max})} - 1 \right| dxdy \tag{3.49}$$

where $V(x,y,k_{max})$ and $V(x,y,k_{max}+\Delta k_{max})$ are lattice potential $V(x,y)$ calculated with a truncation of the Fourier series at k_{max} and $k_{max}+\Delta k_{max}$, respectively. Figure 3.6 plots this truncation error as a function of k_{max} for different cases of the channeling studied in this work and shows a quick convergence of the Fourier series of $V(x,y)$ in all the cases except the channeling in [110] crystal direction. For the case of the [110] direction, more Fourier expansion terms have to be kept, which requires more computer resource. In this study we used $k_{max} = 35$ in all the cases for convenience, which is adequate for the convergence of the Fourier expansion and can also be handled by modern

desktop computers. In Fig. 3.7, the lattice potential calculated with different k_{max} can be compared visually and it further confirms that the convergence of the truncation is achieved much faster at $k_{max} = 9$ and 13 for the cases of diamond and germanium along [001] crystal direction, respectively, and at a slower rate of $k_{max} = 25$ and 35 for the case of germanium along the [111] and [110] direction, respectively.

The lattice potential for the cases of [001] and [110] direction has previously been studied using the axial channeling model [3, 2] and the convergence of the Fourier expansion of $V(x,y)$ was suggested to be much faster than in our calculation for the same cases. With the axial channeling model, for example, the total number of terms needed for the Fourier expansion is only 631 in the case of germanium along the [110] direction [3], while our calculation requires $k_{max} = 35$ or larger for the convergence which yields a minimum of $(2k_{max}+1)^2 = 5041$ terms in the Fourier expansion of $V(x,y)$. It should be noted that the Fourier expansion coefficients $v_{k_1k_2}$ in Eq. (3.48) are calculated from an electron-ion interaction model without any approximation in our method. In the axial channeling model, however, $v_{k_1k_2}$ are calculated starting from the same electron-ion interaction model but approximately. Since the Fourier expansion of $V(x,y)$ is unique, the only explanation for a substantially smaller value of k_{max} in the axial channel model is that the approximation used in the axial channeling model may distort $v_{k_1k_2}$ significantly and the decay rate of $v_{k_1k_2}$ is significantly altered. The lattice potential calculated previously with the axial channeling model is, therefore, not reliable for studying the channeling radiation spectrum.

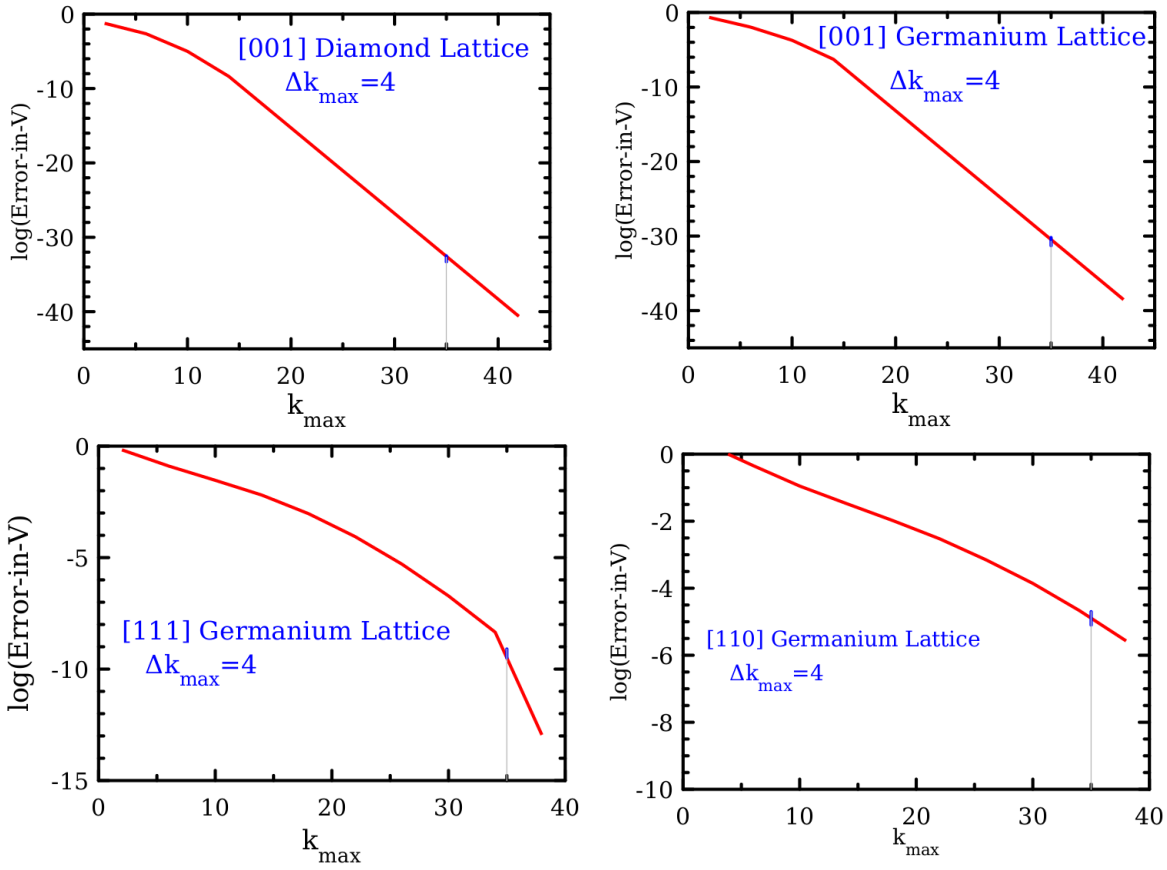

Figure 3.6: Truncation error of the Fourier expansion of $V(x,y)$ in Eq. (3.48) *v.s.* k_{max}, which is calculated using Eq. (3.49) with $\Delta k_{max} = 4$ for channeling of diamond along the [001] direction (top-left figure) and for channeling of germanium along [001] (top-right figure), [111] (bottom-left figure), and [110] (bottom-right figure) crystal direction, respectively. In the rest of this study, we used $k_{max} = 35$ that is marked with a vertical grey line in the figures.

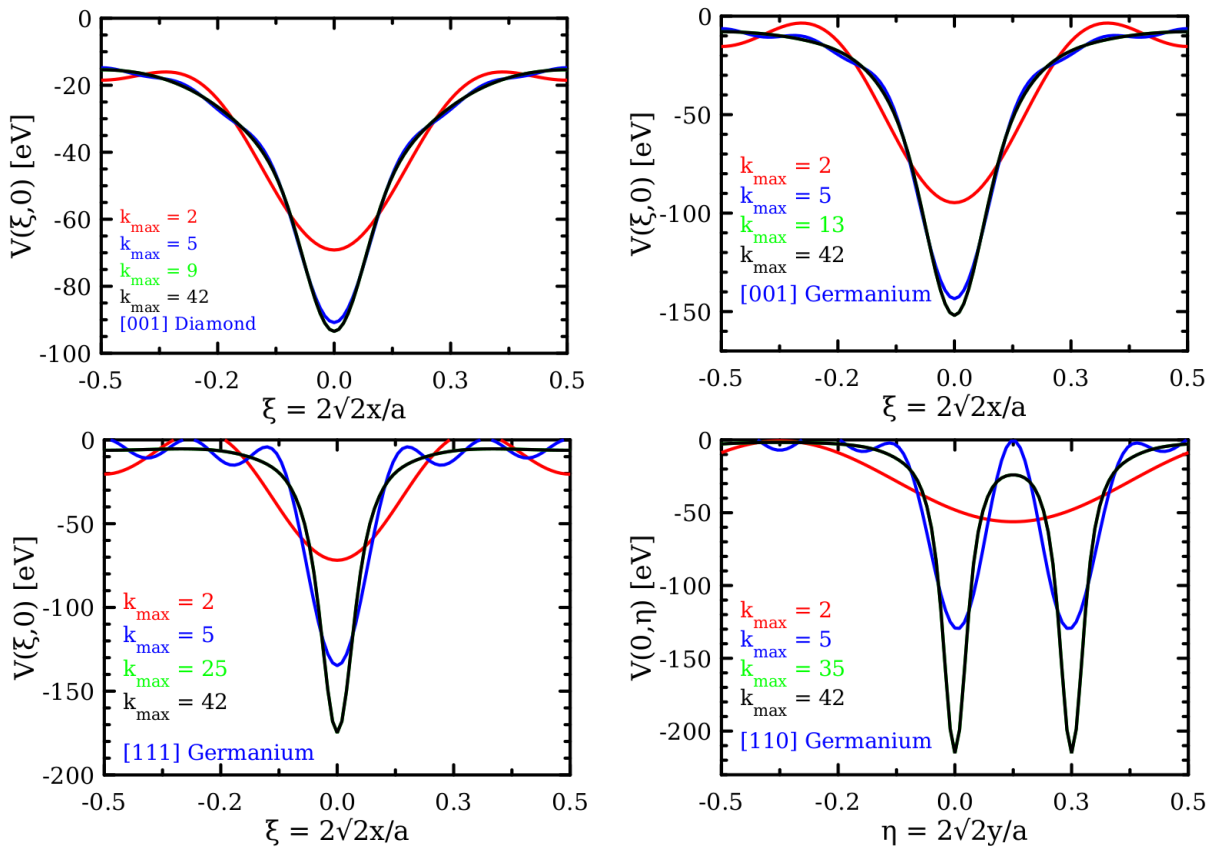

Figure 3.7: Lattice potential $V(\xi,\eta)$ with $\xi = x/a_x$ and $\eta = y/a_y$ in Eq. (3.48) calculated with different k_{max} for channeling of diamond along the [001] direction (top-left figure) and for channeling of germanium along [001] (top-right figure), [111] (bottom-left figure), and [110] (bottom-right figure) crystal direction, respectively. In all the cases, the curves with the two largest values of k_{max} overlap each other, which suggests the convergence of Eq. (3.48).

Chapter 4

Schroedinger Equation and Selection Matrix Construction and Spectrum Analysis

To understand the channeling radiation spectrum, in this chapter, the Bloch eigenstates for the transverse motion of beam electrons are calculated for an ultra-relativistic beam channeling through a crystal along [001], [110], and [111] crystal direction and the transition spectrum of the beam electrons between the eigenstates is studied. The transition spectrum has previously been studied for the cases of channeling along [001] and [110] direction [1, 2, 3]. Because of the use of a rotational symmetry approximation on the lattice potential in their analysis for the transition spectrum, however, the validity of the transition spectrum obtained in those studies is very limited. In our study, the Fourier expansion of the Bloch eigenstates on the two-dimensional transverse plane is solved numerically from the Schrödinger equation with a Fourier expansion of the lattice potential and without any additional approximation. With much more accurate solutions for the Bloch eigenstates, we discovered that the parity symmetry of the Bloch eigenfunctions determines the selection rule of the dipole transitions between the Bloch eigenstates in the cases of the channeling along [001] and [111] crystal direction. For the case of the channeling along [110] crystal direc-

tion, there is no systematic forbidden transition between the Bloch eigenstates due to a lack of sufficient symmetry in the lattice potential on the beam transverse plane. The transition probability was calculated for all the bounded Bloch eigenstates with a discretized mesh in the first Brillouin zone for the energy spectrum of the channeling radiation.

4.1 Eigenstates for the Transverse Motion of Beam Electrons in a Crystal Lattice

4.1.1 Lattice potential on the transverse plane in the beam rest frame

To solve the eigenstates of the transverse motion of beam electrons that travel with almost the speed of light in the longitudinal direction through a crystal, it is convenient to work in the rest frame of the beam. For that purpose, we need to transfer the lattice potential of the crystal on the beam transverse plane from the lab frame to the beam rest frame. Let the z-axis be the longitudinal direction and x and y be the coordinates on the transverse plane of the beam. The beam travels in the z direction with a relativistic velocity $(0,0,v_z \simeq c)$ in the lab frame. For an electron in the beam with velocity $\vec{v} = (v_x, v_y, v_z)$ in the lab frame, the motion on the beam transverse plane is non-relativistic, $v_x << c$ and $v_y << c$, while v_z is the velocity of the beam approximately. The Lorentz transformation for an electromagnetic field from the lab frame to the beam rest frame is [19, 20]

$$(\phi', \vec{A}') = (\gamma\phi - \beta\gamma A_z\,, A_x\,, A_y\,, \text{-}\beta\gamma\phi + \gamma A_z) \tag{4.1}$$

where $(\phi', \vec{A}')$ and $(\phi, \vec{A})$ are the electric scalar and magnetic vector potential in the beam rest frame and lab frame, respectively, β is the ratio of the beam speed to the speed of light, and $\gamma = 1/\sqrt{1-\beta^2}$. In the lab frame, the lattice potential of a crystal contains only the electric field and, therefore, $\vec{A} = 0$. With an ultra-relativistic beam, $\beta \simeq 1$ and

$$(\phi', \vec{A}') \simeq (\gamma\phi\,, 0\,, 0\,, -\gamma\phi) \tag{4.2}$$

Since the beam electrons travel with almost the speed of light in the longitudinal direction, the perturbation from the lattice potential results in little effect on the longitudinal motion of the electrons. As the beam electrons move non-relativistically in the beam transverse plane, the lattice potential could perturb the transverse motion of the electrons significantly when the beam passes through a crystal. For the transverse motion of the electrons, the Lorentz force in the rest frame can be written as

$$(F'_x, F'_y) = e\left(\nabla\phi' + \frac{\vec{v}'}{c} \times \nabla \times \vec{A}'\right)_{x,y} \simeq -\gamma e\,(\partial_x, \partial_y)\,\phi \tag{4.3}$$

where $\vec{v}' = (v_x, v_y, 0)$ is the velocity of the electrons in the beam rest frame. In the beam rest frame, therefore, the lattice potential for the transverse motion of the electrons is simply boosted by the relativistic factor γ of the beam,

$$V'(x,y) \simeq \gamma V(x,y) \tag{4.4}$$

where $V(x,y) = e\phi(x,y)$ is the lattice potential of a crystal in the beam transverse plane in the lab frame.

4.1.2 Schrödinger equation for the transverse motion of beam electrons in a crystal lattice

In the beam rest frame, the Hamiltonian for the transverse motion of the electrons of an ultra-relativistic beam in a crystal is

$$H(x,y,p_x,p_y) = \frac{1}{2m_e}\left(p_x^2 + p_y^2\right) + \gamma V(x,y)\,, \tag{4.5}$$

where $V(x,y)$ is the lattice potential of a crystal in the beam transverse plane in the lab frame, and the corresponding Schrödinger equation is

$$-\left(\frac{\hbar^2}{2m_e}\right)\left[\frac{d^2\Psi(x,y)}{dx^2} + \frac{d^2\Psi(x,y)}{dy^2}\right] + \gamma V(x,y)\Psi(x,y) = E\Psi(x,y) \tag{4.6}$$

Because of the periodicity of the crystal lattice, $V(x,y)$ is a periodic potential in the transverse (x-y) plane of the beam. Let a_x and a_y be the minimum periodicity of $V(x,y)$ in the x and y direction, respectively, *i.e.*

$$V(x,y) = V(x+a_x,y) = V(x,y+a_y) \tag{4.7}$$

where a_x and a_y are the lattice constants of the primitive cell (minimum-area cell) of a two-dimensional lattice that is the projection of the original three-dimensional crystal lattice to the beam transverse plane (see Chapter 3). With a periodic potential, the solution of the Schrödinger equation must be in the form of Bloch eigenfunctions (Bloch theorem) [21],

$$\Psi(x,y) = \frac{1}{2\pi} u(x,y) e^{i(\Omega_x x + \Omega_y y)} \tag{4.8}$$

where $u(x,y)$ has the period of $V(x,y)$, *i.e.* $u(x,y) = u(x+a_x,y) = u(x,y+a_y)$,

$$(\Omega_x\,,\,\Omega_y) = 2\pi\left(\frac{l_1}{Na_x}\,,\,\frac{l_2}{Na_y}\right) \qquad \forall\ (l_1,l_2) = 0,\pm1,\pm2,\ldots \tag{4.9}$$

is called crystal wave vector and N is the number of the primitive cells along either the x or y axis of the two-dimensional lattice on the beam transverse plane. Since $N \to \infty$, l_1/N and l_2/N are in fact continuous in a range of $(-\infty,\infty)$. It should be noticed that a_x and a_y have to be determined with the potential function $V(x,y)$ as detailed in Chapter 3 and may not necessarily be the same as the lattice periodicity on a crystal plane of the original three-dimensional crystal because of the projection. The correct identification of a_x and a_y is important to solving the eigenstates of the Schrödinger equation. Some of previous works [4] mistakenly used the periodicity of the crystal plane of the original three-dimensional lattice and, consequently, the eigenstates they obtained could be wrong.

Since u(x,y) is a periodic function, it can be expanded into a Fourier series of

$$u(x,y) = \sum_{k_2=-\infty}^{\infty}\sum_{k_1=-\infty}^{\infty} C_{k_1,k_2} e^{i2\pi(k_1 x/a_x + k_2 y/a_y)} \tag{4.10}$$

and the Bloch eigenfunctions in Eq. (4.8) can be rewritten as

$$\begin{aligned}\Psi &= \frac{1}{2\pi}\sum_{k_2=-\infty}^{\infty}\sum_{k_1=-\infty}^{\infty} C_{k_1,k_2}\, e^{i2\pi[(k_1+k_x+Q_1)x/a_x+(k_2+k_y+Q_2)y/a_y]} \\ &= \frac{1}{2\pi}\sum_{n_2=-\infty}^{\infty}\sum_{n_1=-\infty}^{\infty} C_{n_1-k_x,n_2-k_y}\, e^{i2\pi[(n_1+Q_1)\xi+(n_2+Q_2)\eta]} \end{aligned} \tag{4.11}$$

where $(l_1,l_2)/N = (k_x+Q_1, k_y+Q_2)$, k_x and k_y are integers, (Q_1,Q_2) are the fractional part of $(l_1,l_2)/N$, $(n_1,n_2) = (k_1+k_x, k_2+k_y)$, and $(\xi,\eta) = (x/a_x, y/a_y)$ are the coordinate on the beam transverse plane scaled with the lattice constant. It is convenient to choose (k_x,k_y) in such way that Q_1 and Q_2 are in the first Brillouin zone,

$$-\frac{1}{2} \le (Q_1, Q_2) < \frac{1}{2} \tag{4.12}$$

With the lattice potential in the Fourier expansion of (see Chapter 3),

$$V(\xi,\eta) = \sum_{k_2=-\infty}^{\infty}\sum_{k_1=-\infty}^{\infty} V_{k_1k_2}\, e^{i2\pi(k_1\xi+k_2\eta)} \tag{4.13}$$

and the Bloch eigenfunction in Eq. (4.11), the Schrödinger equation in Eq. (4.6) can be written as a Fourier expansion of

$$\begin{aligned}&\sum_{k_1,k_2=-\infty}^{\infty}\left[(k_1+Q_1)^2+\left(\frac{a_x}{a_y}\right)^2(k_2+Q_2)^2\right] C_{k_1-k_x,k_2-k_y}\, e^{i2\pi(k_1\xi+k_2\eta)} \\ &\qquad + \sum_{l_1,l_2=-\infty}^{\infty}\tilde{V}_{l_1l_2}\sum_{k_1,k_2=-\infty}^{\infty} C_{k_1-k_x,k_2-k_y}\, e^{i2\pi[(l_1+k_1)\xi+(l_2+k_2)\eta]} \\ = \;& \frac{E}{\varepsilon}\sum_{k_1,k_2=-\infty}^{\infty} C_{k_1-k_x,k_2-k_y}\, e^{i2\pi(k_1\xi+k_2\eta)} \end{aligned} \tag{4.14}$$

where $\varepsilon = \hbar^2/(2m_e a_x^2)$ and $\tilde{V}_{l_1l_2} = \gamma V_{l_1l_2}/\varepsilon$. With the orthogonal condition of $e^{i2\pi(k_1\xi+k_2\eta)}$, Eq.

(4.14) can be expressed as an infinite-dimensional matrix equation,

$$\left[(k_1+Q_1)^2+\left(\frac{a_x}{a_y}\right)^2(k_2+Q_2)^2-\frac{E}{\varepsilon}\right]C_{k_1-k_x,k_2-k_y}=-\sum_{l_1,l_2=-\infty}^{\infty}\tilde{V}_{k_1-l_1,k_2-l_2}C_{l_1-k_x,l_2-k_y} \quad (4.15)$$

Since this equation does not depend on k_x and k_y, the eigenfunction $\left\{C_{k_1-k_x,k_2-k_y}\,\middle|\,k_1,k_2\right\}$ and eigen-energy E are independent of (k_x,k_y) and, therefore, only the case of $k_x=k_y=0$ is needed. Note that Ψ with $k_x=k_y=0$ are the Bloch eigenfunctions in the first Brillouin zone. To solve Eq. (4.15), the infinite-dimensional matrix $V_{k_1k_2}$ needs to be truncated. As shown in Chapter 3, $V_{k_1k_2}$ decays exponentially with k_1 and k_2 in a Gaussian function and the expansion of the lattice potential can be truncated at $k_1=k_{max}$ or $k_2=k_{max}$. Hence, the Bloch eigenfunction in Eq. (4.11) can be truncated at k_{max} as

$$\Psi=\frac{1}{2\pi}\sum_{k_2=-k_{max}}^{k_{max}}\sum_{k_1=-k_{max}}^{k_{max}}C_{k_1,k_2}\,e^{i2\pi[(k_1+Q_1)\xi+(k_2+Q_2)\eta]} \quad (4.16)$$

where $k_x=k_y=0$ in Eq. (4.11). With the truncation and $k_x=k_y=0$, the Schrödinger equation in Eq. (4.15) becomes a $(2k_{max}+1)^2$-dimensional matrix equation,

$$\sum_{l_1,l_2=-k_{max}}^{k_{max}}\left\{\left[(k_1+Q_1)^2+\left(\frac{a_x}{a_y}\right)^2(k_2+Q_2)^2-\frac{E}{\varepsilon}\right]\delta_{l_1k_1}\delta_{l_2k_2}+\tilde{V}_{k_1-l_1,k_2-l_2}\right\}C_{l_1,l_2}=0 \quad (4.17)$$

where $-k_{max}\le(k_1,k_2)\le k_{max}$. Equation (4.17) is an eigenvalue problem,

$$\mathscr{M}\cdot\mathbf{v}=\lambda\mathbf{v} \quad (4.18)$$

where $\lambda = E/\varepsilon$, $\mathbf{v}$ is a $(2k_{max}+1)^2$-dimensional vector

$$\begin{aligned}\mathbf{v} \;=\; \big(&C_{-k_{max},-k_{max}}\,,\, C_{-(k_{max}-1),-k_{max}}\,,\cdots,\, C_{(k_{max}-1),-k_{max}}\,,\, C_{k_{max},-k_{max}},\\ &C_{-k_{max},-(k_{max}-1)}, \qquad\qquad \cdots \qquad\qquad C_{k_{max},-(k_{max}-1)},\\ &\cdots\\ &C_{-k_{max},k_{max}}, \qquad\qquad \cdots \qquad\qquad C_{k_{max},k_{max}}\big)^T\,,\end{aligned}$$

and $\mathscr{M}$ is a $(2k_{max}+1)^2 \times (2k_{max}+1)^2$ matrix

$$\mathscr{M}_{ij} = \left[(k_1+Q_1)^2 + \left(\frac{a_x}{a_y}\right)^2 (k_2+Q_2)^2\right]\delta_{l_1k_1}\delta_{l_2k_2} + \tilde{V}_{k_1-l_1,k_2-l_2}$$

with

$$\begin{aligned} i &= (2k_{max}+1)(l_2+k_{max}) + (l_1+k_{max}+1)\\ j &= (2k_{max}+1)(k_2+k_{max}) + (k_1+k_{max}+1)\end{aligned}$$

The eigenenergies $E_n(\vec{Q})$ and eigenvectors $\{C_{k_1k_2}(\vec{Q},n)\}$ with $n = 1,\cdots,(2k_{max}+1)^2$ can be obtained by diagonalizing $\mathscr{M}$ at different values of (Q_1,Q_2) numerically. It should be noted that the choice of k_{max} needs to be tested for numerical convergence and depends on the type of crystal as well as the beam channeling direction. For diamond, for example, $k_{max} = 9$ is found to be sufficient when the beam is channeling in [001] crystal direction. For germanium, on the other hand, $k_{max} = 35$ is needed for the numerical convergence when the channeling is in [110] crystal direction. For this study, we used a C++ library for linear algebra called Armadillo for the diagonalization of $\mathscr{M}$ [22]. Since Eq. (4.17) is symmetric for the reflection of Q_1 or Q_2, $Q_1 \longrightarrow -Q_1$ or $Q_2 \longrightarrow -Q_2$, the Bloch eigenfunction $u(x,y)$ and eigenenergy E are the same for the positive and negative values of (Q_1,Q_2) and, therefore, solving the Schrödinger equation needs to be done for each value of (Q_1,Q_2) in the first quadrant of the Brillouin zone, $(Q_1,Q_2) \in [0,1/2] \otimes [0,1/2]$.

The normalization and orthogonal condition of the Bloch eigenfunctions is

$$\begin{aligned}
\left\langle \vec{Q}',m \middle| \vec{Q},n \right\rangle &= \sum_{k_1,k_2}\sum_{l_1,l_2} C_{k_1,k_2}(\vec{Q},n)C^*_{l_1,l_2}(\vec{Q}',m) \\
&\qquad \times \frac{1}{2\pi}\int_{-\infty}^{\infty} e^{i2\pi\left(k_1-l_1+Q_1-Q'_1\right)\xi}\,d\xi\ \frac{1}{2\pi}\int_{-\infty}^{\infty} e^{i2\pi\left(k_2-l_2+Q_2-Q'_2\right)\eta}\,d\eta \\
&= \sum_{k_1,k_2}\sum_{l_1,l_2} C_{k_1,k_2}(\vec{Q},n)C^*_{l_1,l_2}(\vec{Q}',m)\delta(k_1-l_1+Q_1-Q'_1)\delta(k_2-l_2+Q_2-Q'_2) \\
&= \sum_{k_1,k_2}\sum_{l_1,l_2} C_{k_1,k_2}(\vec{Q},n)C^*_{l_1,l_2}(\vec{Q}',m)\,\delta_{k_1l_1}\delta_{k_2l_2}\delta\left(Q_1-Q'_1\right)\delta\left(Q_2-Q'_2\right) \\
&= \delta_{nm}\,\delta\left(Q_1-Q'_1\right)\delta\left(Q_2-Q'_2\right)
\end{aligned} \tag{4.19}$$

where $\vec{Q}=\vec{Q}'$ and $\vec{k}=\vec{l}$ because (Q_1, Q_2) and (Q'_1, Q'_2) are fractions while $\vec{l}$ and $\vec{k}$ are integer vectors. The normalization and orthogonal condition of the Bloch eigenstates thus requires

$$\sum_{k_1,k_2=-k_{max}}^{k_{max}} C_{k_1,k_2}(\vec{Q},n)\,C^*_{k_1,k_2}(\vec{Q},m) = \mathbf{v}_n^T\cdot\mathbf{v}_m = \delta_{nm} \tag{4.20}$$

where $\mathbf{v}_m$ is the mth eigenvector of Eq. (4.18).

4.1.3 Numerical results of eigenenergies and eigenfunctions

We have studied several cases of the beam channeling with different beam energy, different channeling direction, and different crystal. The results are compared with all the available data from previous studies by Klein and Chouffani [2, 9]. Table 4.1 lists the parameters of the beam and crystal used in our study.

Table 4.1: Crystals, channeling directions, and beam energies (MeV) used in this study, where a_x and a_y are the lattice constants of the primitive cell of the two-dimensional lattice on the beam transverse plane and a is the lattice constant of the crystal cubic lattice.

crystal	beam direction	a_x	a_y	beam energy
diamond	[001]	$a/\sqrt{8}$	$a/\sqrt{8}$	16.9 30.5 54.5
germanium	[001]	$a/\sqrt{8}$	$a/\sqrt{8}$	9.0
	[110]	$a/\sqrt{2}$	a	9.0
	[111]	$a/\sqrt{2}$	$a/\sqrt{6}$	9.0

4.1.3.1 Numerical errors in solving matrix equation (4.18)

To solve the Bloch eigenstates from Eq. (4.18), one needs to diagonalize a large hermitian matrix $\mathscr{M}$ numerically. The numerical error needs to be checked to ensure the accuracy of the obtained eigenstates and the orthogonality of the obtained eigenvectors. The normalization and orthogonal condition of the eigenvectors $\{\mathbf{v}_n\}$ of $\mathscr{M}$ is $\langle \mathbf{v}_m | \mathbf{v}_n \rangle = \delta_{mn}$ where δ_{mn} is the Kronecker delta. We thus measure the orthogonal and normalization error by

$$\text{orthogonal error} = |\langle \mathbf{v}_m | \mathbf{v}_n \rangle| , \qquad \forall\ m \neq n \tag{4.21}$$

$$\text{normalization error} = |\langle \mathbf{v}_m | \mathbf{v}_m \rangle - 1| \tag{4.22}$$

To check the numerical convergence of the solution of Eq. (4.18), we measure how close a numerical approximation of an eigenstate with which $\mathscr{M}\mathbf{v}_m \approx \lambda_m \mathbf{v}_m$ is to an exact eigenstate with which $\mathscr{M}\mathbf{v}_m = \lambda_m \mathbf{v}_m$. We define the convergence error as

$$\text{convergence error} = \left| \frac{1}{\lambda_m} \langle \mathbf{v}_m | \mathscr{M} | \mathbf{v}_m \rangle - 1 \right| \tag{4.23}$$

Figures (4.1, 4.2, 4.3) plot the normalization, orthogonal, and convergence errors for different eigenstates calculated for the cases of 9 MeV beam channeling through germanium lattice along [001], [110], and [111] crystal direction. Since the eigenstates with a positive eigenenergy generally do not contribute to channeling radiation, all the eigenstates with a negative eigenenergy plus a few eigenstates with a positive eigenenergy are included in the figures. In all cases of three channeling directions, the average normalization errors are below 10^{-6} with standard deviations at 10^{-7} or smaller (see Fig. 1). The error is sufficiently small and, therefore, the numerically-obtained eigenstates is normalized. For the orthogonal error, we calculated the orthogonal condition between the ground state ($n = 1$) and the mth eigenstate. As shown in Fig. 2, the orthogonal error is below 10^{-6} in all the cases, which is sufficiently small to validate orthogonal condition. It can also be seen in Fig. 4.3 that the convergence error is less than 10^{-6} for all the obtained eigenstates, which is sufficiently small to satisfy convergence.

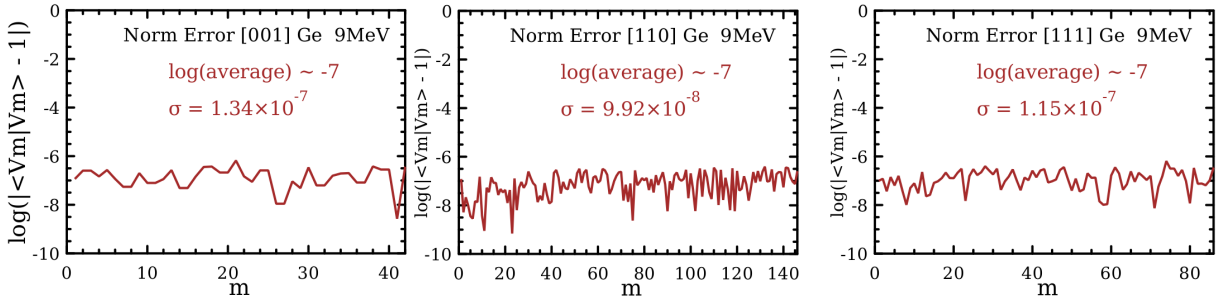

Figure 4.1: $\log|\langle \mathbf{v}_m|\mathbf{v}_m\rangle - 1|$ of the normalization error *v.s.* m of eigenstate $\mathbf{v}_m$ for the cases of 9 MeV beam channeling through germanium lattice along [001], [110], and [111] crystal direction. The average and standard deviation of the normalization error over all the eigenstates are $\sim 10^{-7} - 10^{-6}$ and $\sim 10^{-7}$, respectively.

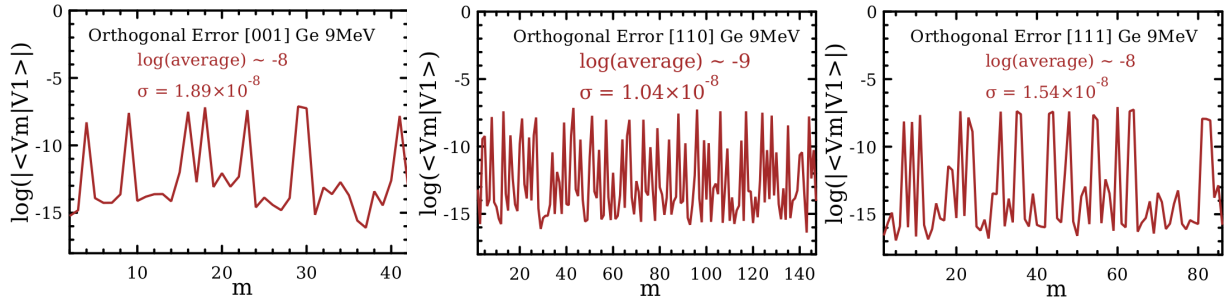

Figure 4.2: $\log|\langle \mathbf{v}_m|\mathbf{v}_n\rangle|$ of the orthogonal error with $n = 1$ (ground state) *v.s.* m of eigenstate $\mathbf{v}_m$ for the cases of 9 MeV beam channeling through germanium lattice along [001], [110], and [111] crystal direction.

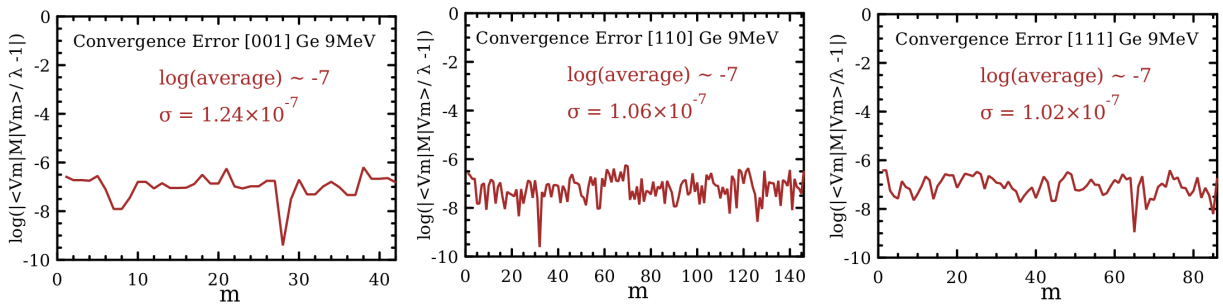

Figure 4.3: $\log\left(\left|\langle \mathbf{v}_m|\mathscr{M}|\mathbf{v}_m\rangle/\lambda_m - 1\right|\right)$ of the convergence error *v.s.* m of eigenstate $\mathbf{v}_m$ for the cases of 9 MeV beam channeling through germanium lattice along [001], [110], and [111] crystal direction. The average and standard deviation of the normalization error over all the eigenstates are $\sim 10^{-7} - 10^{-6}$ and $\sim 10^{-7}$, respectively.

4.1.3.2 Eigenenergy for the transverse motion of beam electrons channeling through a Crystal

In this section, we will study the energy spectrum for the transverse motion of beam electrons channeling through a crystal with different beam energy and different crystal orientation for the channeling. Note that the eigenstates with an energy that is below the maximum (top of the potential well) of lattice potential $V(x,y)$ are the bounded states and are relevant to the channeling radiation. The discussion will be focused on the bounded states.

a. Channeling through diamond along [001] crystal direction with different beam energy

In Fig. 4.4, the eigenenergies at $Q_1 = Q_2 = 0$ in the lab frame for channeling of diamond along [001] crystal direction were plotted for three different beam energy, 16.9 ($\gamma = 33.1$), 30.5 ($\gamma = 59.7$) and 54.5 MeV ($\gamma = 106.7$), respectively. To help us to visualize which eigenstates contribute to the channeling radiation, the lattice potential in the beam rest frame $\gamma V(\xi,\eta)$ as a function of $\xi = \eta$ was also plotted in Fig. 4.4, where the scaled variables $\xi = x/a_x$ and $\eta = y/a_y$ was used for convenience. Note that the beam electrons are in bounded (unbounded) states for their transverse motion if they are at eigenstates that have eigenenergies lower (higher) than the maximum of $\gamma V(\xi,\eta)$. The bounded states are the primary contributors to the channeling radiation. In this case, $\gamma V(\xi,\eta)$ reaches its maximum at the boundary of the unit cell of the lattice at $|\eta| = |\xi| = 1/2$ in

Fig. 4.4. As the beam energy increases, as shown in Fig. 4.4, the eigenenergies decrease (more negative) and the number of the bounded states increases. The increase of the bounded states provides more possibilities of photon emissions from the transitions between different bounded states. Moreover, the bounded states near the maximum of $\gamma V(\xi,\eta)$ becomes more and more dense as the beam energy increases and, consequently, the photon emission lines from those states could be bundled together to form a broadened spectral line. Figure 4.4 also shows that the energy separations between excited ($n > 1$) and ground ($n = 1$) state increases with the beam energy and, therefore, the photon emission lines shift toward higher energy as the beam energy increases. With the additional relativistic doppler effect, this energy increase of the radiation spectral lines with the beam energy is even more significant when the radiation is observed in the lab frame.

The channeling radiation of diamond lattice along [001] direction with those three cases of the beam energy has also been studied theoretically by Klein *et. al.* using axial channeling model [2]. As it has been discussed in Chapter 3, our calculation of the lattice potential is exact without any approximation from a model of single electron-ion interaction and more efficient mathematically as compared with the axial channeling model in which the potential was obtained approximately. In order to compare our result of the energy spectrum with Klein's prediction, the energy separations between excited ($n > 1$) states and the ground ($n = 1$) state are listed in Table 4.2, where the energy separations is calculated as

$$\Delta_n = (E_n - E_1)/\gamma \tag{4.24}$$

since the eigenenergy calculated in Klein's paper is E_n/γ with E_n being our notation of the eigenenergy. As shown in Table 4.2, the results from two different calculations are not close. The discrepancy is especially pronounced at the $n = 2$ and $n = 3$ states which is important to channeling radiation and becomes more significant as the beam energy increases. It should be noted that both calculations of the lattice potential and the numerical solution of the Bloch eigenstates can affect the accuracy of the result. In our case, the lattice potential is exactly calculated without any approximation from the model of single electron-ion interaction and the accuracy of the Bloch eigenstates was carefully checked by the error analysis in Section 4.1.3.1. Since the detail calculation of the

Bloch eigenstates was not discussed in Klein's paper, it is not clear whether any additional numerical approximations were used for solving the eigenstates and what the numerical accuracy is [2].

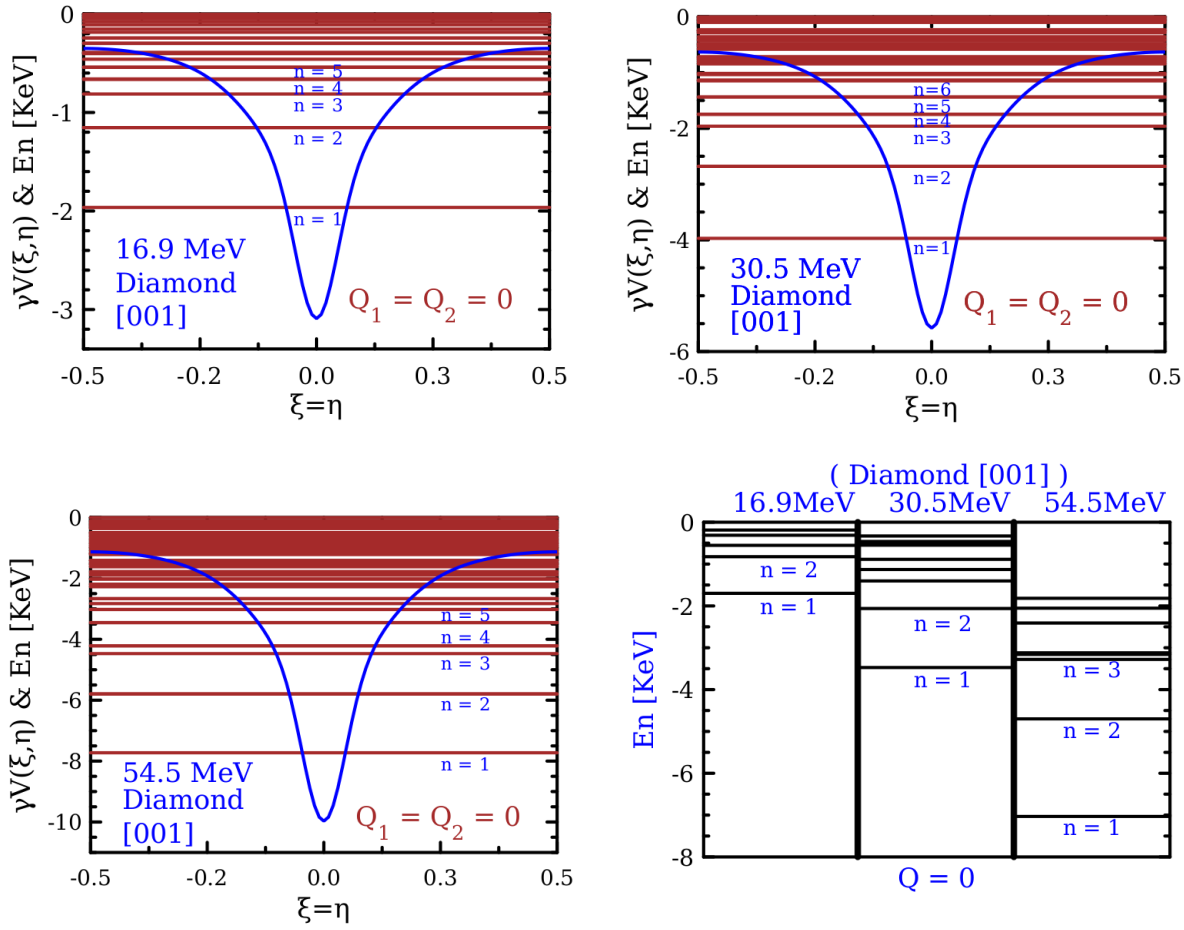

Figure 4.4: Three plots generated from our Generic Model: $\gamma V(\xi,\eta)\&E_n$ vs $\xi = \eta$. The red lines represent eigenenergies at $Q_1 = Q_2 = 0$ of the transverse motion in the beam rest frame for the channeling of diamond lattice along [001] crystal direction, where the beam energy is 16.9, 30.5, and 54.5 MeV, respectively. Blue curve is the lattice potential $\gamma V(\xi,\eta)$ in the beam rest frame as a function of $\xi = \eta$, where $\xi = x/a_x$ and $\eta = y/a_y$ with $a_x = a_y = a/\sqrt{8}$ and a being the diamond lattice constant. The fourth plot shows Klein's Axial Model's predicted eigenenergies, E_n [KeV], in black lines for the same three beam energies[2]. The cyan lines depict the maximum potential energy for the respective labframe potential. All eigenstates below these cyan lines are bounded states.

Table 4.2: Energy separations $\Delta_n = (E_n - E_1)/\gamma$ between the nth excited states and the ground state at $Q_1 = Q_2 = 0$ of the transverse motion in the beam rest frame for the channeling of diamond lattice along [001] crystal direction, where the beam energy is 16.9, 30.5, and 54.5 MeV, respectively. Columns labeled with "Klein" and "Our" are from Klein's paper and our generic model result, respectively, and the "difference" is the percentage difference of the results from two studies. The unit of Δ_n is eV.

	16.9 MeV			30.5 MeV			54.5 MeV		
	Klein	Ours	difference	Klein	Ours	difference	Klein	Ours	difference
Δ_2	26.46	24.49	8.0%	23.63	21.60	9.4%	21.86	18.12	20.7%
Δ_3	34.67	34.8	.4%	41.48	33.67	23.2%	49.23	30.53	61.3%
Δ_4	41.97	39.27	6.9%	39.26	37.25	5.4%	36.3	32.92	10.3%
Δ_5	45.71	39.44	15.9%	43.33	42.44	2.1%	36.67	40.07	8.5%

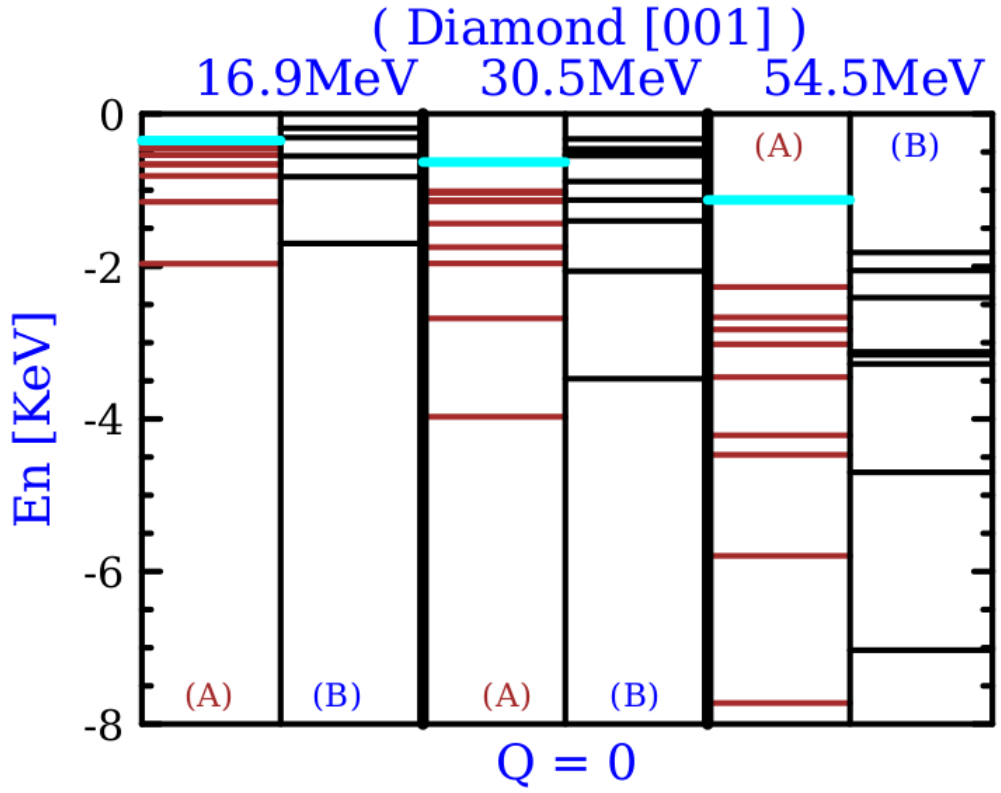

Figure 4.5: Visual comparision of Eigenenergies of our generic model depicted in red lines and Klein's predictions in black lines. For each beam energy 16.9, 30.5 and 54.5MeV, there are two columns: (A) and (B). Column (A) represents the Generic Model predicted eigenenergies in red lines. Column (B) is Klein's Axial Model's predicted eigenergies in black lines. $Q_1 = Q_2 = 0$ of the transverse motion in the beam rest frame diamond lattice along [001]. All Eigenenergies below the cyan line are bounded states.

Table 4.3: Eigenenergies E_n/γ at $Q_1 = Q_2 = 0$ of the transverse motion in the beam rest frame for the channeling of diamond lattice along [001] crystal direction, where the beam energy is 16.9, 30.5, and 54.5 MeV, respectively. Columns labeled with "Klein" and "Ours" are from Klein's paper and our generic model result, respectively. The unit of E_n is eV.

	16.9 MeV		30.5 MeV		54.5 MeV	
	Klein	Ours	Klein	Ours	Klein	Ours
E_1	-51.37	-59.38	-58.18	-66.53	-65.93	-72.437
E_2	-24.91	-34.88	-34.55	-44.93	-44.07	-54.33
E_3	-16.7	-24.58	-23.51	-32.86	-30.74	-41.91
E_4	-9.4	-20.11	-18.92	-29.29	-29.63	-39.52
E_5	-5.66	-19.94	-14.85	-24.09	-29.26	-32.37
E_6		-16.35	-8.81	-19.19	-22.59	-28.32
E_7		-13.90	-9.18	-18.98	-19.26	-26.51
E_8		-12.19	-7.69	-17.37	-17.04	-25.01
E_9		-11.85	-5.51	-17.00		-21.28

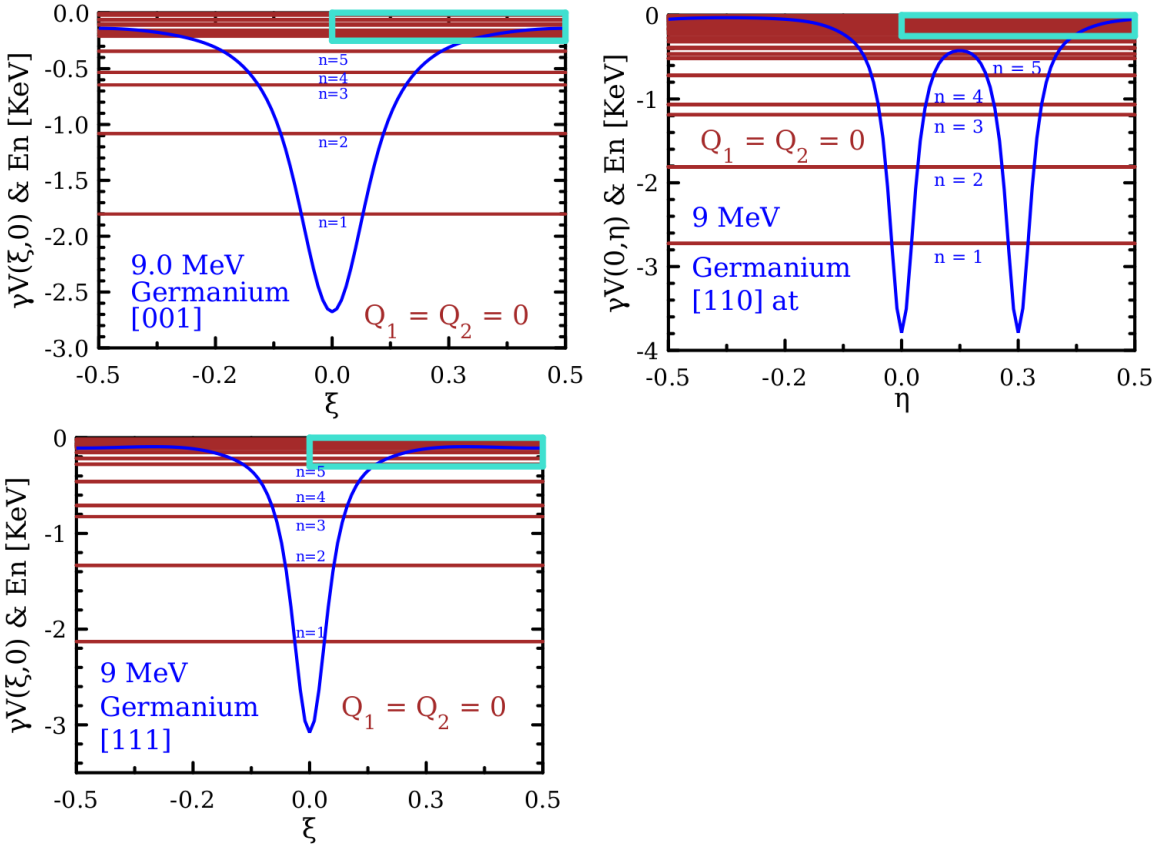

Figure 4.6: Eigenenergies (red lines) at $Q_1 = Q_2 = 0$ of the transverse motion in the beam rest frame for the channeling of germanium lattice along [001], [110], and [111] crystal direction, respectively. The beam energy is 9 MeV. Blue curve is the lattice potential $\gamma V(\xi,\eta)$ in the beam rest frame as a function of ξ at $\eta = 0$ or η at $\xi = 0$, where $\xi = x/a_x$ and $\eta = y/a_y$. The values of (a_x, a_y) are given in Table 1.

b. Channeling through germanium with 9 MeV beam along different crystal direction

To examine the effect of crystal orientation to the channeling radiation, we studied the cases of the channeling through germanium along [001], [110], and [111] crystal direction with 9 MeV beam energy. Figure 4.6 plots the calculated eigenenergies at $Q_1 = Q_2 = 0$. Note that the lattice potential for the [110] direction contains two potential wells in each unit cell ($-1/2 \leq \eta < 1/2$) of the lattice on the beam transverse plane and the potential wells are much deeper than that in the cases of the [001] and [111] direction. In the case of the [110] direction, as shown in Fig. 4.6, the energy separation between the excited states and the ground state is substantially larger as

compared with the other two cases and, consequently, the frequencies of the photon emission are much higher. Near the maximum of lattice potential $V(x,y)$, moreover, there are more bounded states densely bundled together to form a quasi energy band in the case of the [110] direction, which could result in a broadened photon emission line of the transition from those states to a lower energy eigenstate. The more bounded states in the case of the [110] direction also provide more possibilities of photon emissions. The case of the [110] crystal direction with 9 MeV beam is, therefore, very similar to the case of the [001] crystal direction with higher, such as 54.4 MeV, beam energy as it can be seen by comparing Figs. 4.4 and 4.6.

c. Degeneracy of eigenenergy states

The Bloch eigenenergy states are highly degenerate in general, especially in the cases of channeling along [111] and [110] crystal direction of diamond or germanium. Table 4.4 lists the number of degenerate states of the bounded Bloch eigenenergy states solved from Eq. (4.17) for the channeling of germanium with a 9 MeV beam along [001], [111], and [110] crystal direction, respectively. For the [111] case of the indexed eigenstate n = 7, it has a 4-fold degeneracy using a labeling convention, $n(i)$: 7(1), 7(2), 7(3) and 7(4) where i is the index of the sequential numbering of degeneracies within state u_n. Among those three cases, the [001] and [110] lattice potential are the least and most complicated, respectively, in terms of the number of potential wells in a unit cell and the degree of symmetry. The degree of degeneracy in the Bloch eigenstates is apparently related to the complexity of the lattice potential. The degeneracy of the eigenstates could be beneficial to channeling radiation by providing more possibilities of allowed transitions of beam electrons between different energy states.

Table 4.4: Number of degenerate states of the bounded Bloch eigenenergy states $u_{n(i)}$ at $Q_1 = Q_2 = 0$ for the channeling of germanium with a 9 MeV beam along [001], [111], and [110] crystal crystal direction, respectively, where $n = 1$ is of the ground state. For example, the [111] eigenstate at n = 7 has a 4-fold degeneracy.

n		1	2	3	4	5	6	7	8	9	10	11
degeneracy	[001]	1	2	1	2	2	1	2	2	2	1	4
	[111]	2	4	2	4	4	6	4	4	2	1	4
	[110]	4	8	4	8	8	8	4	8	2	8	4

d. $\vec{Q}$-Dependence of eigenenergy

In many cases in condensed matter physics, the energy bands for the electrons in crystals depend strongly on the crystal wave vector $\vec{Q}$ because the lattice potential is usually a small perturbation as compared with the kinetic energy of the electron [see Schrödinger equation in Eq. (4.14)]. In the case of the beam channeling, due to the relativistic motion of the beam the lattice potential $\gamma V(\xi,\eta)$ dominates the kinetic energy of the transverse motion of the beam electrons and, therefore, the energy eigenstates do not depend on $\vec{Q}$ significantly. This is especially true for those lower energy states ($n < 6$ of E_n) that are deep inside the lattice potential well and almost independent of $\vec{Q}$. For the eigenstates with energy near the maximum of $\gamma V(\xi,\eta)$, the $\vec{Q}$-dependence could become substantial. Figure 4.7 plots eigenenergy E_n with $n \geq 6$ as a function of Q_2 at $Q_1 = 0$ for the same system as in Fig. 4.6 and shows a very weak $\vec{Q}$ for all the bounded states. One common feature among of this weak $\vec{Q}$-dependence is that the eigenstates near the maximum of $\gamma V(\xi,\eta)$ become more degenerate as $\vec{Q}$ varies from the center ($\xi = \eta = 0$) to the boundary ($\xi = 1/2$ and/or $\eta = 1/2$) of the Brillouin zone. But this $\vec{Q}$-dependence of E_n is probably too weak to have any significant impact on the channeling radiation. Some studies [23, 24, 25], however, indicates that the beam electrons in those unbounded states could interact with the crystal lattice via some in-

elastic interaction mechanism and collapse down to a lower energy state (called rechanneling) and the beam electrons at bounded states could gain energy through some inelastic collision mechanism and jump to a unbound state (called dechannelling). It is unclear if the degeneracy of the eigenstates of bounded and unbounded states near the maximum of $\gamma V(\xi,\eta)$ have any significant impact on the rechanneling and dechanneling processes.

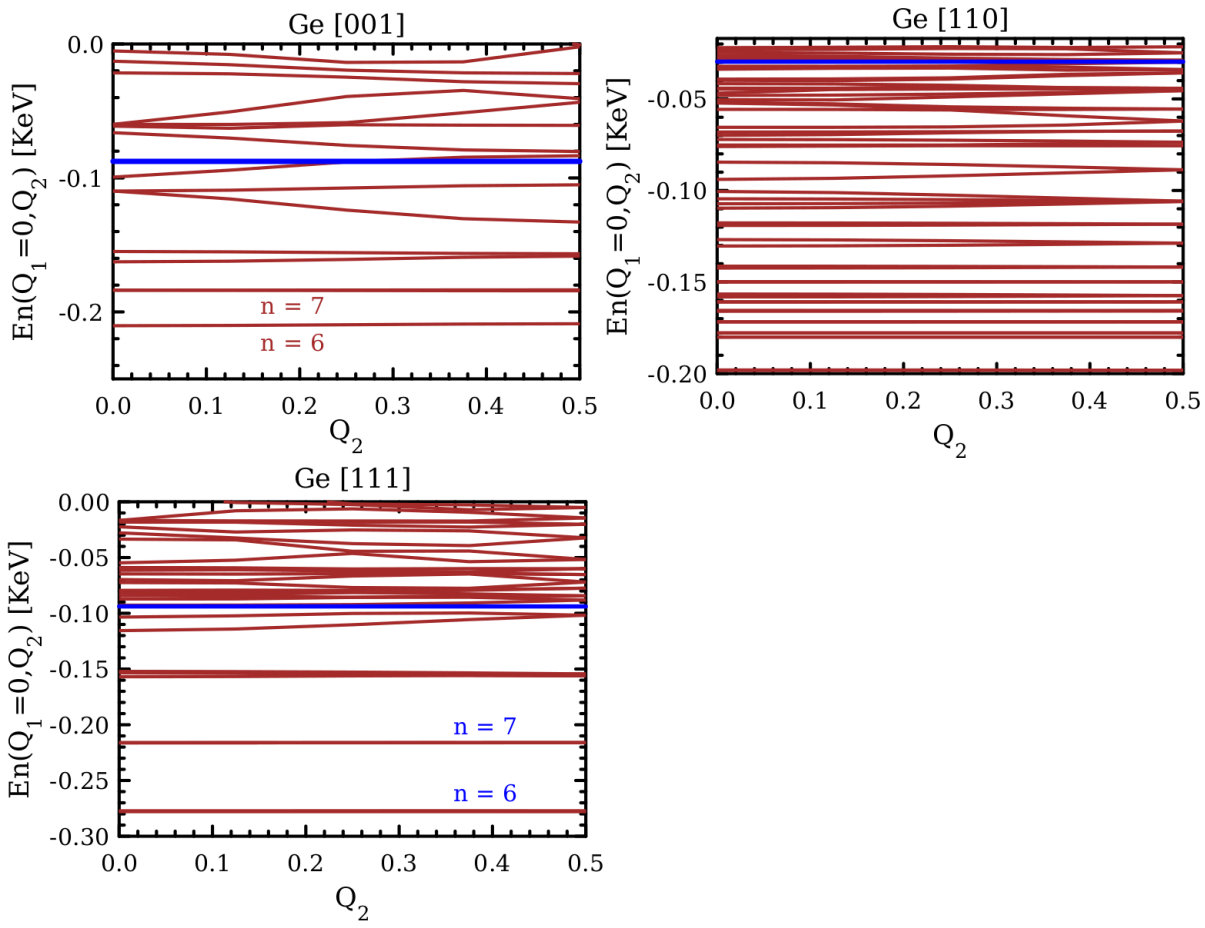

Figure 4.7: Eigenenergy E_n with $n > 6$ *vs*. Q_2 at $Q_1 = 0$ for the cases of Fig. 4.6. Note, the blue horizontal line depicts the maximum potential. All eigenstates depicted in red which are below the blue line are bounded states.

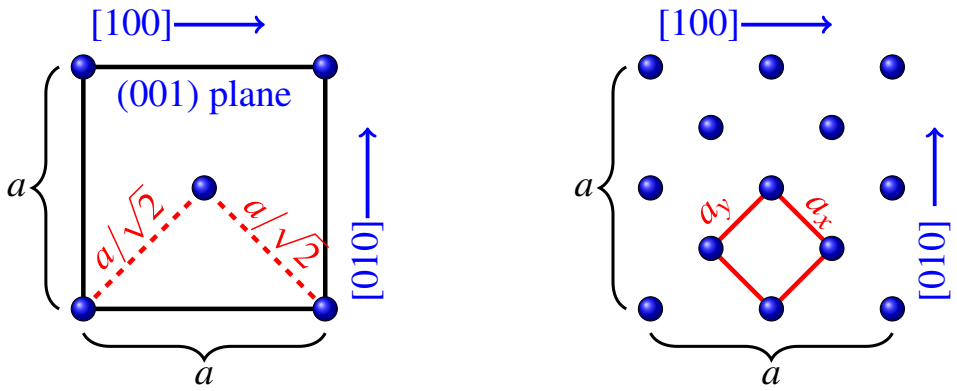

Figure 4.8: Left figure is a unit cell of (001) crystal plane of diamond and right figure is the projection of diamond crystal lattice onto the beam transverse plane that is parallel to (001) crystal plane, where a is the lattice constant of diamond, small red square in the right figure is the primitive cell on the transverse plane, and $a_x = a_y = a/\sqrt{8}$.

e. Effect of incorrect primitive cell for the lattice potential on the beam transverse plane

For the Bloch theorem, the primitive cell with lattice constants a_x and a_y on the beam transverse plane has to be correctly identified from the periodic lattice potential in order to solve the Bloch eigenstates correctly. Without a correct periodicity, the Fourier expansion of the Bloch eigenfunctions in Eq. (4.10) could be wrong. In our study, a_x and a_y have been carefully studied to ensure the primitive cell (see Chapter 3). Because of Lorentz contraction along the beam direction, the original three-dimensional crystal lattice is compressed into a two-dimensional lattice on the beam transverse plane, which is similar to a projection of a three-dimensional lattice onto a two-dimensional plane mathematically. Due to the projection, a_x and a_y of the two-dimensional lattice might not necessarily be the same as the periodicity on a crystal plane of the original three-dimensional lattice. In the case of beam channeling along [001] crystal direction of diamond, for example, the native periodicity on the (001) crystal plane is $a_x = a_y = a/\sqrt{2}$ for diamond, where a is the lattice constant of diamond. After the Lorentz contraction in the beam rest frame, the lattice constants of the primitive cell on the transverse plane is, however, $a_x = a_y = a/\sqrt{8}$ in this case. This reduction of the lattice constants can be understood as following. For the position of ions in diamond, the (001) planes rotate 45° and shift by $a/4$ in both [100] and [010] direction with

respect to each other within every group of four (001) crystal plane. When projecting all the (001) planes onto the transverse plane, as shown in Fig. 4.8, the number of ion sites on the transverse plane increases so that the lattice constants decreases.

One example of the misidentification of the primitive cell is in Azadegan 2006 paper [26] for the calculation of channeling radiation using planar channeling model. In the planar channeling model, the Bloch eigenstates are calculated approximately with a one-dimensional Schrödinger equation where a one-dimensional lattice potential was obtained by averaging the two-dimensional lattice potential along one of the transverse dimensions. In Azadegan's calculation, the lattice constant used for (110) planar channeling was $a/\sqrt{2}$ while the correct lattice constant should be $a/\sqrt{8}$ when the effect of the Lorentz contraction is included. To examine the effect of this mistake, we reproduced the Bloch eigenstates with the wrong periodicity and compared it with the correct ones. Figure 4.9 plots the eigenenergies for both the cases of (110) planar channeling of diamond calculated with the wrong ($a/\sqrt{2}$) and correct ($a/\sqrt{8}$) lattice constant, respectively. Two different beam energy, 14.6 and 54 MeV, were used in the calculation. As shown in Fig. 4.9, the use of a wrong periodicity in Bloch wavefunctions has little impact on the energy of the bounded states while the unbounded states are quite wrong. Note that the incorrect periodicity only affects the kinetic energy term in the Schrödinger equation [see Eq. (4.14)]. For the bounded states, the lattice potential is dominant the Hamiltonian and an incorrect lattice constant has very little effect on the calculated eigenstates. For the unbounded states, on the other hand, the kinetic energy term is dominant and an incorrect lattice constant leads to incorrect eigenstates. Since only bounded states are relevant to channeling radiation, it is accidental that a mistake in the periodicity of the Bloch eigenstates doesn't lead to any significant error in the energy spectrum for channeling radiation.

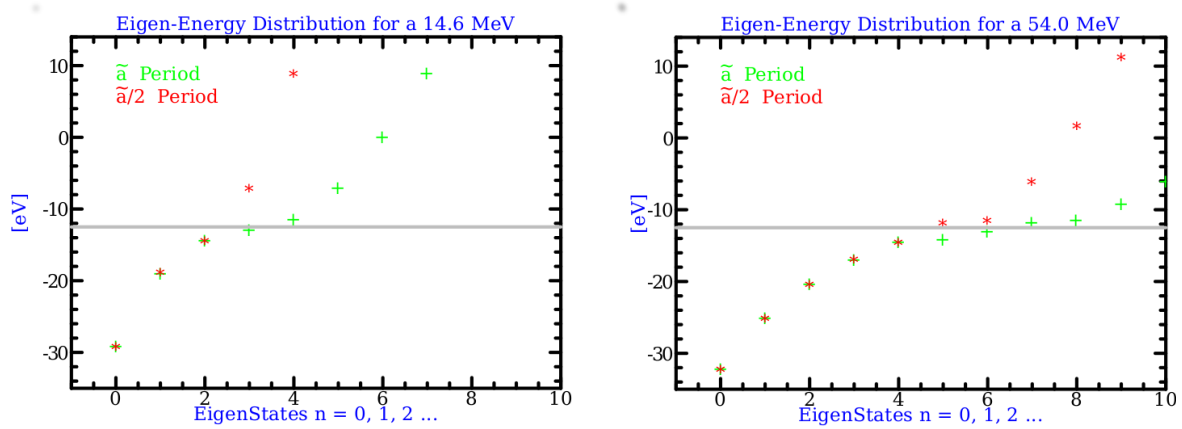

Figure 4.9: Eigenenergy E_n for the (110) planar channeling with 14.6 MeV (left figure) and 54 MeV (right figure) beam energy. Green crosses are calculated with the wrong lattice constant $a/\sqrt{2}$ and red stars are calculated with the correct lattice constant $a/\sqrt{8}$. The grey horizontal line indicates the maximum of the lattice potential.

4.1.3.3 Eigenfunction for the transverse motion of beam electrons channeling through a Crystal

The existence of any spatial symmetry in the Bloch eigenfunctions is important to the possibility of selection rules for transitions of beam electrons between the eigenstates, which in turn determines the radiation spectrum. Based on the axial channeling model, Chouffani, Genz, and Andersen have suggested that the rotational symmetry of the eigenfunctions on the transverse plane is the basic property for the channeling along the [001] and [111] direction by arguing that the first few eigenstates are deep inside the potential well, bounded with a single string of ions along the channeling direction and, therefore, very much localized [1, 3, 5]. With an approximation of the rotational symmetry for the bounded Bloch eigenstates, they suggested a transition selection rule for the photon emission of channeling radiation. Note that a single potential well in a unit cell for the channeling along the [001] and [111] direction is approximately rotational symmetric if it is near the bottom of the potential well. The question is, however, how localized the Bloch eigenfunctions are. Based on our study, we have concluded that the Bloch eigenfunctions, except the ground state, are not rotational symmetric under any reasonable approximation and the transition selection rule based on the rotational symmetry should not be use for the channeling radiation spectrum. In the

case of the channeling along the [110] direction, moreover, due to the existence of asymmetrical double wells in a unit cell in the lattice potential, the Bloch eigenfunctions do not have the rotational symmetry at all even at the ground state. Since the existence of the rotational symmetry is a major disagreement between our study and all the previous channeling radiation studies based on the axial channeling model, in the section, our discussion will be concentrated on the possibility of the rotational symmetry in the Bloch eigenfunctions. We will also show that the parity of the Bloch eigenfunctions is an important feature of the wavefunctions and is the primary reason of the transition selection rules for the channeling radiation.

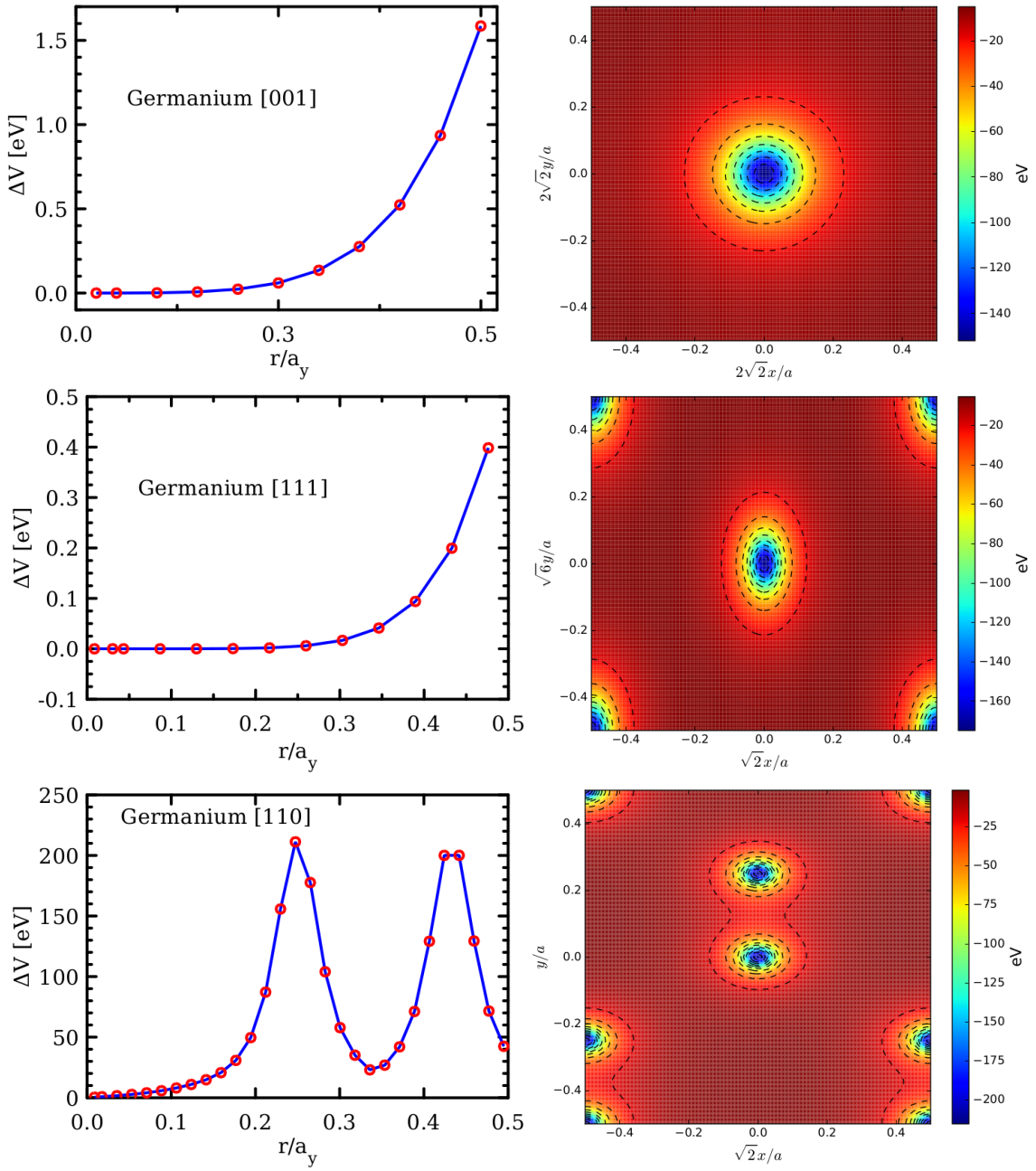

Figure 4.10: The maximal variation of the lattice potential ΔV defined in Eq. (4.25) as a function of r/a_x in a unit cell on the transverse plane (left figure) and the corresponding potential $V(x,y)$ in contour plot (right figure) for the channeling of germanium with a 9 MeV beam along [001], [111], and [011] crystal direction, respectively, where (a_x, a_y) are the lattice constants of the unit cell.

a. Possibility of the rotational symmetry in the lattice potential on the beam transverse plane

If a lattice potential is rotational symmetric approximately, it requires $V(x,y) = V(r,\phi) \simeq V(r)$, where $r = \sqrt{x^2+y^2}$ and $\phi = \tan^{-1}(y/x)$, $x \otimes y \in [-a_x, a_x) \otimes [-a_y, a_y)$, and a_x and a_y are the lattice constants of the unit cell of the lattice. To determine whether the potential has the rotational symmetry, we calculated the maximal variation of a potential with respect to ϕ at each given r, *i.e.*

$$\Delta V = \max_{\phi \in [0,2\pi)} [V(r,\phi)] - \min_{\phi \in [0,2\pi)} [V(r,\phi)] \tag{4.25}$$

Figure 4.10 plots ΔV as a function of r/a_x for the channeling of germanium with a 9 MeV beam along [001], [111], and [110] crystal direction, respectively. For a comparison with the variation of $V(x,y)$ in a unit cell on the transverse plane, the contours of $V(x,y) =$ constant are also included in Fig. 4.10. As shown in Fig. 4.10, in the cases of the channeling along the [001] and [111] direction, $V(x,y)$ is independent of ϕ approximately if $r < a_x/4$ but depends on ϕ substantially if $r > a_x/3$. In the case of the [111] direction, because of the additional potential wells at the four corners of the unit cell, the ϕ-dependence of $V(x,y)$ is especially strong if $r > a_x/2$. In the case of the channeling along the [110] direction, $V(x,y)$ depends on ϕ strongly in whole region of the unit cell. The rotational symmetry emphasized in the previous works [9, 5, 1] could therefore only be possible if the eigenfunctions are confined in the region of about $r < a_x/4$ in the case of the channeling along the [001] and [111] direction. Due to the existence of the additional potential wells in a unit cell in the case of the [111] direction, however, the Bloch eigenfunctions could spread into all the potential wells and be delocalized and, consequently, the eigenfunctions could be highly anisotropic on the transverse plane. Therefore, it is possible that only the case of the [001] direction could be a candidate of the rotational symmetry.

b. No rotational symmetry in the bounded Bloch eigenfunctions in general

If the lattice potential is approximately rotational symmetric in a unit cell, $V(x,y) \simeq V(r)$, the Schrödinger equation for the Bloch eigenstates at $Q_1 = Q_2 = 0$ can be written in the polar coordi-

nate (r,ϕ) on the transverse plane as

$$-\frac{\hbar^2}{2m}\left[\frac{1}{r}\frac{\partial}{\partial r}\left(r\frac{\partial}{\partial r}\right)+\frac{1}{r^2}\frac{\partial^2}{\partial\phi^2}\right]u_n(r,\phi)+V(r)u_n(r,\phi)=E_n u_n(r,\phi) \tag{4.26}$$

The eigenstates can thus be written by using the separation of variables as $u_n(r,\phi)=\mathscr{R}_{nl}(r)e^{il\phi}$ with $l=0,1,\cdots$ and the probability density $|u_n(r,\phi)|^2$ of the eigenstate is independent of ϕ (see Appendix A for a derivation of $u_n(r,\phi)$ using separation of variables). For the beam channeling problem, therefore, if the Schrödinger equation in Eq. (4.17) is rotationally symmetric approximately, the probability densities of the eigenstates solved from Eq. (4.17) should not depend on ϕ approximately.

Figures 4.11, 4.12, and 4.13 are the contour plots of probability density $|\Psi_n|^2$ of the Bloch eigenfunctions Ψ_n solved from the Schrödinger equation in Eq. (4.17) with $Q_1=Q_2=0$ for the cases of the channeling germanium with a 9 MeV beam along [001], [111], and [011] crystal direction, respectively, where all the states plotted are the bounded state and $n=1$ is of the ground state. In the case of the [001] direction, Ψ_n with $n=1$, 3, and 6 are approximately rotational symmetric, but among them at least Ψ_3 is not confined deep inside the potential well. Moreover, Ψ_n with $n=2$, 4, and 5 are not rotational symmetric. This irregularity of the apparent rotational symmetry in the wavefunctions cannot easily be explained using the axial channeling model [1, 5, 9] and the transition selection rules based on the rotational symmetry cannot be applied to all the bounded states which are important to channeling radiation. In the case of the channeling along the [111] direction, because of the potential wells at the center as well as corners of a unit cell, the eigenfunctions are nonzero inside all the wells and no rotational symmetry exist even at the ground state as shown in Fig. 4.11. As shown in Fig. 4.13, all the eigenstates in the case of the channeling along the [110] direction are highly anisotropic on the beam transverse plane. In conclusion, the rotational symmetry is not a basic symmetry of the system and the transition selection rules based on the rotational symmetry is not correct for the channeling radiation spectrum.

c. Parity symmetry of the Bloch eigenfunctions

In the cases of the channeling along [001] and [111] crystal direction, the lattice potential is an even function in the both x and y direction in a unit cell on the beam transverse plane, *i.e.* $V(x,y) = V(-x,y) = V(x,-y)$, and the Shrödinger equation is invariant under the reflection transformation in the both directions. The eigenfunctions could thus be an either even or odd function for the both coordinates, *i.e.*

$$\Psi(-\xi,\eta) = \pm\Psi(\xi,\eta) \qquad \text{and} \qquad \Psi(\xi,-\eta) = \pm\Psi(\xi,\eta)$$

For the case of the channeling along the [110] direction, the lattice potential is reflection symmetric only in the x direction ($[\bar{1}10]$ crystal direction) and, therefore, the eigenfunctions could be an either even or odd function in the x direction, *i.e.*

$$\Psi(-\xi,\eta) = \pm\Psi(\xi,\eta)$$

This parity symmetry of the eigenfunctions could determine the transition selection rules for the channeling radiation spectrum. For the Bloch eigenfunctions

$$\Psi_{n,Q_1,Q_2}(\xi,\eta) = \frac{1}{2\pi} u(\xi,\eta)\, e^{i2\pi(Q_1\xi + Q_2\eta)}$$

the even $(+)$ and odd $(-)$ parity in ξ and η require

$$\begin{cases} \Psi_{n,Q_1,Q_2}(-\xi,\eta) &= \pm\Psi_{n,-Q_1,Q_2}(\xi,\eta) \\ \Psi_{n,Q_1,Q_2}(\xi,-\eta) &= \pm\Psi_{n,Q_1,-Q_2}(\xi,\eta) \end{cases}$$

which yields

$$\begin{cases} u(-\xi,\eta) &= \pm u(\xi,\eta) \\ u(\xi,-\eta) &= \pm u(\xi,\eta) \end{cases}$$

Note that the eigenfunctions $u(\xi,\eta)$ and its associated eigenvenergies are independent of the signs

of Q_1 and Q_2, the reflection symmetry in the Brillouin zone of the Schrödinger equation, see Section (4.1.2), due to the reflection symmetry of a crystal lattice. For

$$\begin{aligned} u(\xi,\eta) &= \sum_{k_1=-k_{max}}^{k_{max}} \sum_{k_2=-k_{max}}^{k_{max}} C_{k_1,k_2}\, e^{i2\pi(k_1\xi+k_2\eta)} \\ u(-\xi,\eta) &= \sum_{k_1=-k_{max}}^{k_{max}} \sum_{k_2=-k_{max}}^{k_{max}} C_{k_1,k_2}\, e^{i2\pi(-k_1\xi+k_2\eta)} \\ &= \sum_{k_1=-k_{max}}^{k_{max}} \sum_{k_2=-k_{max}}^{k_{max}} C_{-k_1,k_2}\, e^{i2\pi(k_1\xi+k_2\eta)} \end{aligned}$$

Therefore, the parity symmetry of the Bloch eigenfunctions requires $C_{-k_1,k_2} = \pm C_{k_1,k_2}$ and $C_{k_1,-k_2} = \pm C_{k_1,k_2}$ for the even (+) or odd (−) parity in ξ and η, respectively. It should be noted that when an eigenstate u_n is degenerate, a numerically obtained eigenstate may not necessarily be an eigenstate of the parity operator and, therefore, not necessarily be an even or odd function, even through it can be since the Hamiltonian and the parity operators commute. We index a degenerate eigenstate as $u_{n(i)}$ where n is the label of the eigenstate and i indexes the degenerate state for state labeled n. As we discussed in Section 4.1.3.2c, the Bloch eigenstates solved from Eq. (4.17) are highly degenerate. From the contour plots of the probability density $|\Psi_n|^2$ of the Bloch eigenfunctions solved from Eq. (4.17), one can clear see the mirror symmetry of $|\Psi_n|^2$ in the x-y plane in the cases of the [001] and [111] direction and in the x direction alone in the case of the [110] direction (see Figs. 4.11, 4.12, and 4.13), which suggests a parity symmetry of u_n, where $\Psi_n(\xi,\eta) = u_n(\xi,\eta)\, e^{-i2\pi(Q_1\xi+Q_2\eta)}/2\pi$. Base on an argument of the continuity of u_n on the x-y plane, one can determine the parity of the eigenfunctions from the contour plots in most cases in Figs. 4.11, 4.12, and 4.13, but for a few cases the parity has to be determined by examining the symmetry in $\{C_{k_1,k_2}\}$ that are plotted in Fig. 4.14–4.20 for some examples. Table 4.5 lists the parity of $u_n(\xi,\eta)$ for the first few Bloch eigenstates for the channeling along [001] and [111] crystal direction and shows that they all have the defined parity. For the case of the channeling in [110] crystal direction, the parity symmetry exists in the y direction, but does not exist in the x direction because the asymmetry of of the lattice potential in that direction.

Table 4.5: Parity of the bounded Bloch eigenstates $u_{n(i)}$ at $Q_1 = Q_2 = 0$ for the channeling of germanium with a 9 MeV beam along [001] and [111] crystal direction, respectively, where $n = 1$ is of the ground state. The even (+) and odd (-) in x means $u_{n(i)}(-x,y) = u_{n(i)}(x,y)$ and $u_{n(i)}(-x,y) = -u_{n(i)}(x,y)$, respectively, and similar in the y direction. The numbers $n(i)$ represents the n_{th} eigenstate and (i_{th}) is the sequential numbering for all the degenerate eigenstates within the n_{th} state. For example in [001] case, the 1st excited state ($n = 2$) has two degenerate states that are labeled as 2(1) and 2(2), respectively.

	parity of $u_{n(i)}(x,y)$ for [001]	
$n(i)$	x	y
1(1)	even	even
2(1)	$u_{2(1)}(-x,-y) = +u_{2(1)}(x,y)$	
2(2)	$u_{2(2)}(-x,-y) = -u_{2(2)}(x,y)$	
3(1)	even	even
4(1)	even	even
4(2)	even	even
5(1)	$u_{5(1)}(-x,-y) = +u_{5(1)}(x,y)$	
5(2)	$u_{5(2)}(-x,-y) = -u_{5(2)}(x,y)$	
6(1)	even	even

	parity of $u_{n(i)}(x,y)$ for [111]	
$n(i)$	x	y
1(1)	even	even
1(2)	even	even
2(1)	even	odd
2(2)	even	odd
2(3)	odd	even
2(4)	odd	even
3(1)	even	even
3(2)	even	even
4(1)	odd	odd
4(2)	odd	odd
4(3)	even	even
4(4)	even	even
5(1)	odd	even
5(2)	even	odd
5(3)	even	odd
5(4)	odd	even
6(1)	even	odd
6(2)	odd	even
6(3)	even	odd
6(4)	odd	even
6(5)	even	even
6(6)	even	even

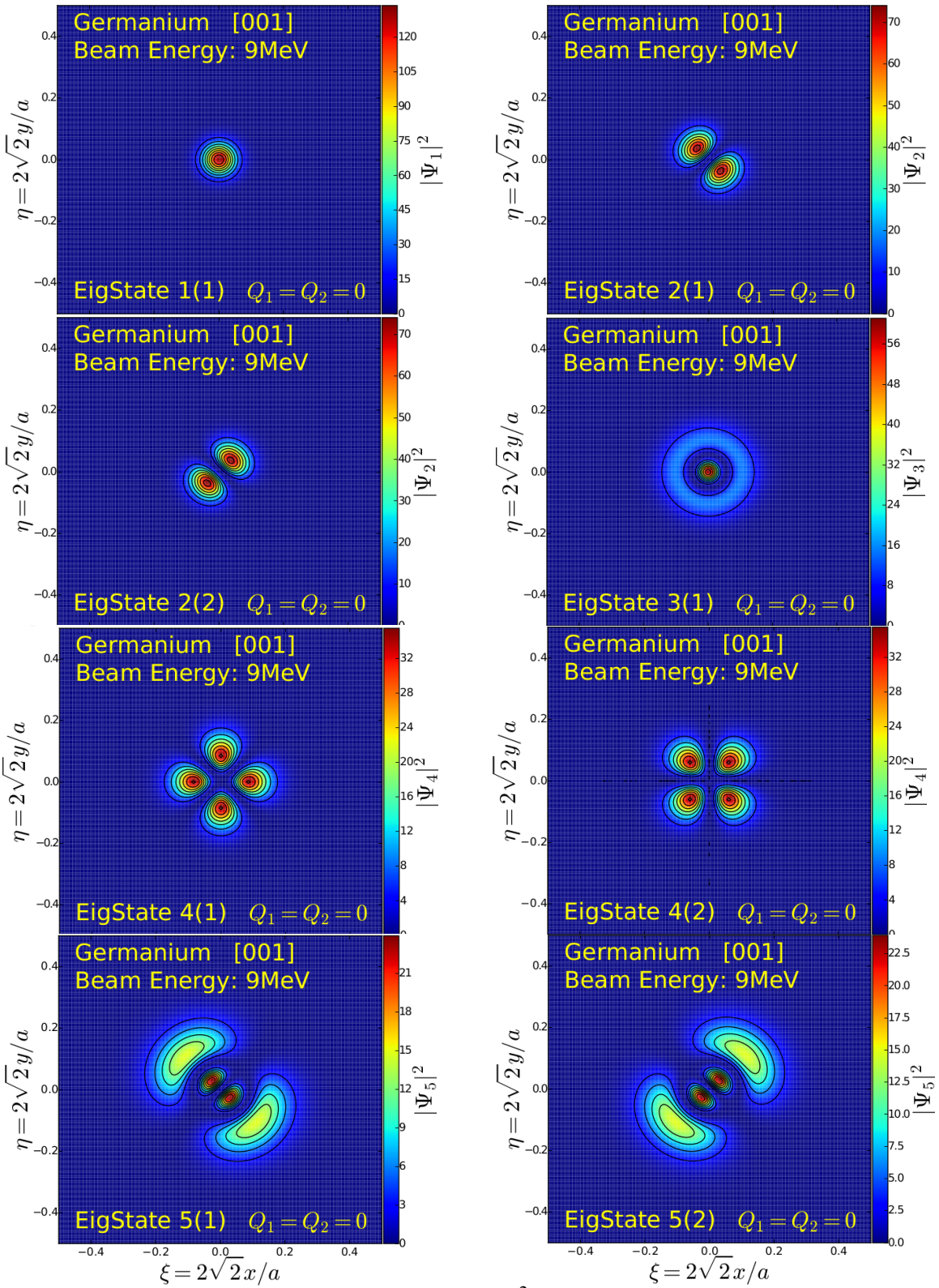

Figure 4.11: Contour plot of probability density $|\Psi_n|^2 = \langle \Psi_n | \Psi_n \rangle$ of the Bloch eigenfunctions at $Q_1 = Q_2 = 0$ for the channeling of germanium with a 9 MeV beam along [001] crystal direction, where $n(i)$ labels all the degenerate states (i) sequentially for eigenstate "n". All the states plotted are the bounded states and $n = 1$ is of the ground state.

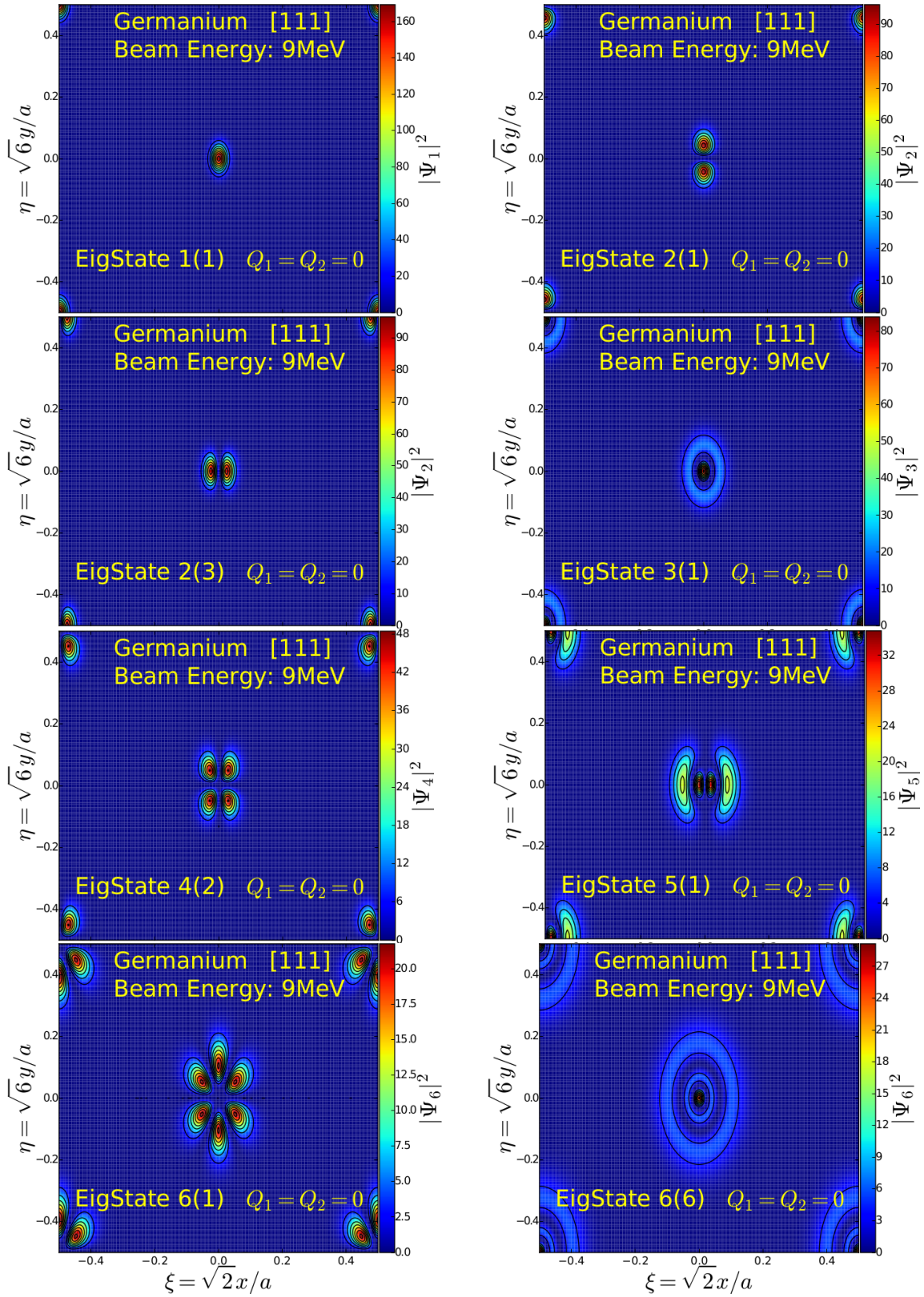

Figure 4.12: Same as Fig. 4.11 but for channeling along [111] crystal direction. The cases of $1(2)$, $2(2)$, $2(4)$, and $3(2)$ are similar to the cases of $1(1)$, $2(1)$, $2(3)$, and $3(1)$, respectively. For eigenstate $n \geq 4$, only a few examples are plotted.

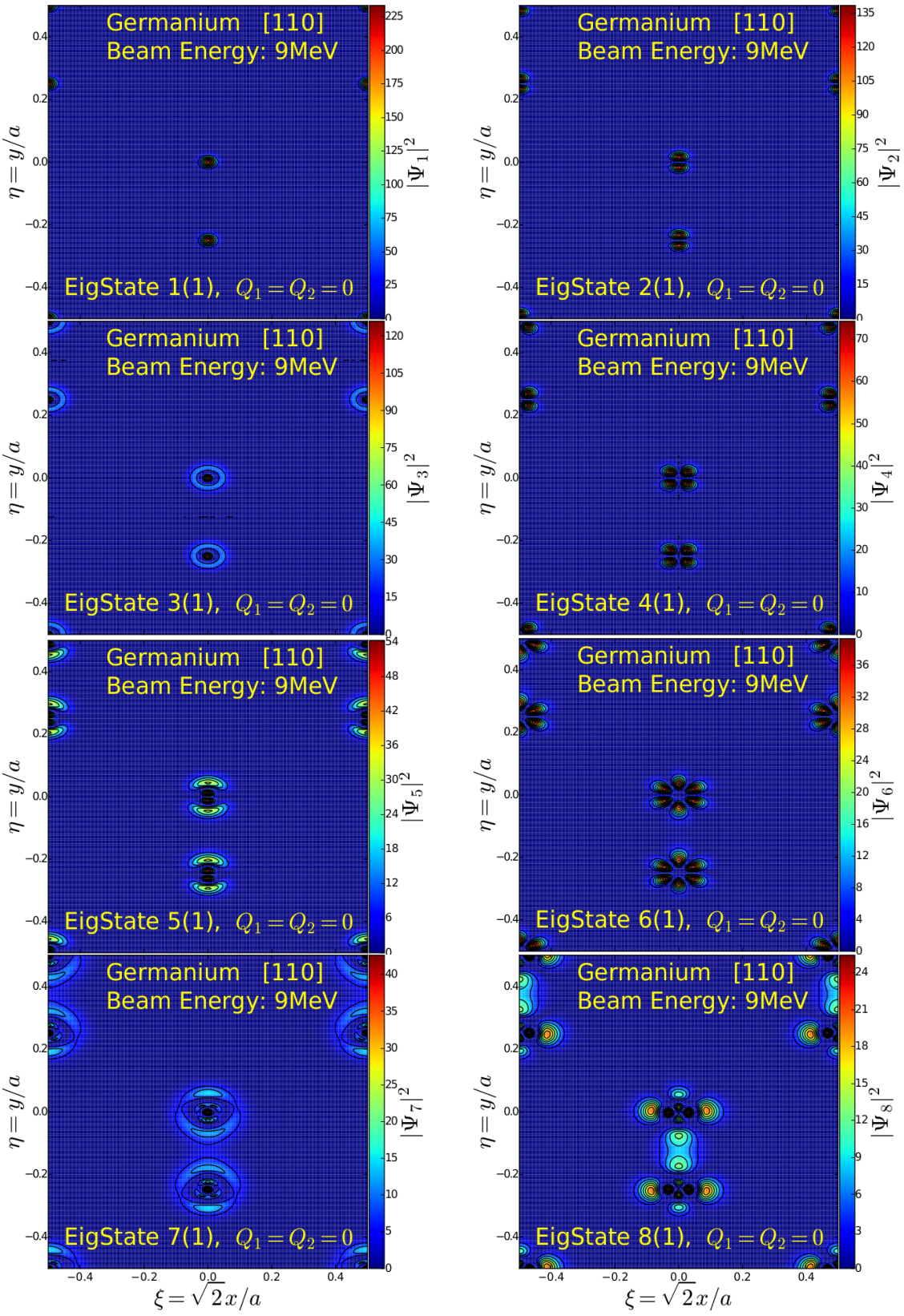

Figure 4.13: Same as Fig. 4.11 but for channeling along [110] crystal direction, where only an example for each eigenstate "*n*" are plotted.

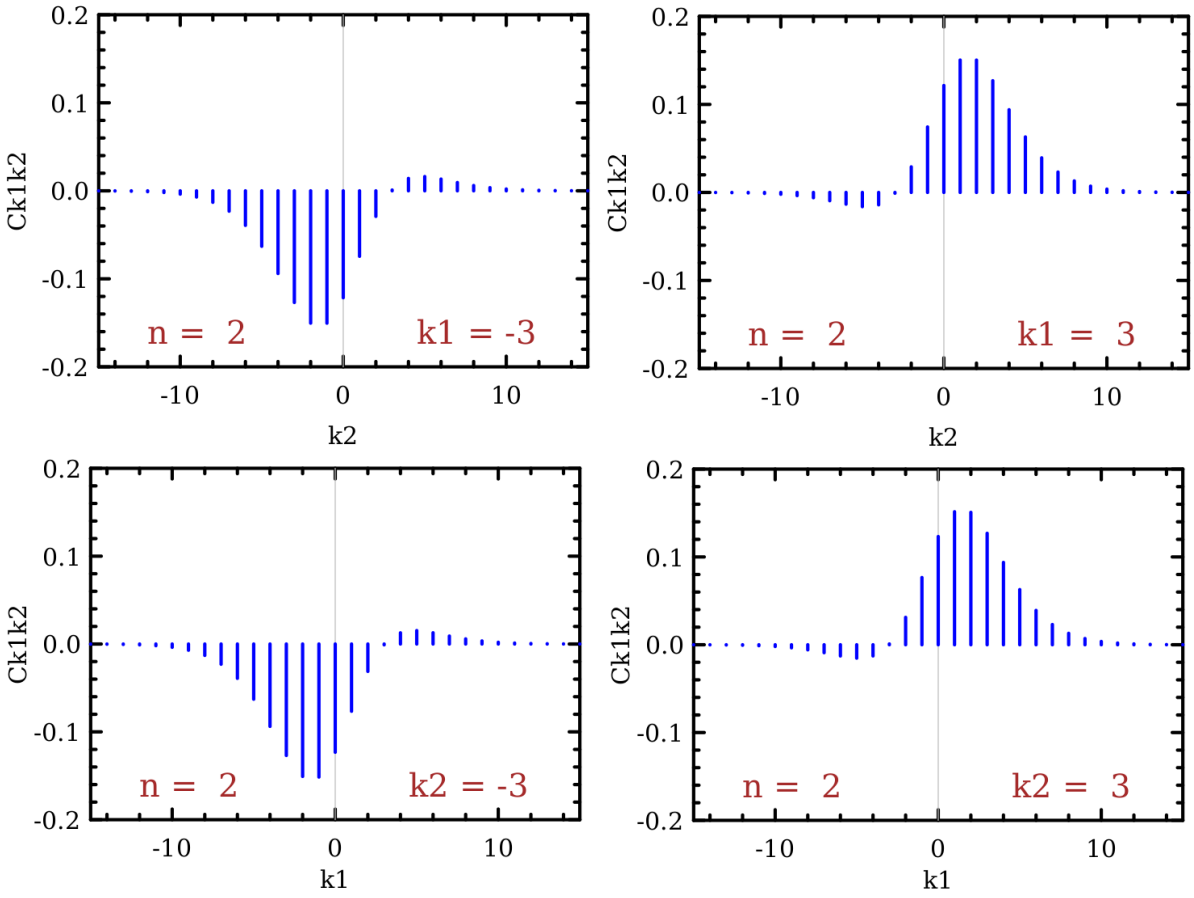

Figure 4.14: C_{k_1,k_2} for Bloch eigenstate $u_{2(2)}$ of the case in Fig. 4.11 with $n = 2$ *v.s.* k_2 at $k_1 = -3$ (top-left figure) and $k_1 = 3$ (top-right figure) and *v.s.* k_1 at $k_2 = -3$ (bottom-left figure) and $k_2 = 3$ (bottom-right figure), respectively, which suggests $C_{-k_1,-k_2} = -C_{k_1,k_2}$ or $u_{2(2)}(-x,-y) = -u_{2(2)}(x,y)$ for the channeling in the [001] crystal direction of germanium. In this case, C_{k_1,k_2} is real.

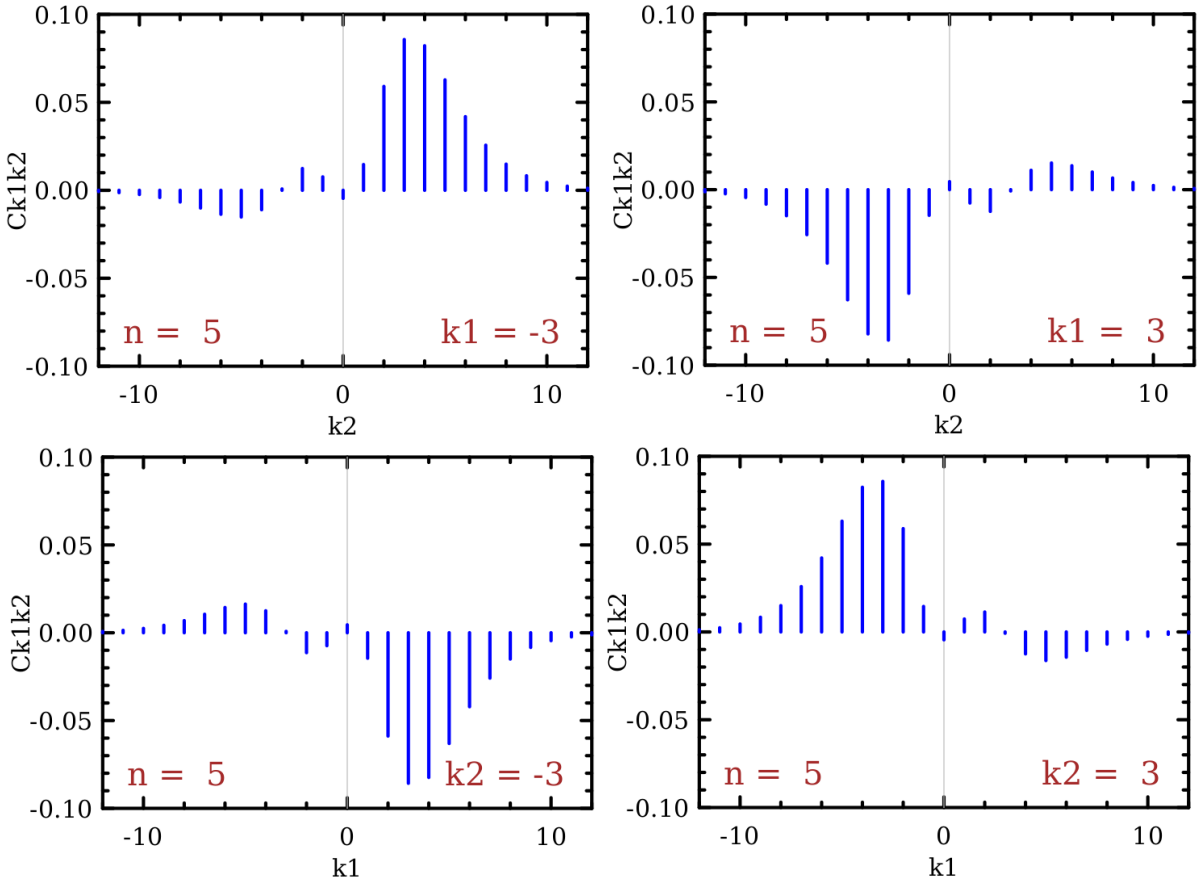

Figure 4.15: C_{k_1,k_2} for Bloch eigenstate $u_{5(1)}$ of the case in Fig. 4.11 with $n = 5$ *v.s.* k_2 at $k_1 = -3$ (top-left figure) and $k_1 = 3$ (top-right figure) and *v.s.* k_1 at $k_2 = -3$ (bottom-left figure) and $k_2 = 3$ (bottom-right figure), respectively, which suggests $C_{-k_1,-k_2} = -C_{k_1,k_2}$ or $u_{5(1)}(-x,-y) = -u_{5(1)}(x,y)$ for the channeling in the [001] crystal direction of germanium. In this case, C_{k_1,k_2} is real.

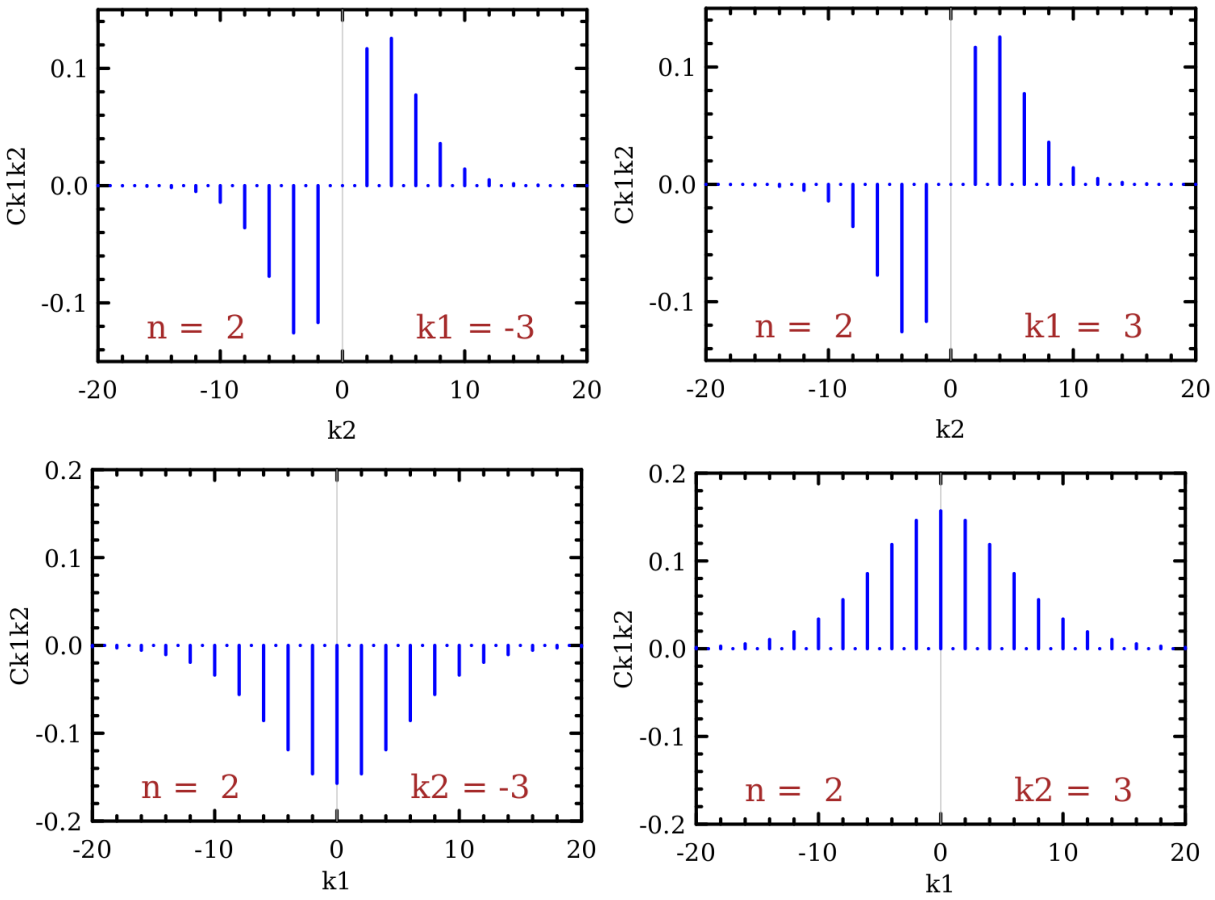

Figure 4.16: C_{k_1,k_2} for Bloch eigenstate $u_{2(1)}$ of the case in Fig. 4.12 with $n = 2$ *v.s.* k_2 at $k_1 = -3$ (top-left figure) and $k_1 = 3$ (top-right figure) and *v.s.* k_1 at $k_2 = -3$ (bottom-left figure) and $k_2 = 3$ (bottom-right figure), respectively, which suggests $C_{-k_1,k_2} = C_{k_1,k_2}$ and $C_{k_1,-k_2} = -C_{k_1,k_2}$ or $u_{2(1)}(-x,y) = u_{2(1)}(x,y)$ and $u_{2(1)}(x,-y) = -u_{2(1)}(x,y)$ for the channeling in the [111] crystal direction of germanium. In this case, C_{k_1,k_2} is real.

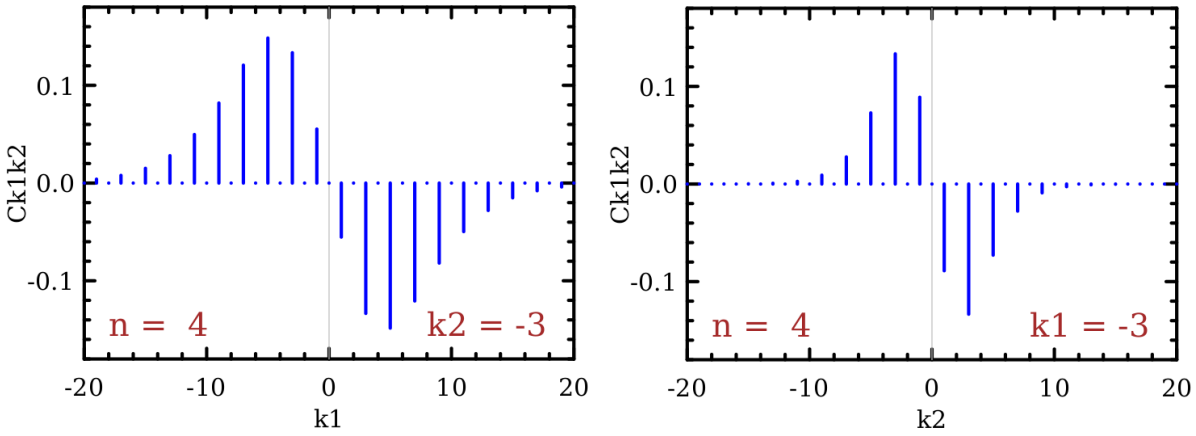

Figure 4.17: C_{k_1,k_2} for Bloch eigenstate $u_{4(1)}$ of the case in Fig. 4.12 with $n = 4$ *v.s.* k_1 at $k_2 = -3$ (left figure) and *v.s.* k_2 at $k_1 = -3$ (right figure), which suggests $u_{4(1)}(-x,y) = -u_{4(1)}(x,y)$ and $u_{4(1)}(x,-y) = -u_{4(1)}(x,y)$ for the channeling in the [111] crystal direction of germanium. In this case, C_{k_1,k_2} is real.

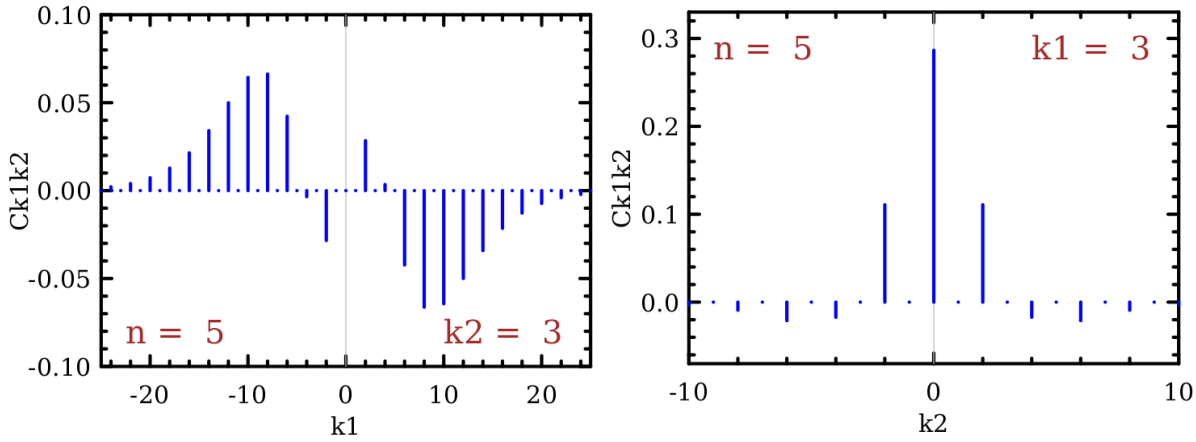

Figure 4.18: C_{k_1,k_2} for Bloch eigenstate $u_{5(1)}$ of the case in Fig. 4.12 with $n = 5$ *v.s.* k_1 at $k_2 = 3$ (left figure) and *v.s.* k_2 at $k_1 = 3$ (right figure), which suggests $u_{5(1)}(-x,y) = -u_{5(1)}(x,y)$ and $u_{5(1)}(x,-y) = u_{5(1)}(x,y)$ for the channeling in the [111] crystal direction of germanium. In this case, C_{k_1,k_2} is real.

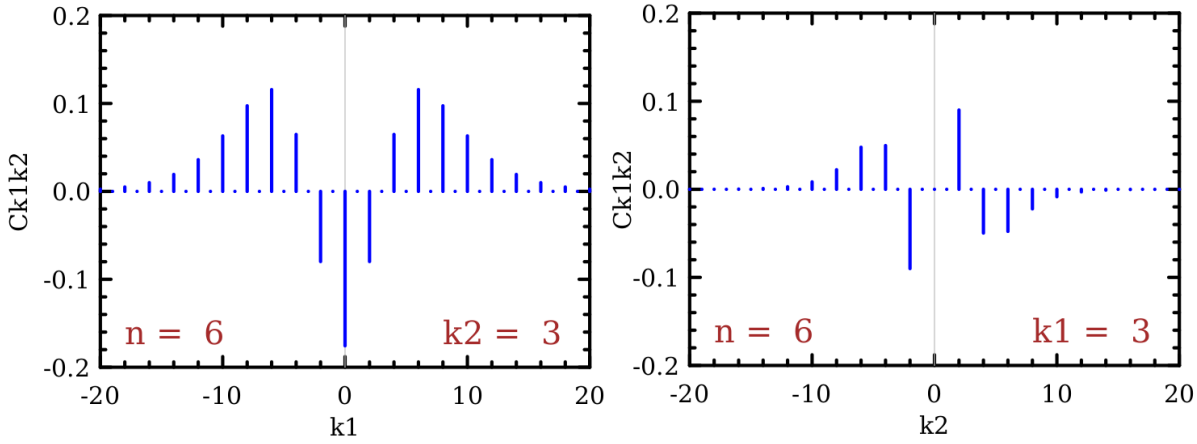

Figure 4.19: C_{k_1,k_2} for Bloch eigenstate $u_{6(1)}$ of the case in Fig. 4.12 with $n = 6$ *v.s.* k_1 at $k_2 = 3$ (left figure) and *v.s.* k_2 at $k_1 = 3$ (right figure), which suggests $u_{6(1)}(-x,y) = u_{6(1)}(x,y)$ and $u_{6(1)}(x,-y) = -u_{6(1)}(x,y)$ for the channeling in the [111] crystal direction of germanium. In this case, C_{k_1,k_2} is real.

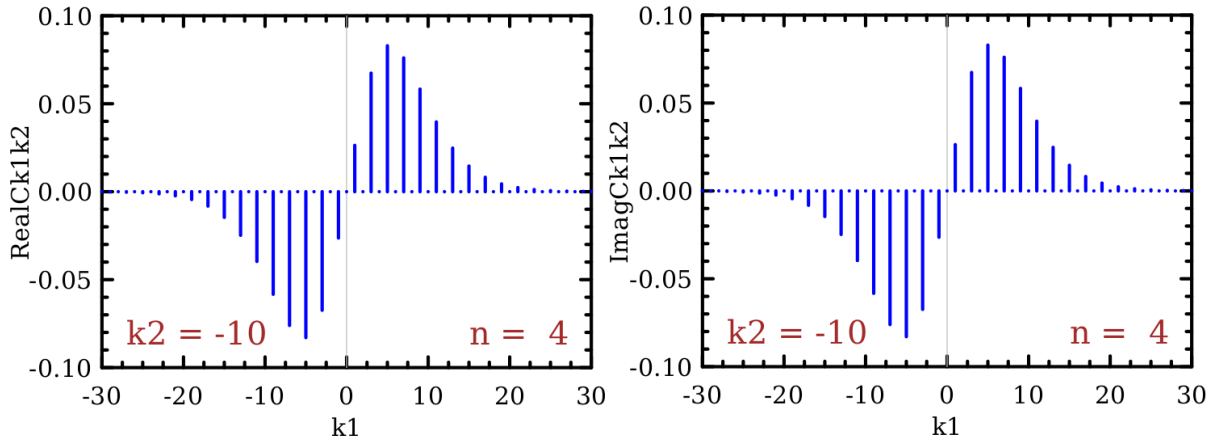

Figure 4.20: C_{k_1,k_2} for the complex Bloch eigenstate $u_{4(1)}$ of the case in Fig. 4.13 with $n = 4$ *v.s.* k_1 at $k_2 = -10$, the left and right figure are for the real and imaginary parts of C_{k_1,k_2}, respectively, which suggests $u_{4(1)}(x,-y) = -u_{4(1)}(x,y)$ for the channeling in the [110] crystal direction of germanium.

4.2 Transition Probability for Channeling Radiation

In this section, we will study the transition probability of beam electrons between two eigenstates for the transverse motion of the electrons when the beam is channeling through a crystal. This transition probability has been studied before by Andersen, Chouffani, and Klein [1, 3, 2] using a rotational symmetry approximation of the eigenstates in the axial channeling model. As it has been shown in Section 4.1.3.3, the Bloch eigenstates for the transverse motion of the beam electrons

doesn't have a rotational symmetry even approximately and the transition probability calculated with the assumption of the rotational symmetry is not applicable to the cases we consider and our result is, therefore, not consistent with the result from the previous axial channeling model [1, 3, 2].

4.2.1 Perturbation Hamiltonian

Consider a weak time-dependent perturbation of an electromagnetic (EM) field, in the beam rest frame, the Hamiltonian for a beam electron in a crystal lattice is

$$\begin{aligned} H(\vec{r},t) &= \frac{(\vec{p}-e\vec{A}/c)^2}{2m_e} + \gamma V(\vec{r}) + e\Phi \\ &\approx \frac{\vec{p}^{\,2}}{2m_e} + \gamma V(\vec{r}) - \frac{e}{2m_e c}\vec{A}\cdot\vec{p} + e\Phi \end{aligned} \tag{4.27}$$

where the unperturbed Hamiltonian is

$$H_0(x,y) = \frac{\vec{p}^{\,2}}{2m_e} + \gamma V(\vec{r})$$

with $V(\vec{r})$ being the lattice potential, $(\Phi(t),\vec{A}(t))$ is the 4-vector potential for the perturbative EM field, and

$$H_1(x,y,t) = -\frac{e}{2m_e c}\vec{A}\cdot\vec{p} + e\Phi$$

is the perturbation. When an electron beam channels through a crystal, it produces both Bremsstrahlung and channeling radiation. The Bremsstrahlung with a wide range of frequencies would be sufficient for generating a perturbative EM field. With the Coulumb gauge of EM wave without free charges, the perturbative EM field can be written as

$$\Phi = 0 \qquad \text{and} \qquad \vec{A} = \vec{A}_0 e^{-i(\omega_p t - \vec{k}\cdot\vec{r})}$$

where ω_p and $\vec{k}$ are the frequency and wave vector of the EM wave, respectively. Note that the perturbative EM wave is the same EM wave produced from the electron transition between differ-

ent energy eigenstates. With the maximum transition of 100 eV in the rest frame, the wave length of $\vec{A}$ is roughly 2×10^{-6} m and is much larger than the characteristic length scale of the problem, the lattice constant of the crystal Å which is in a scale of 10^{-10} m. The $\vec{r}$-dependence of $\vec{A}$ can therefore be neglected, which is called the electric dipole approximation [18]. Considering the electron motion on the beam transverse (x-y) plane and assuming $A_{0x} = A_{0y} = A_0$, the t-dependent perturbative Hamiltonian can thus be written as

$$H_1(x,y,t) = \left(\frac{e\hbar A_0}{2m_e c}\right)\cos(\omega_p t)\,\hat{H}_1'$$

where

$$\hat{H}_1' = -i\left(\frac{\partial}{\partial x} + \frac{\partial}{\partial y}\right) = -i\left(\frac{1}{a_x}\frac{\partial}{\partial \xi} + \frac{1}{a_y}\frac{\partial}{\partial \eta}\right) \tag{4.28}$$

4.2.2 Transition Probability

For the Bloch eigenstates

$$\left|\vec{Q},n\right\rangle = \Psi_{n,\vec{Q}}(\xi,\eta) = \frac{1}{2\pi}u_{n,\vec{Q}}(\xi,\eta)\,e^{i2\pi(Q_1\xi+Q_2\eta)}$$

the transition probability for an electron jumping from an initial state of $(n,\vec{Q})$ to a final state of $(m,\vec{Q}')$ due to the perturbation of H_1 is calculated from $\left\langle \vec{Q}',m\right| H_1 \left|\vec{Q},n\right\rangle$. Since the constant coefficient $eA_0\hbar/(2m_e c)$ in H_1 only scales the probability overall, we can disregard it in the discussion and the transition probability matrix can then be calculated from

$$\left\langle \vec{Q}',m\right| \hat{H}_1' \left|\vec{Q},n\right\rangle = \int_{-\infty}^{\infty} \Psi^*_{m,\vec{Q}'}\,\hat{H}_1'\,\Psi_{n,\vec{Q}}\,d\xi\,d\eta \tag{4.29}$$

where

$$\begin{aligned}\hat{H}_1'\Psi_{n,\vec{Q}} &= \frac{-i}{2\pi}\left(\frac{1}{a_x}\frac{\partial}{\partial\xi}+\frac{1}{a_y}\frac{\partial}{\partial\eta}\right)u_{n,\vec{Q}}(\xi,\eta)\,e^{i2\pi(Q_1\xi+Q_2\eta)} \\ &= \frac{-i}{2\pi}e^{i2\pi(Q_1\xi+Q_2\eta)}\left(\frac{1}{a_x}\frac{\partial}{\partial\xi}+\frac{1}{a_y}\frac{\partial}{\partial\eta}\right)u_{n,\vec{Q}}+2\pi\left(\frac{Q_1}{a_x}+\frac{Q_2}{a_y}\right)\Psi_{n,\vec{Q}}\end{aligned}$$

Since the second term in $\hat{H}_1'\Psi_{n,\vec{Q}}$ vanishes in Eq. (4.29) because of the orthogonal condition between $\Psi_{n,\vec{Q}}$ and $\Psi_{m,\vec{Q}'}$ with $m\neq n$, Eq. (4.29) becomes

$$\begin{aligned}&\left\langle \vec{Q}',m\middle|\hat{H}_1'\middle|\vec{Q},n\right\rangle \\ &\quad=\frac{-i}{(2\pi)^2}\int_{-\infty}^{\infty}e^{i2\pi[(Q_1-Q_1')\xi+(Q_2-Q_2')\eta]}u^*_{m,\vec{Q}'}\left(\frac{1}{a_x}\frac{\partial u_{n,\vec{Q}}}{\partial\xi}+\frac{1}{a_y}\frac{\partial u_{n,\vec{Q}}}{\partial\eta}\right)d\xi\,d\eta \qquad (4.30)\end{aligned}$$

With $u_{n,\vec{Q}}$ solved in a Fourier expansion,

$$u_{n,\vec{Q}}=\sum_{k_1,k_2=-kmax}^{kmax}C_{k_1k_2}(\vec{Q},n)\,e^{i2\pi(k_1\xi+k_2\eta)}$$

the integrals in Eq. (4.30) are simply

$$\begin{aligned}&\frac{1}{(2\pi)^2}\int_{-\infty}^{\infty}e^{i2\pi[(Q_1-Q_1')\xi+(Q_2-Q_2')\eta]}\,e^{i2\pi[(k_1-l_1]\xi+(k_2-l_2)\eta]}\,d\xi\,d\eta \\ &\qquad=\delta_{k_1l_1}\delta_{k_2l_2}\delta(Q_1-Q_1')\delta(Q_2-Q_2') \qquad (4.31)\end{aligned}$$

where (l_1,l_2) are the Fourier expansion indices for $u^*_{m,\vec{Q}'}$ and the separation of the delta functions for (k_1,k_2,l_1,l_2) and (Q_1,Q_2,Q_1',Q_2') is because (k_1,k_2,l_1,l_2) are integers while (Q_1,Q_2,Q_1',Q_2') are fractions. The transition probability matrix can therefore be written as

$$\left|\left\langle \vec{Q}',m\middle|\hat{H}_1'\middle|\vec{Q},n\right\rangle\right|^2=\mathscr{T}(n,m,\vec{Q})\,\delta(\vec{Q}-\vec{Q}') \qquad (4.32)$$

where with Eqs. (4.30) and (4.31)

$$\begin{aligned}\mathscr{T}(n,m,\vec{Q}) &= \left|\frac{1}{(2\pi)^2}\int_{-\infty}^{\infty} u^*_{m,\vec{Q}}\left(\frac{1}{a_x}\frac{\partial u_{n,\vec{Q}}}{\partial \xi}+\frac{1}{a_y}\frac{\partial u_{n,\vec{Q}}}{\partial \eta}\right)d\xi d\eta\right|^2 \\ &= \left|\sum_{k_1,k_2=-k_{max}}^{k_{max}} C_{k_1,k_2}(\vec{Q},n)C^*_{k_1,k_2}(\vec{Q},m)\left(\frac{k_1}{a_x}+\frac{k_2}{a_y}\right)\right|^2 \end{aligned} \tag{4.33}$$

If the Bloch eigenfunctions of the initial state u_n and final state u_m have the same parity in both x and y direction, $\mathscr{T}(n,m,\vec{Q})=0$ from Eq. (4.33) and the transition between those two states is forbidden. A transition is only allowed between two eigenstates that have opposite parity in either x or y direction. Tables 4.6 and 4.7 list the allowed transitions between the first six eigenenergy states with all the degenerate eigenstates at $Q_1=Q_2=0$ for the channeling of germanium with a 9 MeV electron beam along [001] and [111] crystal direction, respectively. All the allowed transitions listed in Tables 4.6 and 4.7 are consistent with the selection rule based on the parity of the Bloch eigenstates listed in Table 4.5. In the case of channeling in the [110] direction, because the parity exists only in the x direction and no other apparent symmetry exists in the y direction for the lattice potential in a unit cell on the transverse plane, there is no true forbidden transition systematically between the initial and final state even through a few of the transitions dominate probably because of larger overlap of their eigenfunctions. For the total transition probability between two different energy eigenstates disregard the difference of the degenerate states, we define

$$T(E_n,E_m,\vec{Q}) = \sum_{\left\{\begin{array}{c}\text{degenerate states}\\ \text{of } n \text{ and } m\end{array}\right\}} \mathscr{T}(n,m,\vec{Q}) \tag{4.34}$$

where the summation is over all the pairs of degenerate states between eigenenergy E_n and E_m. Figure 4.21 shows the values of $T(E_n,E_m,\vec{Q})$ at $Q_1=Q_2=0$ calculated from Eq. (4.33) with the Block eigenfunctions obtained numerically from Eq. (4.17) for a 9 MeV electron beam channeling through germanium along [001], [111], and [110] crystal direction, respectively. The result is

consistent with the selection rule based on the parity of the Bloch eigenstates listed in Table 4.5 for the case of the [001] and [111] direction. In the cases of channeling in the [110] direction, the result confirms that there is no any systematical forbidden transition between any pair of energy eigenstates.

For the radiation spectrum observed in the lab frame, the emitted photon energy ΔE for an electron transition from eigenstate $E_n(\vec{Q})$ to eigenstate $E_m(\vec{Q})$ is

$$\Delta E = \frac{E_n - E_m}{\gamma(1-\beta\cos\theta)} \tag{4.35}$$

where the factor $\gamma(1-\beta\cos\theta)$ is from the relativistic doppler effect and θ is the angle between the beam traveling direction and the line from the beam to the observation point. For $\theta = 0$ and $\beta \simeq 1$, $(1-\beta\cos\theta)^{-1} \simeq 2\gamma^2$ and $\Delta E \simeq 2\gamma(E_n - E_m)$. In the forward radiation cone of $\theta \simeq 0$, therefore, the radiation energy is boosted relativistically by a factor of 2γ to its maximum value in terms of angular dependence of the radiation energy. For the channeling radiation spectrum, one should count all the probabilities of transitions between bounded Bloch eigenstates with $0 \leq Q_1 < 1/2$ and $0 \leq Q_2 < 1/2$ that yield the same radiation energy of $\Delta E = 2\gamma(E_n - E_m)$ for the forward radiation. The total transition probability for the forward radiation energy ΔE in the lab frame is thus

$$T_p(\Delta E) = \sum_{\left\{\begin{array}{c}\text{All } n,m,\vec{Q} \text{ with} \\ 2\gamma(E_n - E_m) = \Delta E \pm \delta\end{array}\right\}} T(E_n, E_m, \vec{Q}) \tag{4.36}$$

where 2δ is the width of the energy bins in which all the possible transitions with $2\gamma(E_n - E_m) = \Delta E \pm \delta$ are counted for the same radiation energy ΔE. Note that $T_p(\Delta E)$ is the channeling radiation spectrum when the occupation number of beam electrons on the Bloch eigenstates is uniform.

Table 4.6: Allowed transitions between the first six eigenenergy states with all the degenerate eigenstates at $Q_1 = Q_2 = 0$ for the channeling of germanium with a 9 MeV electron beam along [001] crystal direction, where n and m with bolded numbers are of the initial and final state, respectively, and the numbers in parenthesis is the sequential numbering for all the degenerate eigenstates. For example, the 1st excited state ($m = 2$) has two degenerate states that are labeled with number 2(1) and 2(2), respectively, and $4(2) \rightarrow 2(2)$ means an allowed transition from one of $n = 4$ eigenstate to one of $n = 2$ eigenstates.

n \ m	**1** (1)	**2** (1,2)	**3** (1)	**4** (1,2)	**5** (1,2)
6 (1)	none	$6(1) \rightarrow 2(2)$	none	none	$6(1) \rightarrow 5(2)$
5 (1,2)	$5(2) \rightarrow 1(1)$	none	$5(2) \rightarrow 3(1)$	$5(1) \rightarrow 4(1)$ $5(2) \rightarrow 4(2)$	
4 (1,2)	none	$4(1) \rightarrow 2(1)$ $4(2) \rightarrow 2(2)$	none		
3 (1)	none	$3(1) \rightarrow 2(2)$			
2 (1,2)	$2(2) \rightarrow 1(1)$				

Table 4.7: Same as Table 4.6 but for the channeling along [111] crystal direction.

m / n	**1** (1,2)	**2** (1,2,3,4)	**3** (1,2)	**4** (1,2,3,4)	**5** (1,2,3,4)
6 (1,2 3,4 5,6)	none	$6(5) \rightarrow 2(2)$ $6(5) \rightarrow 2(4)$ $6(6) \rightarrow 2(1)$ $6(6) \rightarrow 2(3)$	none	$6(1) \rightarrow 4(2), 6(1) \rightarrow 4(4)$ $6(2) \rightarrow 4(1), 6(2) \rightarrow 4(3)$ $6(3) \rightarrow 4(1), 6(3) \rightarrow 4(3)$ $6(4) \rightarrow 4(2), 6(4) \rightarrow 4(4)$	$6(5) \rightarrow 5(3)$ $6(5) \rightarrow 5(4)$ $6(6) \rightarrow 5(1)$ $6(6) \rightarrow 5(2)$
5 (1,2 3,4)	$5(1) \rightarrow 1(2)$ $5(2) \rightarrow 1(2)$ $5(3) \rightarrow 1(1)$ $5(4) \rightarrow 1(1)$	none	$5(1) \rightarrow 3(2)$ $5(2) \rightarrow 3(2)$ $5(3) \rightarrow 3(1)$ $5(4) \rightarrow 3(1)$	$5(1) \rightarrow 4(2), 5(1) \rightarrow 4(4)$ $5(2) \rightarrow 4(2), 5(2) \rightarrow 4(4)$ $5(3) \rightarrow 4(1), 5(3) \rightarrow 4(3)$ $5(4) \rightarrow 4(1), 5(4) \rightarrow 4(3)$	
4 (1,2 3,4)	none	$4(1) \rightarrow 2(2), 4(3) \rightarrow 2(2)$ $4(1) \rightarrow 2(4), 4(3) \rightarrow 2(4)$ $4(2) \rightarrow 2(1), 4(4) \rightarrow 2(1)$ $4(2) \rightarrow 2(3), 4(4) \rightarrow 2(3)$	none		
3 (1,2)	none	$3(1) \rightarrow 2(2)$ $3(1) \rightarrow 2(4)$ $3(2) \rightarrow 2(1)$ $3(2) \rightarrow 2(3)$			
2 (1,2 3,4)	$2(1) \rightarrow 1(2)$ $2(2) \rightarrow 1(1)$ $2(3) \rightarrow 1(2)$ $2(4) \rightarrow 1(1)$				

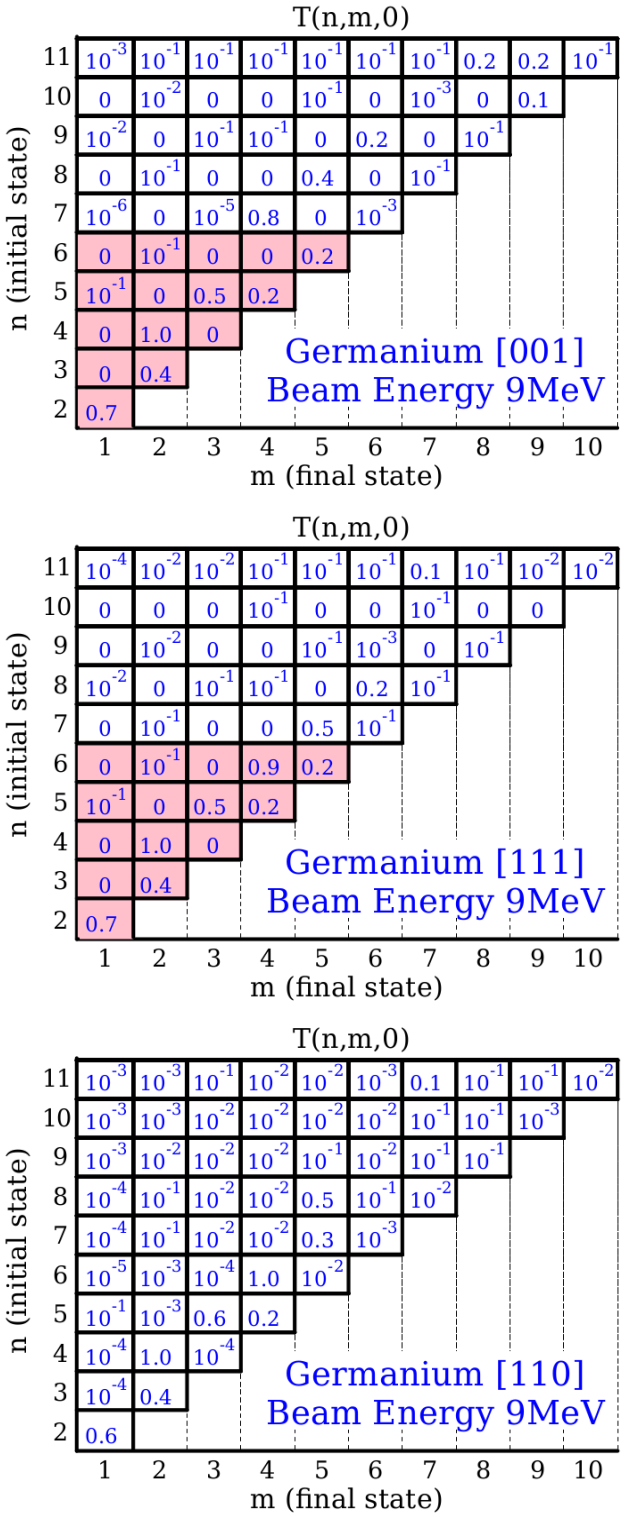

Figure 4.21: Numerically calculated $\mathscr{T}(n,m,\vec{Q})$ at $Q_1 = Q_2 = 0$ for a 9 MeV electron beam channeling through germanium along [001], [111], and [110] crystal direction, respectively, where the values of $\mathscr{T}$ are scaled in such a way that the largest value in each case is 1. Initial (n) and final (m) states are along the vertical and horizontal axis, respectively. If $\mathscr{T}$ is listed as 10^{-j}, it implies $10^{-(j+1)} < \mathscr{T} < 10^{-j}$.

4.3 Compare with Planar and Axial Channeling Model

The channeling radiation has traditionally been studied computationally using two different models with very different approximations, the one-dimensional planar [4] and two-dimensional axial channeling model [9], and the results calculated from these two models are quite different. In order to sort out the discrepancy between the planar and axial channeling model, in this study we have developed a third approach, a two-dimensional exact calculation of the channeling radiation. Note that all the three approaches are based on the same basic assumption that the channeling radiation is due to the electron transitions between bounded Bloch eigenstates for the transverse motion of beam electrons and start with the same model of single electron-ion interaction for beam electrons in a crystal. In the planar channeling model, however, the transverse motion of beam electrons is assumed to be all aligned in a single crystal direction during the channeling and approximated as a one-dimensional motion. This one-dimensional approximation is valid only if the coupling between the original two-dimensional motion of the electrons in the beam transverse plane is negligible. In the axial channeling model, on the other hand, the Bloch eigenstates for the transverse motion of beam electrons in a crystal are solved from the two-dimensional Shrödinger equation but with an approximate lattice potential on the transverse plane. In our approach, the Bloch eigenstates are solved without any approximation from the two-dimensional Shrödinger equation with an exactly calculated lattice potential. Our two-dimensional exact calculation can therefore be used as a basis for examining the validity of the approximations in the planar and axial channeling model.

a. Compare with Planar Channeling Model

To simplify the computational task of solving two-dimensional Schrödinger equation for the transverse motion of beam electrons in a crystal, the channeling radiation has been studied approximately with a one-dimensional planar channeling model [4]. In the planar channeling model, the transverse motion of beam electrons is approximated as a one-dimensional motion, which is valid

only if the coupling between the original two-dimensional motion of the electrons in the transverse plane is negligible. As shown by the two-dimensional solution of the Bloch eigenstates in Figs. 4.11, 4.12, and 4.13, however, the electron motion in the transverse plane is strongly coupled and cannot be decoupled into two independent motion (separation of variables) in two required orthogonal directions. This strong coupling in the electron motion is because the two directions of the transverse plane is coupled in the lattice potential that dominates the Schrödinger equation for the transverse motion of the electrons in the crystal. The coupling between two-dimensional transverse motion of the electrons is therefore not negligible and the one-dimensional planar channeling model is likely not appropriate for studying the channeling radiation.

In order to compared with the planar channeling model, one should first understand the beam channeling direction in the planar channeling model. In the case of (hkl) planar channeling, beam electrons are assumed to channel through a crystal along a direction that is parallel to (hkl) crystal planes while the transverse motion of the electrons is assumed to be one dimensional and perpendicular to the (hkl) plane under the influence of a periodic potential that is the average of the lattice potential on the (hkl) plane. Let x be the coordinate along $[hkl]$ crystal direction, the periodic potential for the one-dimensional transverse motion is calculated from

$$V_{(hkl)}(x) = \frac{1}{L^2}\int_0^L \int_0^L V(x,y,z)dydz \tag{4.37}$$

where $V(\vec{r})$ is the three-dimensional lattice potential of the crystal, (y,z) is a pair of orthogonal coordinates in the (hkl) plane, and L is the size of the crystal. Since for any rotational transformation of (y,z) in the (hkl) plane $(y,z) = \mathscr{R}(y_1,z_1)$,

$$V_{(hkl)}(x) = \frac{1}{L^2}\int_0^L \int_0^L V(x,y,z)dydz = \frac{1}{L^2}\int_0^L \int_0^L V(x,\mathscr{R}(y_1,z_1))dy_1dz_1$$

where $V(x,\mathscr{R}(y_1,z_1))$ is the lattice potential of the crystal in the coordinate of (x,y_1,z_1) and the determinant of Jacobian of the transformation is one. The calculation of the one-dimensional potential $V_{(hkl)}(x)$ for the planar channeling model is therefore independent of the channeling direc-

tion as long as it is parallel to the channeling plane and, for the original three-dimensional motion of the beam electrons in the crystal, the longitudinal motion and the other degree of freedom of the transverse motion can be in any two orthogonal directions in the channeling plane. In the (001) planar channeling case, for example, the one-dimensional transverse motion is along [001] crystal direction and the beam could be channeling in [100] or [110] direction, or even not aligned with any crystal direction as long as parallel to the (001) plane. The planar channeling model has been studied previously for the channeling of diamond along (100), (110) and (111) crystal plane [4]. The following table 4.8 list a few possibilities of the beam channeling direction in those planar channeling cases, where $\vec{e}_z$ is the beam channeling direction and $\vec{e}_x$ and $\vec{e}_y$ are two orthogonal directions in the beam transverse plane.

Table 4.8

$\vec{e}_x$	[100]	[001]	[110]	[110]	$[1\bar{1}0]$	[111]
$\vec{e}_y$	[010]	$[1\bar{1}0]$	$[\bar{1}10]$	[001]	$[11\bar{2}]$	$[\bar{1}\bar{1}2]$
$\vec{e}_z$	[001]	[110]	[001]	$[1\bar{1}0]$	[111]	$[1\bar{1}0]$

Note that $\vec{e}_x = [100]$ and $\vec{e}_x = [001]$ as well as $\vec{e}_x = [110]$ and $\vec{e}_x = [1\bar{1}0]$ are a pair of identical cases in the planar channeling model because of the 4-fold rotational symmetry on the (001) crystal plane of a cubic lattice. Similarly, for the three-dimensional motion of the beam electrons, the channeling direction of $\vec{e}_z = [1\bar{1}0]$ and $\vec{e}_z = [0\bar{1}1]$ are identical to $\vec{e}_z = [110]$. Therefore from table 4.9, results of the planar channeling model can be compared with our two-dimensional calculation of the channeling radiation in the following manners.

Table 4.9

Crystal Plane of 1D Planar Model	Beam Direction of 2D Calculation
(100)	[001] or [110]
(110)	[001], [110] or [111]
(111)	[110]

To compare with the results of the planar channeling model, we have therefore performed the two-dimensional calculation of the channeling radiation for a 14.6 MeV electron beam channeling along [001] and [110] crystal direction. Figure 4.22 plots the Bloch eigenenergies for the transverse motion of beam electrons obtained from our two-dimensional exact calculation as well as the eigenenergies from Azedegan's calculation based on the planar channeling model [4]. As shown in the figure, the one-dimensional approximation of the planar channeling model yields a very different set of the bounded Bloch eigenstates. In all the cases, the one-dimensional calculation yields many fewer bounded eigenenergy states than there should be and the energy gaps between bounded eigenenergy states are also very different. Therefore, the one-dimensional approximation significantly distorts the eigenstates of the transverse motion of beam electrons. In Fig. 4.23, the transition probability calculated from Eq. (4.36) with the two-dimensional exact calculation of the Bloch eigenstates is plotted as a function of photon energy and it shows a much richer transition spectrum than just a few transition lines from the one-dimensional calculation. The dense transition lines of the two-dimensional calculation is due to many nearly degenerate Bloch eigenstates especially near the maximum of the lattice potential. The major transition lines from the exact calculation is also very different from the one-dimensional approximation. The one-dimensional planar channeling model is therefore not appropriate for studying the channeling radiation. In Table 4.10, the experimentally measured radiation spectrum from Azedegan's paper [4] are compared with the possible transition lines calculated from the one-dimensional approximation as well as the two-dimensional exact calculation and it shows that the experimental data can be better explained by the two-dimensional calculation. It should be noted, however, that the calculated transition probability should not be compared with only a few measured radiation lines without the information of the distribution of beam electrons in the transverse momentum space. The radiation spectrum depends not only on the transition probability between the Bloch eigenstates but also on the electron occupation on the eigenstates which depends on the transverse momentum distribution of beam electrons.

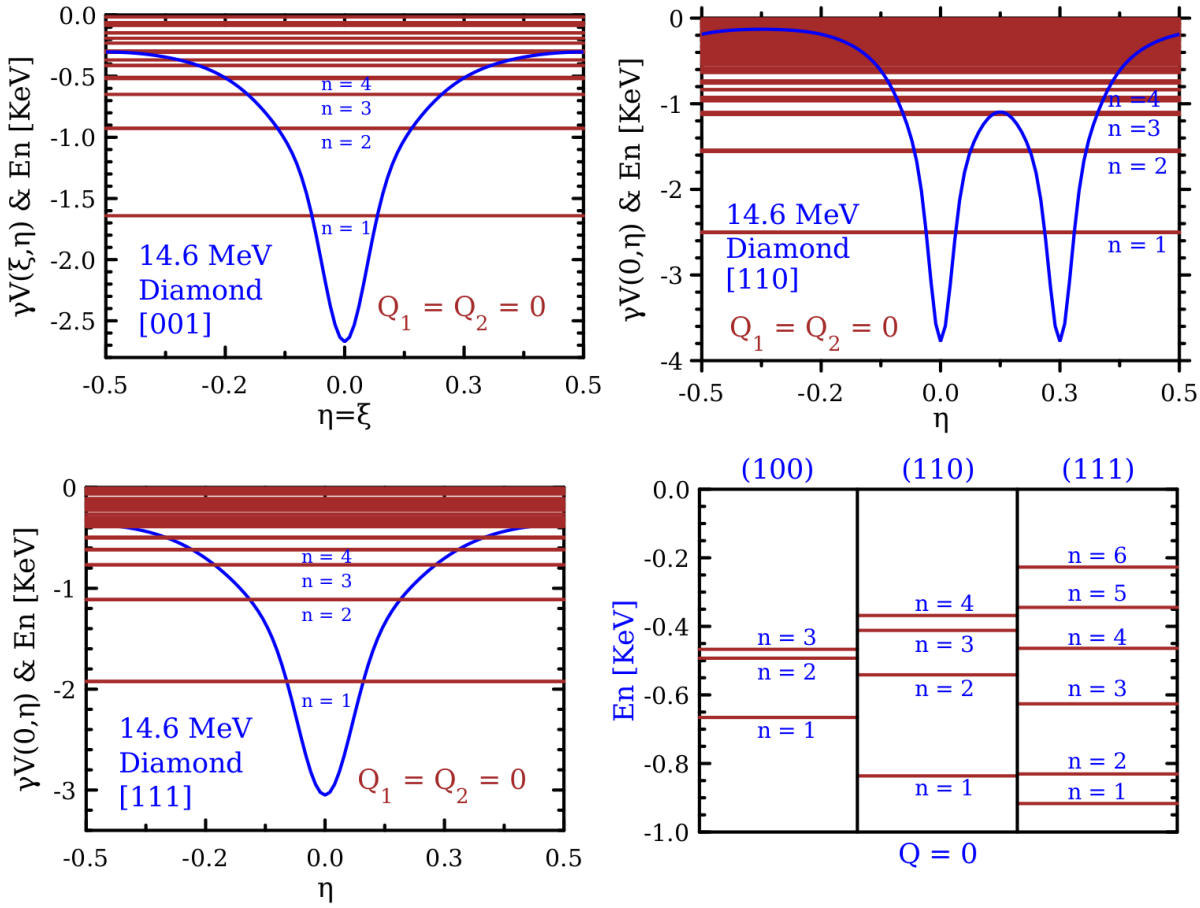

Figure 4.22: Eigenenergies (red horizontal lines) at $\vec{Q} = 0$ for the transverse motion of beam electrons in the beam rest frame for a 14.6 MeV beam channeling through diamond along [001], [110], and [111] crystal direction, respectively. Top and bottom-left figures are the results from our two-dimensional exact calculation, where the blue curve is the lattice potential $\gamma V(\xi, \eta)$ in the beam rest frame as a function of η at $\xi = \eta$ for the [001] direction and at $\xi = 0$ for the [110] and [111] direction, respectively, with $\xi = x/a_x$ and $\eta = y/a_y$. The values of a_x and a_y are given in Table 4.1. The bottom-right figure is the results of Azedegan's calculation based on the planar channeling model, where only bounded or possibly bounded states are included [4].

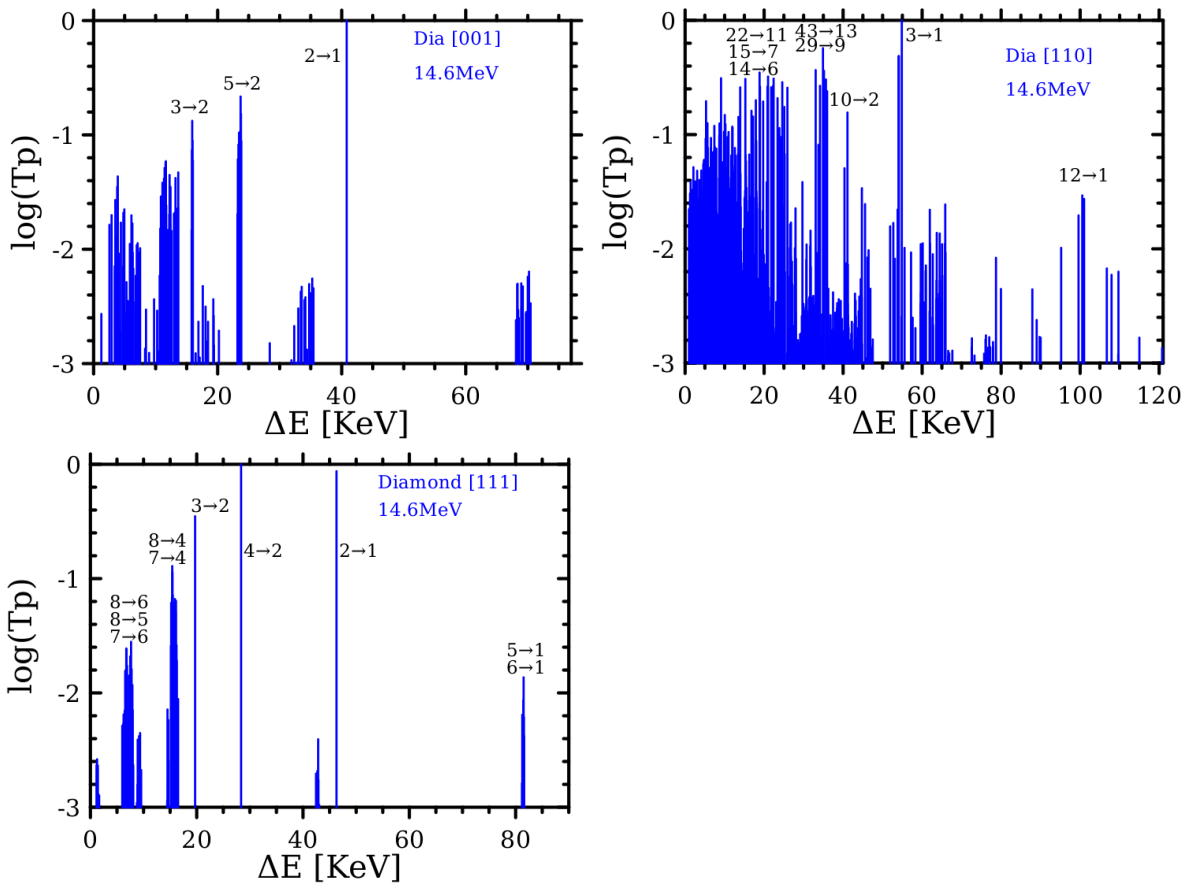

Figure 4.23: Total transition probability between bounded Bloch eigenstates with $\vec{Q} \in [0, 0.5) \otimes [0, 0.5)$ that yield radiation energy ΔE for the channeling of diamond with a 14.6 MeV beam along [001] (top-left), [110] (top-right), and [111] (bottom-left) crystal direction, respectively, where ΔE is in the lab frame and the width of the energy bin is $2\delta = 0.05$ KeV. T_p is calculated from Eq. (4.36) with the Bloch eigenstates obtained by the two-dimensional exact calculation. The label of $n \to m$ near the top of a peak marks a transition from eigenstate E_n to eigenstate E_m for that peak.

Table 4.10: Experimentally measured radiation lines from Azadegan's paper [4] in compared with the possible transition lines between the bounded Bloch eigenstates obtained with the one-dimensional (1D) approximation of the planar channeling model from Azadegan's paper [4] and from the two-dimensional (2D) exact calculation for the channeling of diamond with a 14.6 MeV beam along [001] and [110] crystal direction, respectively, where the unit of photon energy ΔE is KeV in the lab frame and $n \to m$ means a transition from E_n to E_m with E_1 being the ground state. For the 1D planar model, the crystal plane (hkl) labels the plane for motion of beam electrons during the channeling

1D planar model			measured	2D exact calculation		
Beam	Transition	ΔE	ΔE	Beam	Transition	ΔE
(100)	$2 \to 1$	9.56	9.38	[001]	$7 \to 5$	8.99 to 9.76
(110)	$2 \to 1$	17.06	16.54	[110]	$25 \to 13$	16.54
					$27 \to 14$	16.51
					$30 \to 16$	16.53
					$31 \to 18$	16.58
					$33 \to 20$	16.51
					$34 \to 21$	16.52
(110)	$3 \to 2$	7.13	7.89	[110]	$6 \to 5$	7.93
					$28 \to 21$	7.85
					$29 \to 22$	7.85
					$31 \to 24$	7.85
					$31 \to 25$	7.87
					$31 \to 26$	7.90
					$32 \to 27$	7.88
					$34 \to 28$	7.89
					$34 \to 29$	7.91
(111)	$3 \to 2$	11.69	11.07	[110]	$12 \to 8$	11.05
					$16 \to 12$	11.05
					$25 \to 15$	11.08
					$29 \to 16$	11.1
					$41 \to 20$	11.05
(111)	$4 \to 3$	9.26	8.14	[110]	$6 \to 5$	7.93
					$29 \to 19$	8.21
					$35 \to 21$	8.31
(111)	$5 \to 4$	6.83	6.05	[110]	$9 \to 7$	6.23
					$26 \to 18$	6.24
	$6 \to 5$	6.71			$29 \to 20$	6.18
					$35 \to 25$	6.05

b. Compare with Axial Channeling Model and Experimental Data

The channeling radiation spectrum has also been calculated previously using the axial channeling model and studied experimentally for the cases of diamond along [001] crystal direction with 16.9 and 30.5 MeV beam energy [2], respectively, and along the [110] direction with 5.2 and 9 MeV beam energy [5], respectively. For [111] crystal direction, only one experimental study has been done with a 4 MeV beam channeling through silicon lattice [1]. To compared with the results from the previous studies, we have calculated the total transition probability $T_p(\Delta E)$ in Eq. (4.36) between all the bounded Bloch eigenstates for those cases using our method. As shown in Figs. 4.24, 4.25, and 4.26, the transition spectrum obtained are very different from the result of the axial channeling model in terms of both broad bands and dominate peaks of the transition probability. For the cases of the [001] and [110] direction, the broad bands at lower energy of the transition spectrum are due to the transitions between many Bloch eigenstates with the eigenenergies in a nearly continuous band near the maximum of the lattice potential well. In the case of the [111] direction, because of a very low beam energy there are only very few bounded states and there is no continuous energy band in the bounded state. Therefore, the transition spectrum contains only a few peaks as shown in Fig. 4.26. From the axial channeling model, on the other hand, the transition spectrum contains only four and six possible transitions in the cases of the [001] direction with 16.9 and 30.5 MeV beam, respectively, and only three possible transitions in the case of the [110] direction with 5.2 and 9 MeV beam. It is not clear why there are only a small number of transition possibilities from the axial channeling model. It could be either because only the dominate transition peaks were discussed in their papers or due to the use of much more strict transition selection rule based on the approximation of a rotational symmetry of the system. It should be noted, as shown in Table 4.11, that both our calculation and the calculation with the axial channeling model are based on the same basic channeling radiation model, in which the radiation is assumed to be from the transitions between the Bloch eigenstates for the transverse motion of beam electrons, and the fundamental difference in the two different treatments is the additional approximations in the axial channeling model as our treatment is exact from the basic channeling

radiation model to the transition spectrum. The very different transition spectrum obtained from these two different treatments only suggests that the approximations used in the axial channeling model is not appropriate for studying the channeling radiation with the conditions that we are interested in.

For all the cases in Figs. 4.24, 4.25, and 4.26, the radiation spectrum was measured experimentally and a few radiation peaks from the measured continuous spectrum were given in their papers [1, 2, 5]. As shown in Figs. 4.24 and 4.25, the measured radiation peaks matches very well with the calculated transition spectrum using the axial channeling model while those measurements do not agree with our calculation. It is rather puzzling that the result from a more accurate calculation does not agree with the experiments while the calculation with additional approximations matches with the experiment nicely. Further experimental study with a better control of experimental conditions such as the radiation detection conditions and beam conditions (electron distribution in the transverse momentum space) is therefore needed to sort out this puzzle.

Table 4.11: Similarities and differences between our two-dimensional exact calculation and the axial and planar channeling model in the calculation of the channeling radiation.

	2D exact calculation	**Axial Channeling Model**	**Planar Channeling Model**
basic assumption	Channeling radiation is due to electron transitions between Bloch eigenstates for the transverse motion of beam electrons.		
single electron-ion interaction	Born approximation for scattering with fitting parameters from experimental data. All three methods can also use other interaction models.		
lattice potential in beam transverse plane	Potential is calculated without any approximation and not rotationally symmetric in the transverse plane.	Potential is calculated approximately and different from the one calculated exactly.	Potential is only calculated along one direction in the transverse plane
Bloch eigenstates	Eigenstates are calculated without any approximation and, in general, not rotationally symmetric in the transverse plane. The relative numerical errors of the calculation are under 10^{-6}.	It's not clear how they were obtained numerically and how large the numerical errors are.	Eigenstates for the 1D motion are solved from 1D Schrödinger equation
transition probability	Transition probabilities are calculated from 2D eigenstates.	Transition probabilities were discussed with the assumption of a rotational symmetry in the eigenfunctions	Transition probabilities are calculated from 1D eigenstates.
radiation spectrum	accurate 2D calculation	approximate 2D calculation	approximate due to 1D calculation

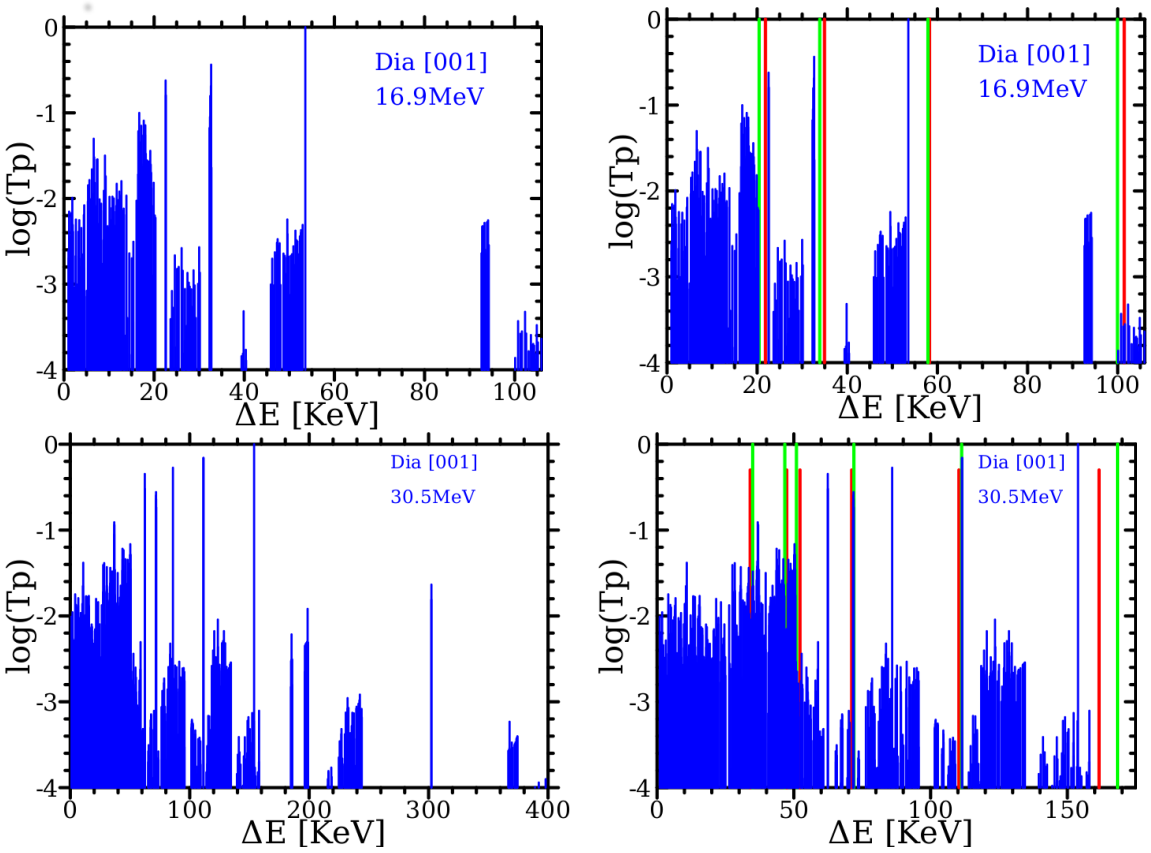

Figure 4.24: Total probability of the transitions between bounded Bloch eigenstates with $\vec{Q} \in [0,0.5) \otimes [0,0.5)$ that yield radiation energy ΔE for the channeling of diamond along [001] crystal direction with 16.9 and 30.5 MeV beam energy, respectively, where ΔE is observed in the lab frame and the width of the energy bin is $2\delta = 0.05$ KeV. Left figures are the spectrum calculated from our model with Eq. (4.36) and the right figures are the same spectrum over plotted with the result from Klein's calculation based on the axial channeling model (green lines) and Klein's experimental measurement (red lines) [2].

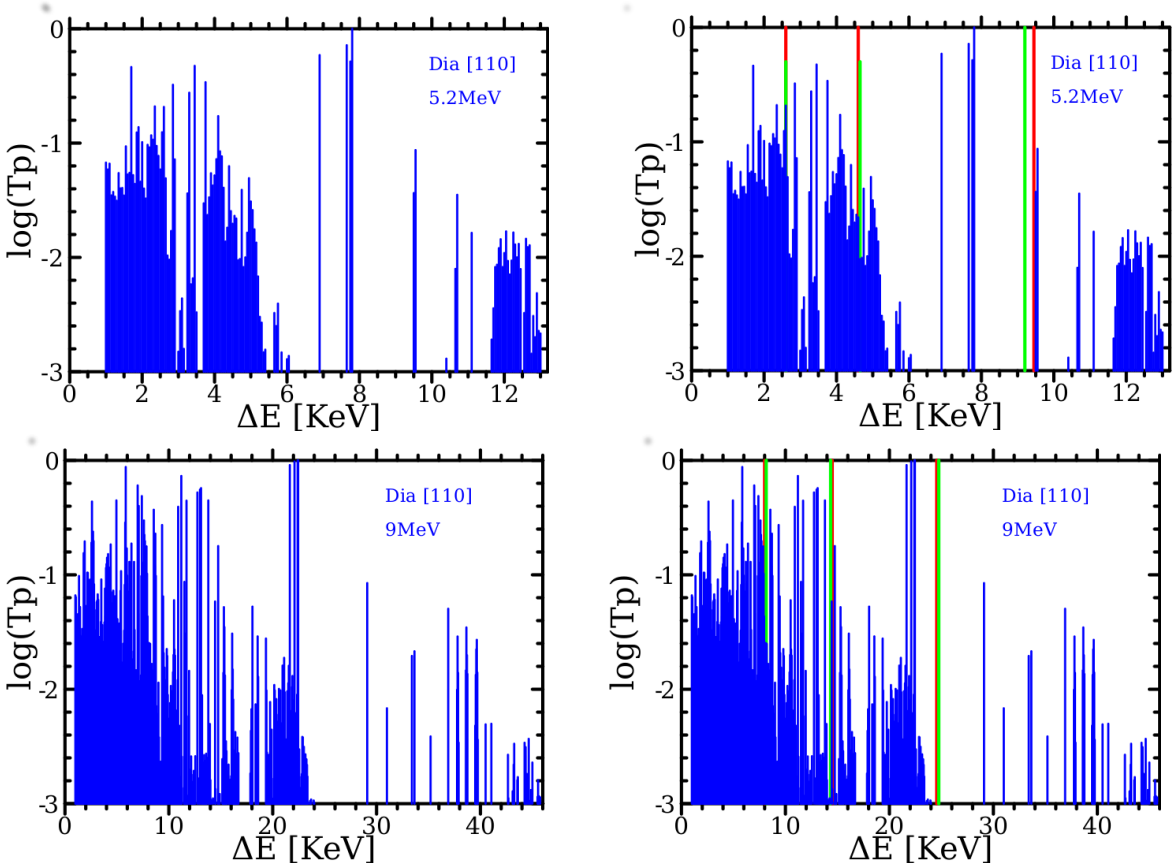

Figure 4.25: Same as Fig. 4.24 but for the channeling of diamond along [110] crystal direction with 9 and 5.2 MeV beam energy, respectively. Left figures are the spectrum calculated from our model with Eq. (4.36) and the right figures are the same spectrum over plotted with the result from Genz's calculation based on the axial channeling model (green lines) and Genz's experimental measurement (red lines) [5].

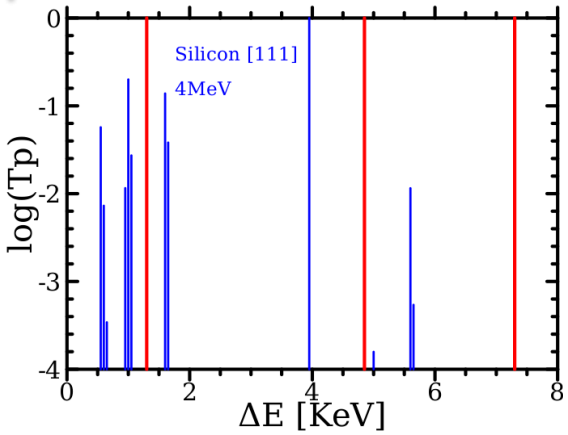

Figure 4.26: Same as Fig. 4.24 but for the channeling of Silicon along [111] crystal direction with 4 MeV beam energy, where the Blue is the spectrum calculated from our model with Eq. (4.36) and the Red is the experimental measurement from Anderson's paper [1].

Chapter 5

Beam Structures Affects on Channeling Spectrum

The observed channeling radiation spectrum is determined by the transition probabilities between the Bloch eigenstates for the transverse motion of beam electrons together with the occupation number of the beam electrons at each eigenstate. In this chapter, we will study the electron occupation number that is determined by the distribution of the beam electrons in the transverse momentum space. Prior to entering the crystal lattice, the beam electrons move non-relativistically as free particles in the transverse plane. Once entering the crystal, each electron has certain probabilities to occupy the Bloch eigenstates. An electron with sufficiently small (large) transverse momentum has a high probability to occupy the bounded (unbounded) Bloch eigenstates. The electrons at the bounded eigenstates are confined to a small region in the unit cell of the crystal lattice in the transverse plane when the beam passes through the crystal and, therefore, they are channeling through the crystal without experiencing any random scattering from the lattice. The electrons at the unbounded eigenstates, on the other hand, are not confined in the transverse plane and, therefore, randomly scattered by and cannot channel through the crystal. For channeling radiation, we will focus only on the beam electrons at the bounded Bloch eigenstates for their transverse motion.

5.1 Probabilities of a beam electron at Bloch eigenstates

When an ultra-relativistic beam enters a crystal lattice, the beam electrons interact with the lattice potential and occupy the Bloch eigenstates for the beam transverse motion of the electrons. Considering a beam electron moves with momentum $\vec{p} = (p_x, p_y)$ in the transverse plane in the beam rest frame before entering the crystal, the initial wavefunction of the electron is

$$\Phi_e(\vec{p}) = \frac{1}{2\pi} e^{i(p_x x + p_y y)/\hbar}$$

Inside the lattice potential in the transverse plane, the probabilities of the electron at the Bloch eigenstates can be calculated by an expansion of $\Phi_e(\vec{p})$ with the Bloch eigenstates,

$$\Phi_e(\vec{p}) = \int_0^{1/2}\int_0^{1/2} d\vec{Q} \sum_n \left\langle \Phi_e(\vec{p}) \middle| \Psi_{n,\vec{Q}} \right\rangle \Psi_{n,\vec{Q}}(x,y) \tag{5.1}$$

where

$$\Psi_{n,\vec{Q}}(x,y) = \frac{1}{2\pi} \sum_{k_2=-k_{max}}^{k_{max}} \sum_{k_1=-k_{max}}^{k_{max}} C_{k_1,k_2}(\vec{Q},n)\, e^{i2\pi[(k_1+Q_1)x/a_x + (k_2+Q_2)y/a_y]} \tag{5.2}$$

is the Bloch eigenstates in the first Brillouin zone, n numbers all the eigenenergy states including all the degenerate eigenstats, and (a_x, a_y) are the lattice constants of the primitive unit cell of the lattice in the transverse plane. Because of the symmetry of the Schrödinger equation in the Brillouin zone, we only need the first quadrant of the Brillouin zone $\vec{Q} \in [0, 0.5) \otimes [0, 0.5)$ for the expansion. The probability of the electron with transverse momentum $\vec{p}$ occupying the Bloch eigenstate $\Psi_{n,\vec{Q}}$ is

thus

$$\begin{aligned}
\left|\left\langle \Phi_e(\vec{p}) \left| \Psi_{n,\vec{Q}} \right\rangle\right|^2 &= \left| \int_{-\infty}^{\infty} \Phi_e^*(\vec{p}) \Psi_{n,\vec{Q}}(x,y)\, dxdy \right|^2 \\
&= \left| \sum_{k_1,k_2=-k_{max}}^{k_{max}} C_{k_1,k_2}(\vec{Q},n) \frac{1}{(2\pi)^2} \int_{-\infty}^{\infty} e^{i2\pi[(k_1+Q_1)/a_x - p_x/h]x} dx \int_{-\infty}^{\infty} e^{i2\pi[(k_2+Q_2)/a_y - p_y/h]y} dy \right|^2 \\
&= \left| \sum_{k_1,k_2=-k_{max}}^{k_{max}} C_{k_1,k_2}(\vec{Q},n)\, \delta\left(\frac{p_x}{h} - \frac{k_1+Q_1}{a_x}\right) \delta\left(\frac{p_y}{h} - \frac{k_2+Q_2}{a_y}\right) \right|^2 \\
&= \left| C_{k_1,k_2}(\vec{Q},n) \right|^2_{\vec{k}=\vec{P}-\vec{Q}} = \sum_{k_1=-k_{max}}^{k_{max}} \sum_{k_2=-k_{max}}^{k_{max}} \left| C_{k_1,k_2}(\vec{Q},n) \right|^2 \delta\left(\vec{k} - \vec{P} + \vec{Q}\right)
\end{aligned} \tag{5.3}$$

where $\vec{P} = (p_x a_x\,,\, p_y a_y)/h$. The delta function in Eq. (5.3) enforces the conservation of momentum when the electron interacts with the lattice potential, i.e. the wave vector $\vec{p}/h$ of an incident electron has to match a Bloch wave vector $((k_1+Q_1)/a_x\,,\,(k_2+Q_2)/a_y)$ so that the electron has a probability of $\left|C_{k_1,k_2}(\vec{Q},n)\right|^2$ to occupy the eigenstate $\Psi_{n,\vec{Q}}$.

5.2 Occupation number of beam electrons at Bloch eigenstates

Let $f(p_x, p_y)$ be the distribution of the transverse momentum of an electron beam with

$$\int_{-p_{xmax}}^{p_{xmax}} \int_{-p_{ymax}}^{p_{ymax}} f(p_x,p_y) dp_x dp_y = N\,,$$

where N is the number of electrons in the beam and p_{xmax} and p_{ymax} are the maximal possible transverse momenta of the electrons. The occupation number of the electrons at the Bloch eigenstate

$\Psi_{n,\vec{Q}}$ can then be calculated as

$$\begin{aligned}
\mathscr{N}(n,\vec{Q}) &= \int_{-p_{xmax}}^{p_{xmax}} \int_{-p_{ymax}}^{p_{ymax}} \left| \left\langle \Phi_e(\vec{p}) \middle| \Psi_{n,\vec{Q}} \right\rangle \right|^2 f(p_x,p_y)\, dp_x dp_y \\
&= \frac{h^2}{a_x a_y} \sum_{k_1=-k_{max}}^{k_{max}} \sum_{k_2=-k_{max}}^{k_{max}} \left| C_{k_1,k_2}(\vec{Q},n) \right|^2 \\
&\quad \times \int_{-P_{1max}}^{P_{1max}} \int_{-P_{2max}}^{P_{2max}} \delta\left(\vec{k}-\vec{P}+\vec{Q}\right) f\left(\frac{P_1 h}{a_x}, \frac{P_2 h}{a_y}\right) dP_1 dP_2 \\
&= \frac{h^2}{a_x a_y} \sum_{k_1=-k_{max}}^{k_{max}} \sum_{k_2=-k_{max}}^{k_{max}} \left| C_{k_1,k_2}(\vec{Q},n) \right|^2 f\left(\frac{(k_1+Q_1)h}{a_x}, \frac{(k_2+Q_2)h}{a_y}\right) \\
&\qquad \times H\left(P_{1max}-|k_1+Q_1|\right) H\left(P_{2max}-|k_2+Q_2|\right)
\end{aligned} \tag{5.4}$$

where $(P_{1max}, P_{2max}) = (p_{xmax}a_x, p_{ymax}a_y)/h$ and $H(z)$ is Heaviside step function with $H(z) = 0$ for $z < 0$ and $H(z) = 1$ for $z \geq 0$. In the definition of the beam distribution of the transverse momentum, p_{xmax} and p_{ymax} are the maximal transverse momentum of the electrons in the beam and can be controlled experimentally by designing the beam shape. If p_{xmax} and/or p_{ymax} are larger than the maximal transverse momentum (p_c) allowed for channeling, only the electrons with $p_x^2 + p_y^2 \leq p_c^2$ can channel through the crystal and need to be considered in Eq. (5.4). It is, however, not necessary to apply $p_x^2 + p_y^2 \leq p_c^2$ in Eq. (5.4) as long as only the bounded Bloch eigenstates are included for the calculation of the channeling radiation spectrum. It should also be noted that the channeling condition of $p_x^2 + p_y^2 \leq p_c^2$ is only a classical estimate of a quantum phenomenon. In quantum mechanics, an electron with $p_x^2 + p_y^2 > p_c^2$ has still possibilities, even very small, to occupy the bounded Bloch eigenstates and to be able to channel through the crystal without being scattered. The electrons with $p_x^2 + p_y^2 < p_c^2$, on the other hand, have also some probabilities to occupy unbounded Bloch eigenstates and to be unable to channel through the crystal. Nevertheless, the condition of $p_x^2 + p_y^2 \leq p_c^2$ provides an estimate on the maximal beam size p_{xmax} and p_{ymax} in the transverse momentum space that one could design a beam for a desired electron occupation profile at the bounded Bloch eigenstates and, in turn, for a desired channeling radiation spectrum

without too much Bremsstrahlung noise in the radiation due to the scattering of the dechanneled electrons. To estimate p_c, we consider the condition for an electron being trapped inside the lattice potential in the transverse plane: the energy of the transverse motion of the electron has to be smaller than the maximum of the lattice potential, *i.e.* in the beam rest frame,

$$\frac{1}{2m_e}(p_x^2+p_y^2)+\gamma V(x,y)\leq \gamma V_{max} \tag{5.5}$$

where V_{max} is the maximum of the lattice potential $V(x,y)$ and the maximal kinetic energy $p_c^2/2m_e$ occurs at the minimum (V_{min}) of $V(x,y)$. Therefore

$$\frac{1}{2m_e}(p_x^2+p_y^2)\leq \frac{1}{2m_e}p_c^2=\gamma V_{max}-\gamma V_{min}$$

and

$$p_c=\sqrt{2m_e\gamma(V_{max}-V_{min})} \tag{5.6}$$

Note that p_c defined here is equivalent to the definition of Lindhard's critical angle in Eq. (2.2).

a. Uniform distribution of transverse momentum

In the case that a beam has a uniform distribution of the electrons in the transverse momentum space,

$$f(p_x,p_y)=\begin{cases}\dfrac{N}{4p_{xmax}p_{ymax}}, & \text{for } |p_x|\leq p_{xmax} \text{ and } |p_y|\leq p_{ymax}\\ 0, & \text{otherwise}\end{cases} \tag{5.7}$$

The electron occupation numbers at the Bloch eigenstates are

$$\begin{aligned}\mathscr{N}(n,\vec{Q}) &= \frac{N}{4P_{1max}P_{2max}}\sum_{k_1=-k_{max}}^{k_{max}}\sum_{k_2=-k_{max}}^{k_{max}}\left|C_{k_1,k_2}(\vec{Q},n)\right|^2\\ &\quad\times H\left(P_{1max}-|k_1+Q_1|\right)H\left(P_{2max}-|k_2+Q_2|\right)\end{aligned} \tag{5.8}$$

b. Gaussian distribution of transverse momentum

In the case that a beam has a Gaussian distribution of the electrons in the transverse momentum space,

$$f(p_x, p_y) = \frac{N}{2\pi\sigma_x\sigma_y} e^{-\left(p_x^2/\sigma_x^2 + p_y^2/\sigma_y^2\right)/2} \tag{5.9}$$

where the beam width (σ_x, σ_y) in the transverse momentum space is determined from the emittance and Courant-Synder parameters of the beam (will be discussed later). The occupation numbers of the electron at the Bloch eigenstates are

$$\begin{aligned} \mathscr{N}(n, \vec{Q}) &= \frac{N}{2\pi\sigma_1\sigma_2} \sum_{k_1=-k_{max}}^{k_{max}} \sum_{k_1=-k_{max}}^{k_{max}} \left| C_{k_1,k_2}(\vec{Q}, n) \right|^2 e^{-\left[(k_1+Q_1)^2/\sigma_1^2 + (k_2+Q_2)^2/\sigma_2^2\right]/2} \\ &\quad \times H\left(P_{1max} - |k_1 + Q_1|\right) H\left(P_{2max} - |k_2 + Q_2|\right) \end{aligned} \tag{5.10}$$

where $(\sigma_1\,, \sigma_2) = (\sigma_x a_x\,, \sigma_y a_y)/h$. When $\sigma_x >> p_c$ and $\sigma_y >> p_c$, the electrons in the core ($|p_x| < p_c$ and $|p_y| < p_c$) of the beam that can channeling through the crystal have nearly a uniform distribution in the transverse momentum space.

5.3 Calculation of Channeling Radiation Spectrum

The channeling radiation intensity from the transitions of beam electrons from an initial Bloch eigenstate $\Psi_{n,\vec{Q}}$ to a final eigenstate $\Psi_{m,\vec{Q}'}$ is proportional to

$$\mathscr{N}(n, \vec{Q})\, \mathscr{T}(n, m, \vec{Q})\, \delta(\vec{Q}' - \vec{Q})$$

which emits photons of energy $\Delta E = E_n(\vec{Q}) - E_m(\vec{Q})$, where ΔE is the photon energy in the beam rest frame. The total radiation intensity of a given photon energy can thus be obtained by summing

over all different combinations of the initial and final states that generate the same photon energy,

$$\mathscr{I}(\Delta E) = \sum_{\left\{\begin{array}{c}\text{All bounded states}\\ \text{of } n,m,\vec{Q} \text{ with}\\ E_m - E_n = \Delta E\end{array}\right\}} \mathscr{N}(n,\vec{Q})\,\mathscr{T}(n,m,\vec{Q}) \tag{5.11}$$

where the summation includes only the bounded Bloch eigenstates. Figure 5.1 plots $\mathscr{I}(\Delta E)$ calculated for the channeling of diamond along [110] crystal direction, where the beam has a round Gaussian distribution in the transverse momentum space with $\sigma_x = \sigma_y = \sigma$, and shows how the spectrum changes with the beam width σ_x from $\sigma << p_c$ to $\sigma > p_c$. As shown in the figure 5.1, $\mathscr{N}(n,\vec{Q})$ is quite sparse when $\sigma << p_c$ and increases in density as σ increases. Consequently, the radiation spectrum becomes more rich because of more electrons in different eigenstates as σ increases. The channeling radiation spectrum can therefore be changed by shaping the beam distribution in the transverse momentum space. With a properly constructed beam distribution of the transverse momentum, we could even have only a few specific eigenstates to be occupied which allows for a tunable channeling radiation from a few select transitions.

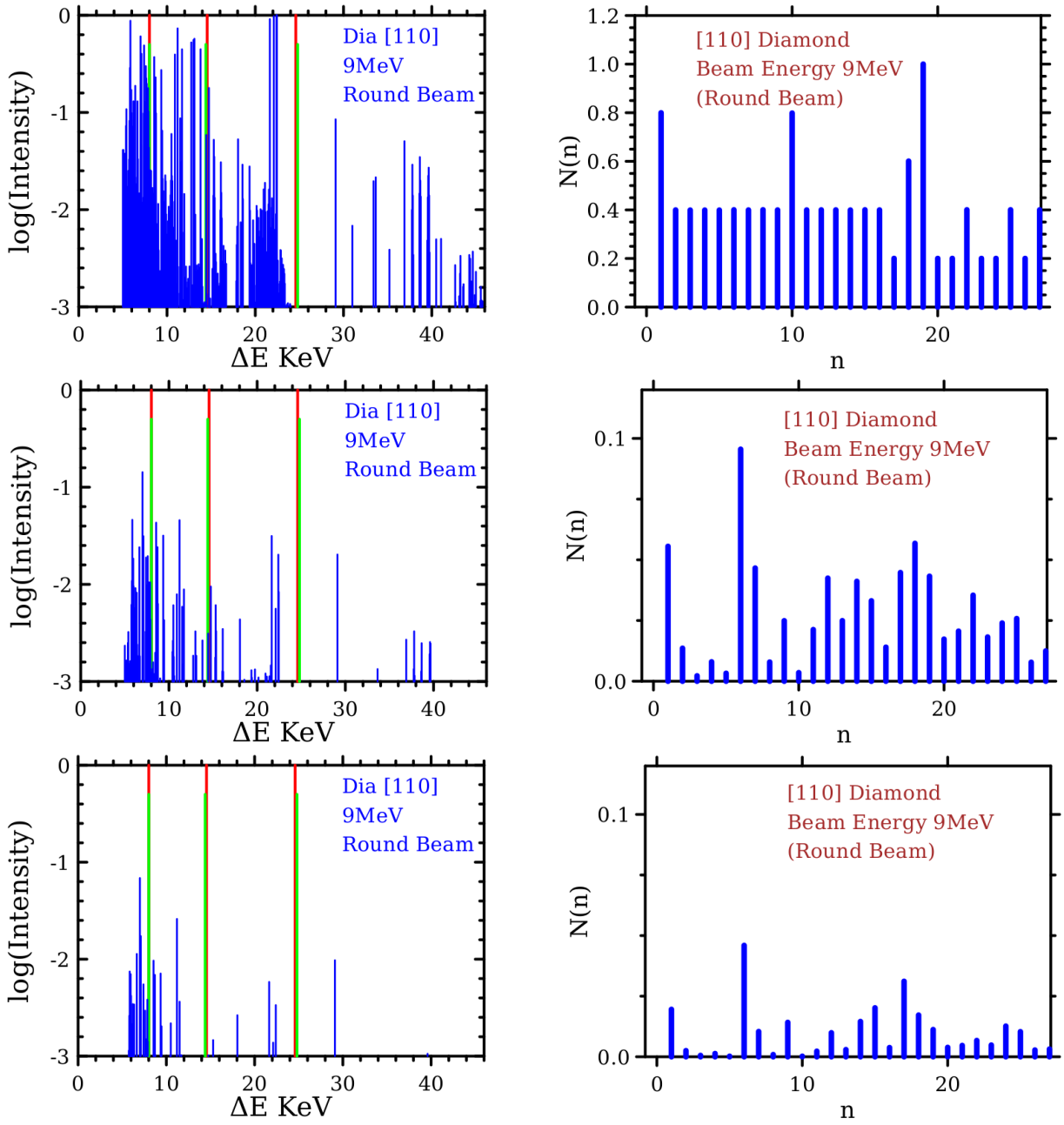

Figure 5.1: Both the left and right plot columns are from the Diamond lattice with orientation [110] at beam energy 9.0MeV. The left column are spectrum plots in the labframe depicted in blue that was generated from this study's 2D Channeling model. In addition, the red lines depict measured data and the green lines depict the Axial Channeling Model's prediction from Genz's paper[5]. The right column plots the occupation probability for each bound state. From eqn. 5.11, each spectrum plot is based on its probability of occupation, $\mathcal{N}(n)$ which is the plot on its immediate right. The beam structure is Gaussian with a $p_c/\sigma_{px} = 0.906$ for the top row, $p_c/\sigma_{px} = 40.5$ for the second row, and $p_c/\sigma_{px} = 70.5$ for the bottom row. Note, for the right sided plots, the top frame's y-axis is one order of magnitude larger than other two frames. All spectrum plots used a common normalizing constant. All occupation plots on the right also used a single common normalizing constant.

5.4 Beam Distribution of Electron Transverse Momentum

Beam emittance is the measurement of the bunch trace space area or equivalently the phase space. For the x degree of freedom (dof), the trace space is (x', x) where in the lab frame $p_x \propto x' = dx/dz$[27].

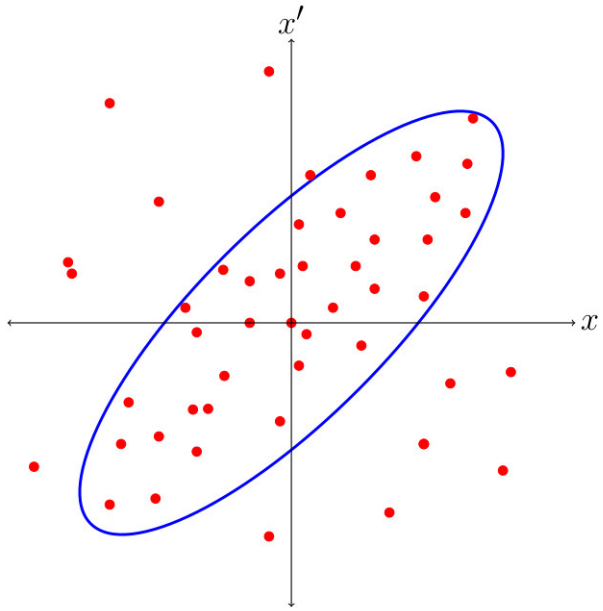

Figure 5.2: The x and x' are the x dof trace space of the electron's motion where $x' = dx/dz$ and z is the longitudinal relativistic beam velocity direction. The blue ellipse encloses a fixed particle density with in that ellipse. As the electron travels along the z direction, the ellipse orientation and minor and major axis may change but the overall area will remain the same. The number of electrons within the ellipse does not change either which conserves the electron trace space density. The red dots represents one electron.

In Particle accelerators, the Liouville's theorem states that conservation of phase space is conserved[28]. The trace space area that is contained within some defined contour, C is calculated by

$$\text{Area} = \int_C x' dx = \text{constant} \tag{5.12}$$

.

Generally but not always, the majority of the electrons with in a bunch can be enclosed in an el-

lipse. The shape of the ellipse may change as the bunch travels through the beam line, but the area of the ellipse is conserved. The electron particles enclosed within the ellipse boundary never changed and thus the particle density within the ellipse boundary does not change either.

The Courant-Snyder's twiss parameters γ_{twiss}, α_{twiss}, and β_{twiss} are the accelerator parameters which describe the envelope path of any particle contained with in the ellipse, Figure (5.2) which is described by an ellipse in Eq.(5.13)[28, 29].

$$(\gamma_{twiss}x^2 + 2\alpha_{twiss}xx' + \beta_{twiss}x'^2) = \varepsilon_x \tag{5.13}$$

If the (x, x') trace space area that the bunch occupies within this ellipse is A_x, then the geometric emittance is defined as

$$\varepsilon_x = A_x/\pi \tag{5.14}$$

Equation 5.14 is true because of the Courant-Snyder's Identity for beam accelerators is

$$\gamma_{twiss}\beta_{twiss} - \alpha_{twiss}^2 = 1$$

At the interaction point where the electron interacts with the crystal within the beamline, the twiss parameters at this point are γ^*, α^* and β^* and the beam is engineered such that $\alpha^* = 0$. With this condition, we can apply a coordinate transformation, $X_N = \frac{x}{\sqrt{\hat{\beta}^*}}$ and $X'_N = \sqrt{\hat{\beta}^*}x'$, for defining the ellipse equation.

$$X_N{}^2 + X'_N{}^2 = \hat{\gamma}^*x^2 + \hat{\beta}^*x'^2 = \left(\frac{x}{\sqrt{\hat{\beta}^*}}\right)^2 + \left(\sqrt{\hat{\beta}^*}x'\right)^2$$

We assume that the probability distribution function for the distribution of electron with in the phase space is Gaussian and assuming $\sigma_{X_N x} = \sigma_{X'_N x} = \sigma_N x$, with the normalization constant is

$1/2\pi\sigma_{Nx}^2$. The Probabililty Distribution Function (PDF) $= f(X_N, X'_N)$ is:

$$\begin{aligned} f(X_N, X'_N) &= \frac{1}{2\pi\sigma_{Nx}^2} e^{-\frac{{X_N}^2+{X'_N}^2}{2\sigma_{Nx}^2}} \\ &= \frac{1}{2\pi\sigma_{Nx}^2} e^{-\frac{(\frac{x}{\sqrt{\hat{\beta}^*}})^2+(\sqrt{\hat{\beta}^*}x')^2}{2\sigma_{Nx}^2}} dX_N dX'_N \end{aligned} \tag{5.15}$$

When calculating the average ellipse area based on the particles distribution in x and x' is equivalent to $\left\langle {X_N}^2 + {X'_N}^2 \right\rangle = \left\langle \gamma^* x^2 + 2\alpha^* x x' + \beta^* x'^2 \right\rangle$, we define this average area in the x trace space as the rms emittance, ε_{RMS_x}, as

$$\varepsilon_{RMS_x} = \int_{-\infty}^{\infty} \left({X_N}^2 + {X'_N}^2 \right) f(X_N, X'_N) dX_N dX'_N = 2\sigma_{Nx}^2$$

Since we can measure what the emittance is for either the x or y trace space, we can then experimentally determine the value of $\sigma_{Nx} = \sqrt{\varepsilon_{RMSx}/2}$. The emittance and in turn the σ_{Nx} defines the beam structure for a Gaussian based momentum distribution.

$$f(x') = \frac{\sqrt{\hat{\beta}^*}}{\sqrt{2\pi}\sigma_{Nx}} e^{-\frac{(\sqrt{\hat{\beta}^*}x')^2}{2\sigma_{Nx}^2}} dx' \tag{5.16}$$

However, since we are using momentum in calculating the probability of occupation, it is a simple matter to transform $x' = dx/dz$ in terms of the momentum, p_x.

$$x' = \frac{dx}{dz} = \frac{1}{\beta c}\frac{dx}{dt} = \frac{p_x}{\gamma m \beta c} \tag{5.17}$$

$$(\gamma m \beta c) dx' = dp_x$$

where p_x is also the transverse momentum of in the beam electron's rest frame. The beam distri-

bution in the transverse momentum space is then,

$$f(p_x) = \frac{\sqrt{\beta^*}}{\sqrt{2\pi}(\gamma m\beta c)\sigma_{Nx}} \exp\left[-\left(\frac{\beta^*_{twiss}}{2\sigma^2_{Nx}}\right)\left(\frac{p_x}{\gamma m\beta c}\right)^2\right] dp_x \tag{5.18}$$

$$= \frac{1}{\sqrt{2\pi}\sigma_{px}} \exp\left(-\frac{p_x^2}{2\sigma^2_{px}}\right) dp_x \tag{5.19}$$

where

$$\sigma_{px} = \sigma_{Nx}\frac{\gamma m\beta c}{\sqrt{\beta^*_{twiss}}} = \sqrt{\frac{E}{2\pi}}\frac{\gamma m\beta c}{\sqrt{\beta^*_{twiss}}} = \sqrt{\frac{\varepsilon_{RMS_x}}{2}}\frac{\gamma m\beta c}{\sqrt{\beta^*_{twiss}}} \tag{5.20}$$

You will notice the momentum in the electron's restframe is depicted in Eqn.(5.4) as a relativistic momentum. To check for consistency whether this correct, we apply the Lorentz transformation, Λ^μ_ν, to the electron's momentum four-vector from the labframe momentum four-vector p^ν to the rest frame momentum four-vector p^μ . As stated earlier, in the lab frame the electron's relativistic velocity, v_z component or beam direction, is along the $[hkl]$ lattice orientation with $\dot{\vec{z}} = \dot{z}_{[hkl]}$. The electron rest frame is defined along the z component where $\dot{z}_{[hkl]} = 0$. Since the eigenstate transverse momentum is in the electron's rest frame and the incident electron's transverse momentum is in the lab frame, the incident electron is not in the correct coordinate frame to be expanded in terms of eigenstates. Therefore a Lorentz transformation $\Lambda^\mu_\nu p^\nu = p^\mu$ from the lab frame to the moving frame four vector, p^μ is required. The incident electron's momentum four-vector in the lab frame is

$$p^\nu = (\gamma m_e c, \gamma m_e \dot{x}, \gamma m_e \dot{y}, \gamma m_e \dot{z})$$

where m_e is the electron mass and γ is the Lorentz factor. After applying the Lorentz transformation to the restframe, the electron's restframe's momentum four-vector takes the form

$$p^{\mu} = (m_e c, \gamma m_e \dot{x}, \gamma m_e \dot{y}, 0)$$

Therefore, both the physical explanation for applying the Lorentz transformation and the results of the transformation are in agreement with the trace space x' transformation to its momentum space $p_x = \gamma m_e \dot{x}$. Therefore, to determine the P_Occupation, we need to know the beam's structure σ_{kx} in Eqn.(5.10) which is expressed in terms of the beam's emittance and β_{twiss} as well as the beam's energy which is in terms of Lorentz factor, γ.

$$\sigma_{kx} = \sigma_{px} a_x/(h2\pi) = \sigma_{Nx} \frac{\gamma m \beta c}{\sqrt{\beta^*_{twiss}}} \frac{a_x}{h2\pi} = \sqrt{\frac{\varepsilon_{RMS_x}}{2}} \frac{\gamma m \beta c}{\sqrt{\beta^*_{twiss}}} \frac{a_x}{h2\pi} \tag{5.21}$$

In accelerator physics, the experimenters can manipulate the beams structure by manipulating the emittance, β_{twiss}, beam energy, and even the beam momentum distribution within the ellipse's conserved area. From this manipulation, the experimenters than can then control to some degree what states that can be occupied and deny other states from being occupied. This then provides tunable capabilities in selecting the desired transition emission energies.

Chapter 6

Detector Calibration and Pileup Mitigation

The channeling radiation experiment was conducted at the Fermilab Accelerator Science and Technology (FAST). Using a diamond crystal, the experiment was focused on generating channeling radiation from a [110] lattice orientation. Since complications in the experiment prevented any meaningful data, this study had no spectrum data to compare with its predictions. In this chapter, the focus was on calibrating the X123CdTe Amptek detector used in the experiment and reduce deadtime and pileup affects

Experimental Setup

The beamline begins with a Radio Frequency (RF) gun, two cryomodules, followed by a 4-dipole magnetic bend chicane and then runs through the crystal interaction point (Crystal lattice orientation [110] with $165.4 \pm 3.5 \mu m$ thickness) followed by dipole magnet which steers the beam into the beam dump. Figure 6.1 illustrates the beamline. Transverse emittance rated at $0.01 - 0.1 \mu m$ with a Gaussian momentum distribution.

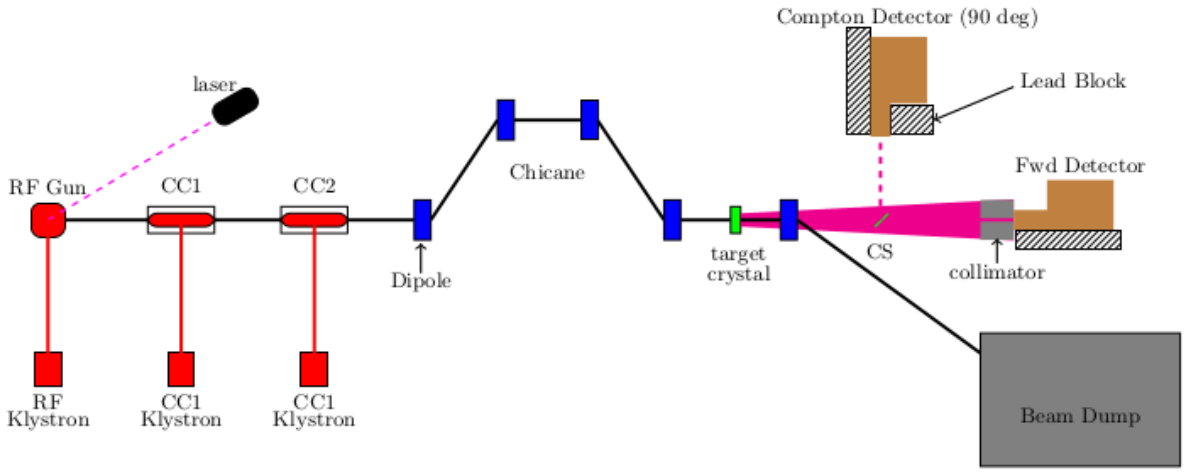

Figure 6.1: RF gun focuses and accelerates the electron bunch to 4MeV into the CC1 and CC2 superconducting accelerating crymodules which further accelerates the electrons to 42.5MeV. Since the electrons are relativistic, electron-crystal induced Bremsstrahlung and channeling radiation are collimated to a $\frac{1}{\gamma}$ opening angle. The induced radiation all passes into the forward detector except for a small portion which is compton scattered, using a plastic disc (CS), into the 90 degree detector. To reduce photon flux into the forward detector, a combination of lead and brass collimator were also installed. Focusing quadrupoles were used along the beamline but are not shown in this diagram.

The electron source is a 1-1/2 cell 1.3-GHz cylindrical-symmetric RF gun comprising of a Cs_2Te photo-cathode illuminated by an ultraviolet (UV, λ = 263 nanometers) [30]. The photo-cathode drive laser illuminates the photo-cathode with a frequency that is adjustable from 1 to 3 MHz with a 33 picosecond laser pulse length. With the drive laser set at 1 MHz, it can generate a group of electrons called a bunch every 1μ second. Upon exiting the RF gun, the generated bunch now has approximately 4 MeV of energy per electron.

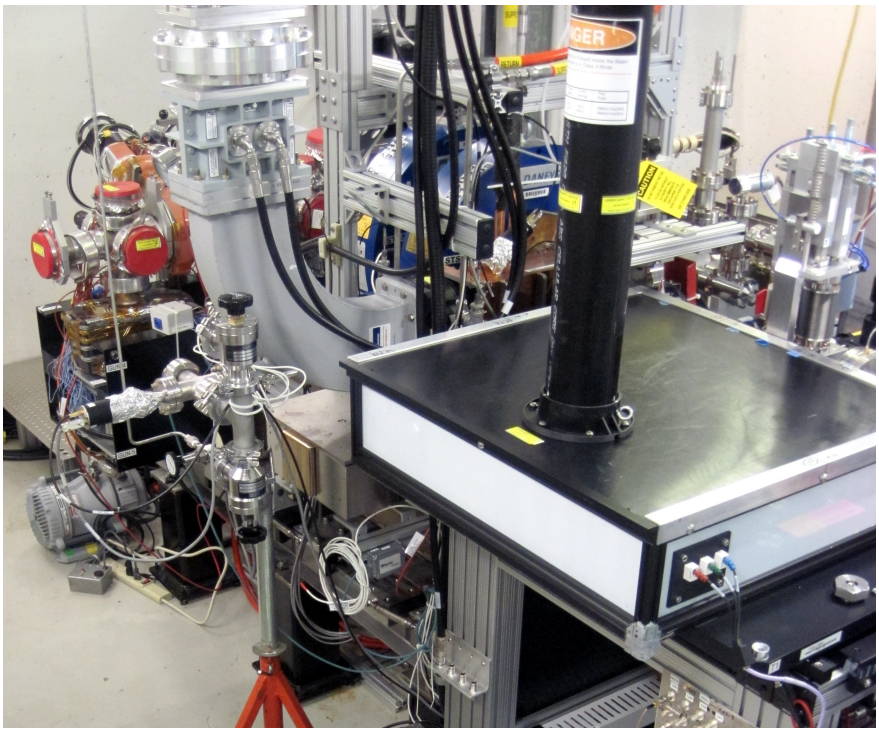

Figure 6.2: RF Gun, the two blue solenoid are centered on the photocathode. The microwave rectangular tubing on the left and entering near the blue solenoids are microwaves that powers the RF cavity which accelerates the bunch to approximately 4 MeV [6].

The two superconducting accelerating cryomodules, CC1 and CC2 accelerates the bunch from 4 MeV to approximately 42.4 MeV. The macropulse duration of the RF waves which drive the RF gun and the two cryomodules ranges from 600 to 1000μ seconds. Within each RF macro pulse, the number of bunches generated are limited to 3000 maximum [31]. Generally, this experiment ran approximately 240 bunches per RF macro pulse. The repetition rate (reprate) is the frequency RF macro pulses in one second. FAST beamline can run from 1 -5 Hz reprate. In this experiment, the reprate was set at 1 Hz.

The diamond crystal is mounted with a [110] orientation on a device called a Goniometer. The Goniometer has three positional settings. Position one is that the beamline has no target in the beampipe. Position two has the diamond crystal target positioned in the beamline. Position three has the aluminum foil target inserted into the beamline.

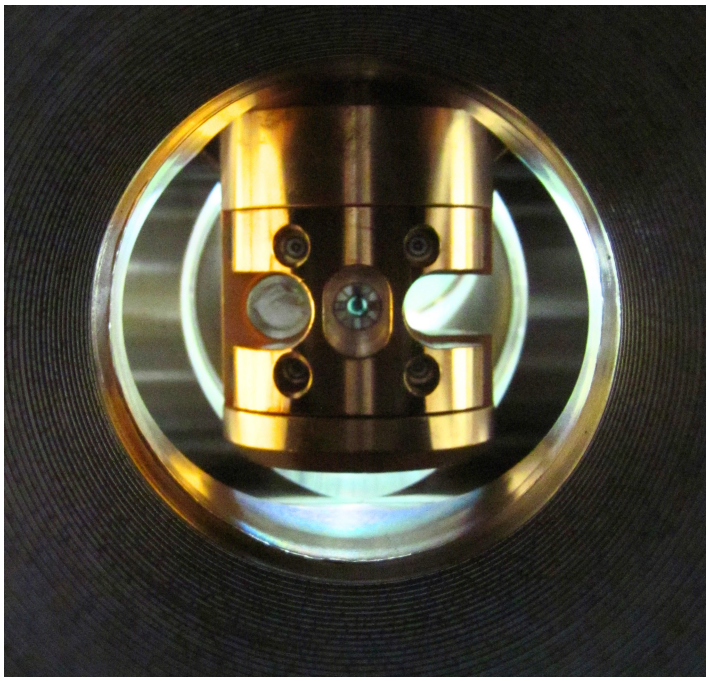

Figure 6.3: Goniometer apparatus with three positional states. The right most aperature is position one, (the open position), where no target is in the beamline. Position two is the center aperature where the diamond crystal target is mounted and placed into the beamline, and the third position is the far left aperature containing the aluminum foil target which is place into the beamline[6].

When the crystal is in the beamline, the goniometer can change its pitch, yaw and vertical position within the beam pipe to achieve the critical angle condition for channeling radiation. For this experiment, instead of establishing the beam line with the crystal's [110] axial orientation, the beam is oriented parallel to the (110) plane which is described by the intersection of [110] and [001] axial lines.

Both the forward detector and the 90 degree (Compton) detectors are the X123CdTe Amptek detector. The forward detector was to calibrate alignment of the crystal with the beam, measure the dark current's Bremsstrahlung contributions to background, and (if possible) measure the channeling radiation. Depending on the forward detector's collimation and the magnitude of the beam

current, signal pileup on the forward detector will most likely dominate the forward detector's data collection. To measure channeling radiation in the 90 degree detector, a plastic plate is placed into the path of the generated photons. Due to Compton scattering, the photons scattered into the 90 degree detector are approximately 6 orders of magnitude less than the number of photons generated from the Bunch-Crystal interaction. As illustrated in Figure 6.1 , the forward detector is located above the beam dump. The 90 degree detector is located approximately one meter away, perpendicularly, from the radiation path induced from the bunch-crystal interaction. Sources of radiation that can affect the detector's measurement are beam dump radiation, dark current generated Bremsstrahlung radiation, background radiation, and bunch-crystal generated Bremsstrahlung and channeling radiation. Lead block shielding is placed around the detectors to shield from beam dump radiation and dark current induced radiation. Although the forward detector's will receive both dark current and bunch-crystal induced radiation, the lead shielding around the detector will prevent these radiation from interfering with the detector solid state circuits. Consequently, due to the beam dump's radiation emissions, both the forward detector and the 90 Degree (Compton) detector must be shielded from these radiation effects. Dark current are a stream of low luminosity, low energy electrons that are continuously generated and accelerated down the beamline whether the RF is on or off. Due to their high emittance, the stream of electrons have a high probability of scraping the beam pipe and interacting with the crystal and the crystal's thin copper mount which generates Bremsstrahlung radiation into the detector. Since the energy of the dark current is relativistic at around 4 MeV with no RF pulse and approximately 44 MeV with the RF pulse is on, the dark current induced Bremsstrahlung radiation is collimated with a $\frac{1}{\gamma}$ opening angle. This means that most of the radiation generated by the dark current is oriented along the beam line. The 90 degree detector's off center from the beam line was to mitigate or eliminate all dark current induced radiation counts except what is plastic plate scatters into the detector's window. Since the Chicane is on the same side of main beamline direction as the 90 degree detector, dark current interaction in the chicane's beam pipe would irradiate the detector with generated Bremsstrahlung radiation. Therefore, in this particular setup, the 90 degree detector also had to have lead shielding to protect

it from Chicane dark current induced radiation.

The chicane was also designed to have a beam scraper at point 3. The beam scrapper would eliminate any beam halo and also mitigate or eliminate dark current. Since the beam scrapper was not available in this experiment, the chicane's dipole magnets were manipulated to steer any beam halo and dark current into the beam pipeline to scrape these unwanted electrons out of the beam. By doing this in the chicane, the Bremsstrahlung generated from the scraping are removed from the main beam line where the forward detector is located.

This experiment had numerous issues that had to be resolved to ensure that the conditions were met for a successful experiment. Although not inclusive, the following is a general list of major experimental setup issues that had to be solved or accounted for.

- Beam emittance did not exceed critical angle for channeling.
- Reduce dark current contribution to Bremsstrahlung background noise.
- Scrape any beam halo to reduce contributions to Bremsstrahlung background noise.
- Goniometer manipulation to set crystal in correct orientation.
- Shielding detectors from Beam Dump Radiation, dark current generated Bremsstrahlung radiation, and beam halo generated Bremsstrahlung radiation.
- X123CdTe Amptek Detector calibration.
- X123CdTe Amptek Detector deadtime and pileup data corrections.
- Eliminate detector pileup from high scattered photon flux rates.

From this general list, this study specifically focused on the detector calibration and the deadtime and pileup corrections setup issues.

X123CdTe Amptek Detector Calibration

Detector energy calibration was already determined. The X123CdTe AMPTEK detector has the capability to discretely vary the number of multi-channels (256, 512, 1024, 2048, 4096, and 8192)[32]. In our experiment, we selected 1024 channels. The channel to energy calibration was [33]

$$\text{Channels/KeV} = 0.837 \times \text{Gain} \quad \text{(Forward Detector)} \tag{6.1}$$

$$\text{Channels/KeV} = 0.861 \times \text{Gain} \quad \text{(90 Degree Detector)} \tag{6.2}$$

Since the gain was adjustable, the selected gain for this experiment was set to Gain = 8.0. At this setting, the Forward Detector's channel to energy calibration (Calib) = 6.696 Channels/KeV.

The detector also has a Fast Channel and Slow Channel to detect and characterize the arriving photon energy pulse. The slow channel utilizes a trapezoid pulse shaper to accurately determine the pulse height (Photon Energy). For both channels, the peaking time is the parameter that defines the "the time required for the shaped pulse to reach its maximum amplitude ..." [34]. The shorter the peaking time corresponds to reducing the slow channel's dead time. When a photon arrives at the detector, dead time is the time required for the detector to be able to accurately record a subsequent photon. In this detector, the slow channel's deadtime is equal to the peaking time. If the peaking time is too small, then the slow channel will begin to record random noise. The longer the peaking time, then the longer the deadtime. Long deadtimes can cause pileup errors. Peaking times for the slow channel can be 0.2μ sec to 102μsec. The fast channel also utilizes a trapezoid pulse shaper but its peaking time is 120ns which is a great deal smaller than the slow channel. The fast channel is designed only to detect a photon pulse and not measure its pulse height. When a photon arrives at the detector, the fast channel allows the detector to reject any subsequent photons arriving within the deadtime. The fast channel gives the detector the ability to significantly reduce pileup errors. Both the slow and fast channels have specific signal thresholds. Photon signal energies that are less than the defined threshold settings are not considered. To optimize the detector, the peaking times and both the Fast and Slow Thresholds must eventually be determined. To determine optimal

settings, 125 spectrums of Cobalt 57 were collected with an acquisition time of 1 hour and a gain setting of 8. Each spectrum recorded was one out of 125 possible combinations of peaking time, Fast Channel Threshold (THFA), and Slow Channel Threshold (TFSL). The different settings of these three parameters are the following:

Peaking Time: [0.2μsec, 0.6μsec, 1.0μsec, 2.0μsec, 3.0μsec,]

THSL: [0.1, 0.3, 0.5, 0.7, 0.9]

THFA: [10.0, 20.0, 30.0, 40.0, 50.0]

Although the optimization for the best set of these three parameters is required, this part of the calibration of the detector was not the focus of this study. However, these 125 Co57 spectrum files were used to calibrate the efficiency of the detector.

Detector Efficiency

The detector efficiency determines the percentage of photons that are successfully detected and is measured as a function of photon energy. The actual detector is made up of a variety of materials that the photons must transit through before arriving at the CdTe Active Detector Volume (Interaction zone). Figure 6.4 illustrates that the photon must transit through a $100\mu m$ thick Beryllium (Be) which is a 3×3 area size window separating the environment from inner mechanisms of the detector [35]. After Gamma photon transits through the Be window, it also must transit through two materials before reaching the interaction zone. These two materials are Platinum (Pt) Contact layer of [$0.2\mu m$] and CdTe Deal Layer which is typically suppose to be around [$0.15\mu m$] thickness. With the exception of the interaction zone, each material that the photon transits through, a percentage of photons are absorbed depending on the energy of the photon.

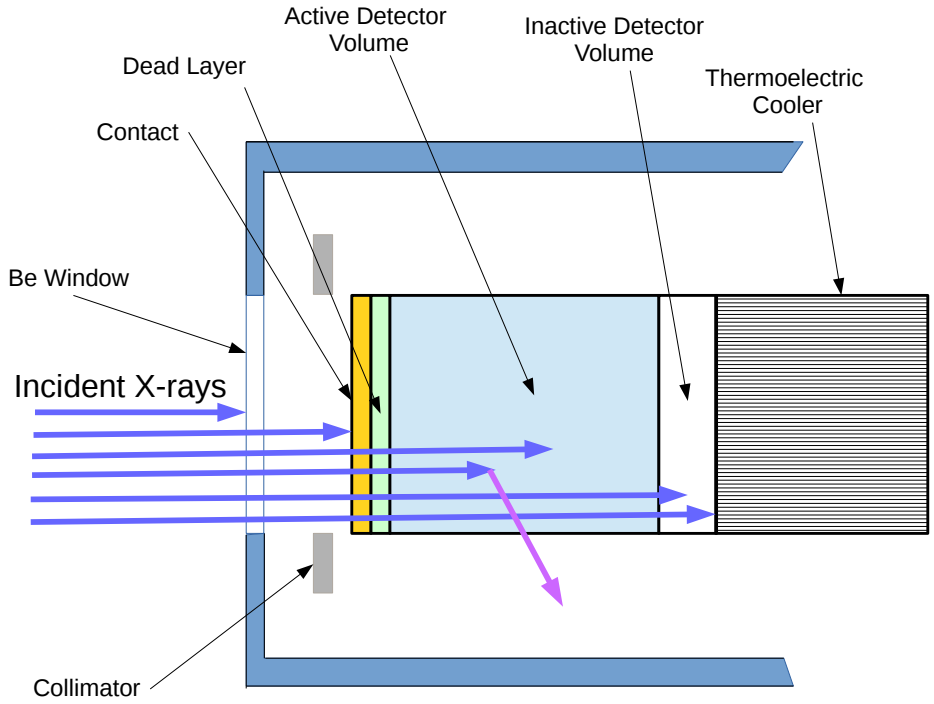

Figure 6.4: Cross section view of X123 CdTe Detector: The incident X-ray photon enters the Be window (3×3mm with thickness of $[100\mu m]$) then passes through Platinum (Pt) Contact Layer $[0.2\mu m]$ and the CdTe Dead Layer typically $[0.15\mu m]$ thickness before interacting with CdTe Active Detector Volume with thickness "t". The blue arrows represent X-Rays transiting through various stages of the material. The pink arrow indicates that the photon instead of being absorbed in the active detector volume, the photon was scattered out of the detector and not registered. [7].

Detector Efficiency depends on CdTe Active Volume Effective Thickness "t". To determine each detector's effective Thickness "t", we measure the ratio of two emission intensities where the detector efficiency is not at 100%. Co57 has two emission peaks that means this requirement: 14.4 KeV & 122.06 KeV.

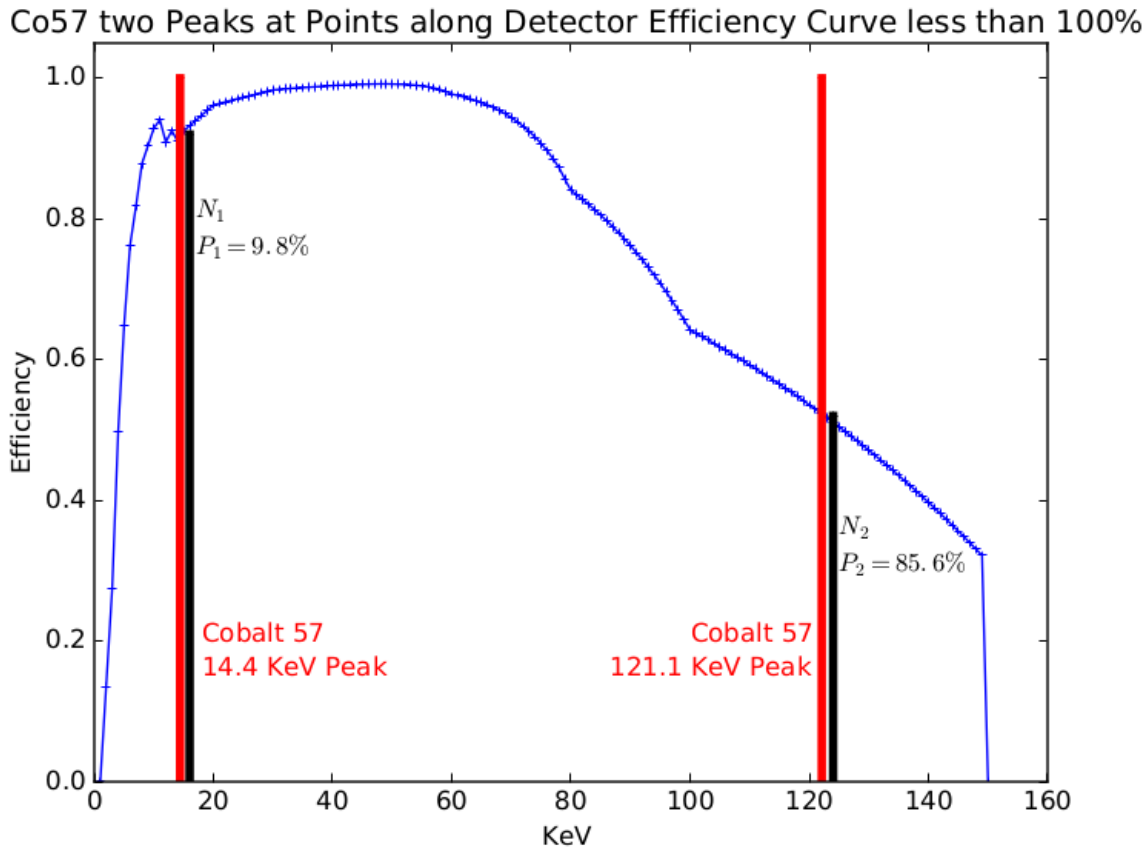

Figure 6.5: The blue curve represents a detector efficiency curve using t = 1mm. If the efficiency was 100% both the 14.4 KeV Peak 1 and the 122.1 KeV Co57 Peak 2 emissions would be recorded as indicated by the red bar. However, the black bar represents the actual recording. For Peak 1 emissions, the probability of emission is 9.8%. For the Peak 2 emissions, the probability of emissions is 85.6%. N_1 would represent the actual intensity measured for For Peak 1. Likewise, N_1 is the measured intensity for Peak 2

Although we do not know what "t" is, the blue efficiency curve in Fig. 6.5 is a good representation. Therefore, Co57's two emission peaks are acceptable candidates for numerically determining the actual effective thickness of the active Detector Volume. The equation for determining the effective thickness is:

$$\frac{N_1}{N_2} = \frac{P_1 P_{1env}}{P_2 P_{2env}} \frac{(1 - e^{-\mu_1 t})}{(1 - e^{-\mu_2 t})} \approx \frac{P_1}{P_2} \frac{(1 - e^{-\mu_1 t})}{(1 - e^{-\mu_2 t})} \tag{6.3}$$

where N_1 is Co57 Peak 1's 14.4 KeV Photon measured intensity and N_2 is Co57 peak 2's 122.06 KeV photon measured intensity. $P_1 = 9.8\%$ and $P_2 = 85.6\%$ are the probabilities of emission for

Peak 1 and Peak 2 respectively. The CdTe linear absorption coefficients μ_1 and μ_2 are based on Peak 1 and Peak 2 emission energies respectively. P_{1env} and P_{2env} approximately equal to one are the probability of photon absorption due to environment materials: Air, Be (window), Pt (contact layer) and the CdTe (dead layer).

$$P_{1env} = e^{\mu_{1Air} t_{Air}} e^{\mu_{1Be} t_{Be}} e^{\mu_{1dead} t_{dead}} e^{\mu_{1c} t_c} \approx 1$$

$$P_{2env} = e^{\mu_{1Air} t_{Air}} e^{\mu_{2Be} t_{Be}} e^{\mu_{2dead} t_{dead}} e^{\mu_{2c} t_c} \approx 1$$

where μ_{iAir}, μ_{iBe}, μ_{idead}, and μ_{ic} are the linear absorption coefficients for Air, Be (window), Pt (contact layer) and CdTe (DeadLayer) for Peak's i $\in$ [1,2]. Likewise, the thickness of each of these environmental materials are t_{Air} for air and etc. for the other environmental materials. Since in equation 6.3 all variables are either measured or known, the solving for "t" is done numerically using the Bisection method.

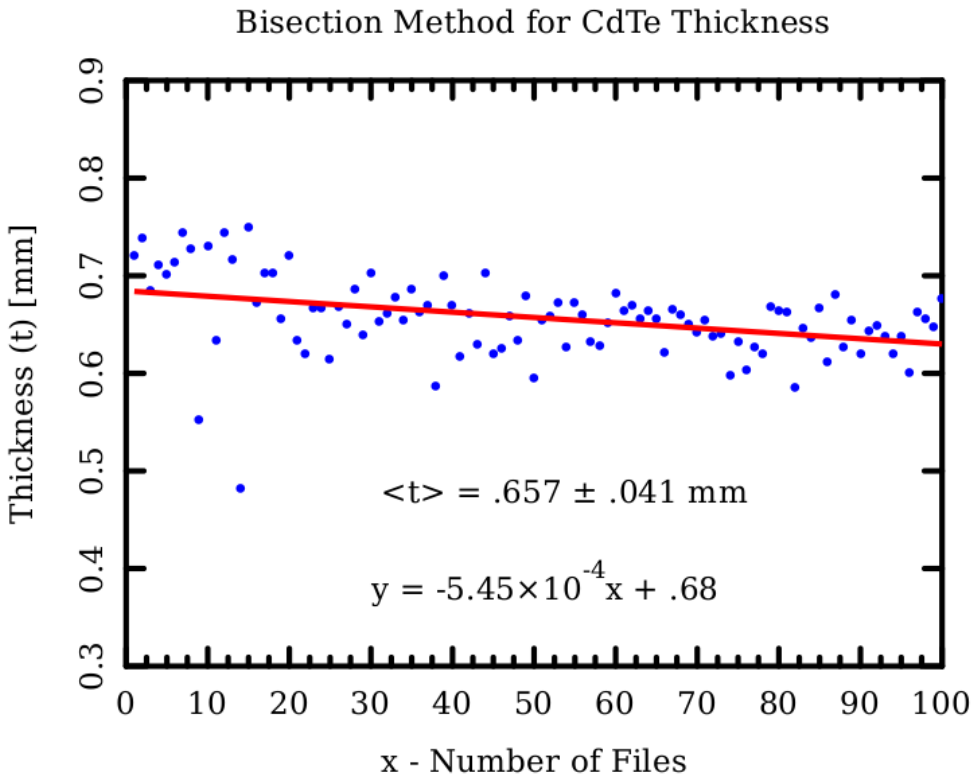

Figure 6.6: estimates the effective "t" thickness the CdTe Active Detector Volume. 100 spectrum files of Co57 emissions were recorded based on different parameters: Peaking time, Fast Threshold, and Slow Threshold limits with a gain set at 8. For each file, the intensity of two peaks were measured and using eqn. 6.3 were numerically solved for the effective thickness "t". Along the x-axis, every integer from 1 to 100 represents the calculated thickness for the corresponding file number. The estimated average thickness from the numerical calculation of "t" from eqn. $< t >$ = 0.657mm was average over the 100 file samples with an error of $\pm$ 0.041mm

As stated earlier, over a 125 spectrum files were recorded for Co57 radioactive emission peaks. Each spectrum recorded was one out of 125 possible combinations of peaking time, Fast Channel Threshold (THFA), and Slow Channel Threshold (TFSL). Since the THFA threshold set at 10.0 was too low and hence noise was to high, this parameter was thrown out. This then left 100 viable Co57 spectrum files to use to calculate the effective thickness. Nominally, the CdTe effective thickness is designed to be approximately 1mm. However, in this forward detector, Fig. 6.6 shows that the effective thickness was noticeably less at 0.657mm.

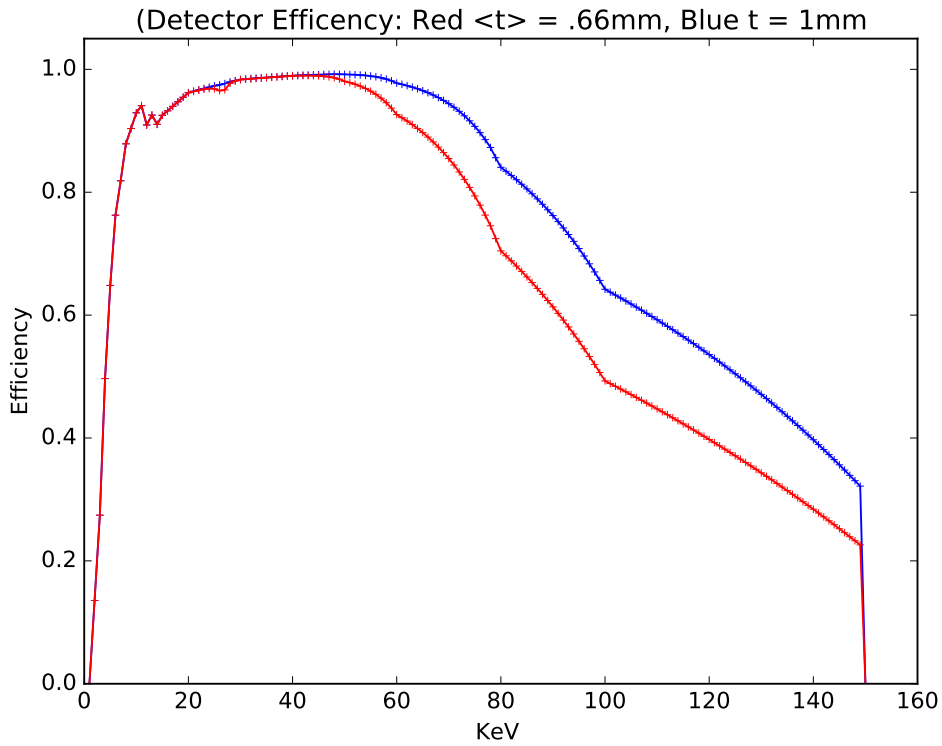

Figure 6.7: is the Forward Detector's efficiency curve with blue curve representing Amptek's nominal thickness of 1mm. The red efficiency curve is based on the measured estimated effective thickness "t"

Figure 6.7 depicts the Detector's efficiency based on the Amptek's designed effective thickness "t"=1mm as compared to the determined effective $\langle t \rangle = 0.66mm$

Hole Tailing Affects on Measuring Peak Intensities N_1 and N_2

For CdTe materials, the large Z (atomic number) has the advantage of having high stopping power for photons. The high stopping power means that the probability of high energy photons interacting with the CdTe molecule is also high. All though there are other interactions such as Compton scattering, the primary interaction with the CdTe in the Active Detector Volume is photon energy ionizing its electrons creating a number of electron-hole pairs equivalent to the photon energy absorbed. Under a bias voltage, these charge carriers holes(+) and electrons(-) must travel a fixed distance before being collected. The holes drift toward the Cathode(-) and the electrons drift to-

ward the Anode(+). The charge collection process collects both the holes (positive charge) and electrons (negative charge) to determine the total induce charge, Q.

$$Q(t) = \frac{q_0}{d}(\text{electron drfit distance} + \text{hole drift distance}) \tag{6.4}$$

"This induced charge starts at zero when the electrons and holes are first formed by the ionizing particle and reaches its maximum of q_0 when both species have been collected[34]."

At photon energies above 50KeV, hole-tailing effects changes the photon peak's Gaussian structure to an increase shoulder on the low energy side of the peak. This then complicates the process in determining the intensity of a peak. For a Gaussian structure peak, we would integrate Full Width Half Maximum (FWHM) to determine the peak's intensity. With hole-tailing effects, using the FWHM integration interval would not accurately represent the peaks intensity. For a CdTe material, when a hole and electron is produced, the electron travels faster than the hole. In addition, due to normal impurities in the crystal, the electron and or holes can be trapped as they move towards Anode and Cathode respectively. Due to this trapping, the life time for electron and hole is 3μ sec and 1μ sec, respectively. From this, two results occur, at high energies, the probability of interaction through the depth of the Active Detector Volume is uniform. If the photon interacts close to the Cathode, all the holes are generally collected and the electrons are also collected. However, if the photon interacts near the Anode, all the electrons are collected but some of the holes are not collected due to slow transit time and short lifetimes. This creates a lower charge collection which in-turn contributes to the intensity and widening of the peaks lower energy shoulder side. Second, if the peaking time is small, the slow transit time of the holes will prevent full charge collection before the detector pulse shaping is finished.

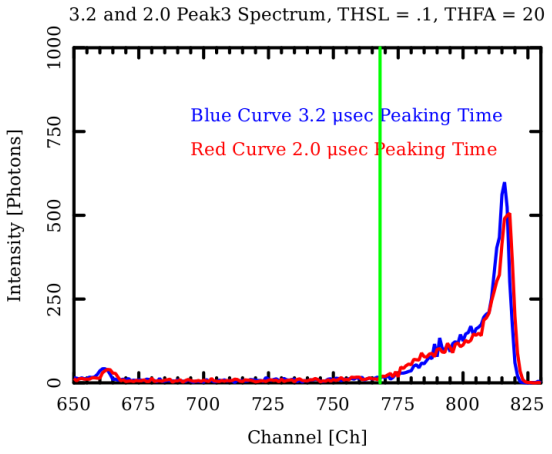

Fig. 6.8a

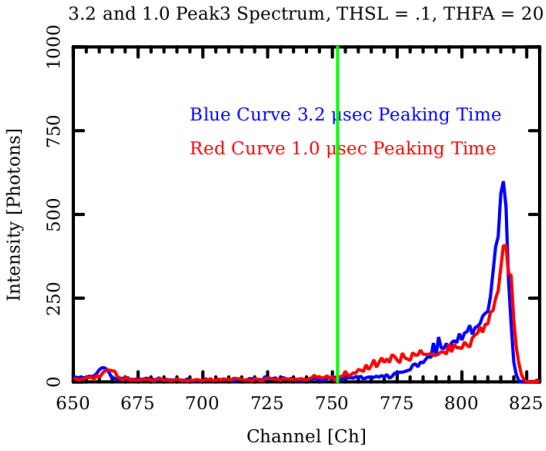

Fig. 6.8b

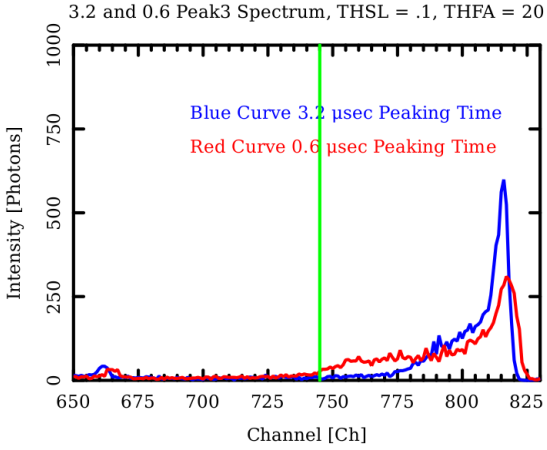

Fig. 6.8c

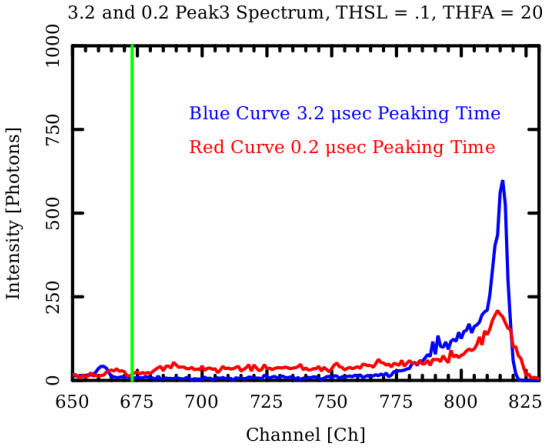

Fig. 6.8d

Figure 6.8: illustrates that when decreasing the detector's peaking time, hole-tailing affects increases the shoulder width on the low energy side of the peak. Using 3.2μsec as a baseline, we decrease the peaking time and compare the two peak spectrums of 122.4KeV. The blue curve represents 122.4KeV peak at 3.2μsec peaking time. The red curve represents smaller peaking times: Fig.(6.8a) 2.0μsec, Fig.(6.8b) 1.0μsec, Fig.(6.8c) 0.6μsec, and Fig.(6.8d) 0.2μsec. The green vertical line delineates where red curves shoulder from hole-tailing contributions cut off. Threshold settings for Slow and Fast Channels were set at 0.1 and 20 respectively

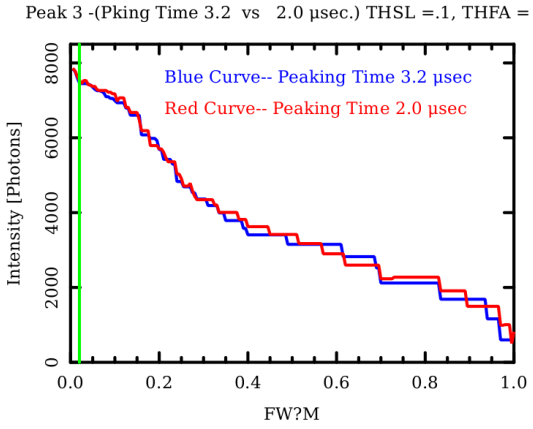

Fig. 6.9a

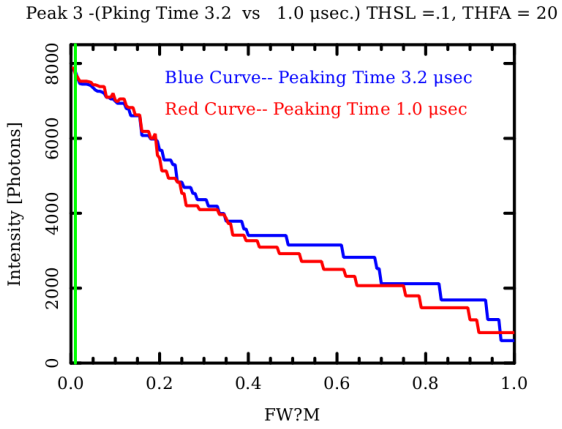

Fig. 6.9b

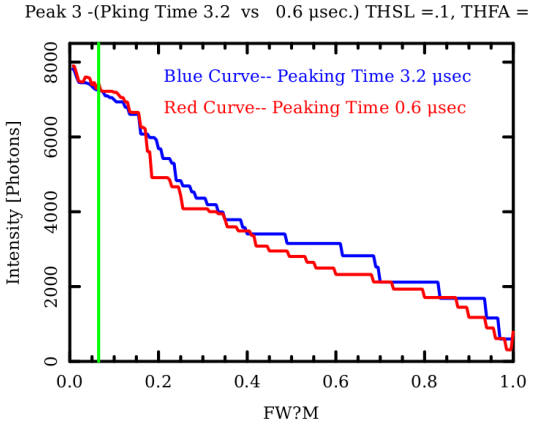

Fig. 6.9c

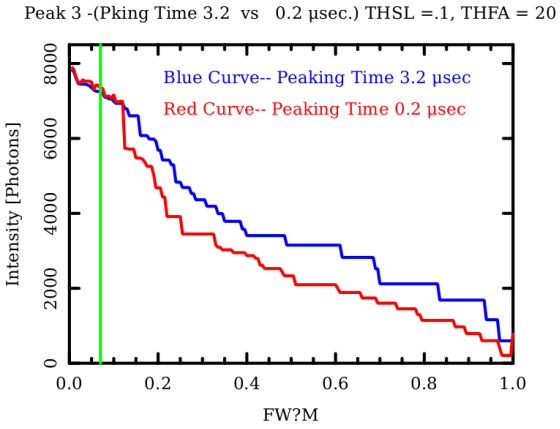

Fig. 6.9d

Figure 6.9: varies the full width question (**?**) maximum (FW?M) from near zero to maximum height. Integrating over the FW?M interval, the peak's intensity is plotted as a function of FW?M interval for various peaking time settings. Using 3.2μsec as a baseline, we decrease the peaking time and compare the peak's intensity vs FW?M for peak 3 at energy 122.4KeV. The blue curve represents intensity vs FW?M at 3.2μsec peaking time. The red curve represents smaller peaking vs FW?M: Fig.(6.9a) 2.0μsec, Fig.(6.9b) 1.0μsec, Fig.(6.9c) 0.6μsec, and Fig.(6.9d) 0.2μsec. The green vertical line delineates where red curves shoulder from hole-tailing contributions cut off. As the peaking time decreases, the intensities between the two peaking times are nearly equivalent when the integration interval is set at around one tenth of the maximum. Threshold settings for Slow and Fast Channels were set at 0.1 and 20 respectively.

Figure 6.8 illustrates that at high energies, hole-tailing effects increase as the peaking time decreases. The lower energy shoulder of the peak increases and extends to lower energies as the

peaking time decreases. Because of the slower hole's transit times, the lower peaking times prevents sufficient time to collect the holes in the charge collection process. Figure 6.9 relies on the assumption that the intensity for the peak 3 should be the same regardless of the peaking time. Therefore, we compare the intensity based on the integration intervals of various FW?M. When comparing the intensity for Peaking time 3.2 μsec versus lower peaking times, the curves diverged at some point. For peaking times of 0.2 μsec, some where around FW.1M was sufficient for both curves to match in intensity. Not much above that interval, the intensity curves would then diverge. Since FW.1M worked for all peaking times, we used this interval to determine the intensities for N_1 and N_2 in calculating the effective "t" thickness for the Effective Detector Volume. In addition, Knoll indicated that using FW.1M was used to "...specify the severity of tailing ... [34]" pg 445 Knoll. Amptek also stated that FWHM and even 2FWHM may not be sufficient to determine the intensity of the peak.

Peaking times affects on Photon Peaks at low Energies

At lower energies, we do not see the effects of hole-tailing. At lower energies, the absorption is not uniform. Rather, at these lower energies, the interaction occurs closer to the Cathode. Hence, from the production of electron hole pairing, the holes have a very short distance for charge collection. Thus, peaking time and trapping of electrons and holes are insignificance. However, it appears as peaking time decreases, the photon peak's Gaussian curve's FWHM increases. In addition, the photon's peak also appears to shifts to a higher energy. However, due to detector change in peaking time, this also shifts the channeling zero energy. In this case, the zero channeling had shifted to the right. If we re-calibrated for this shift, the photon energy would not change.

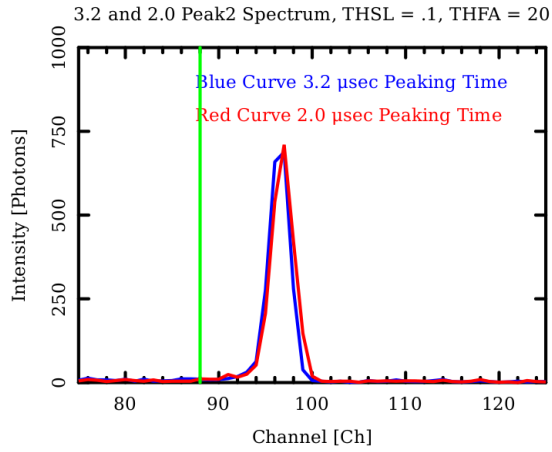

Fig. 6.10a

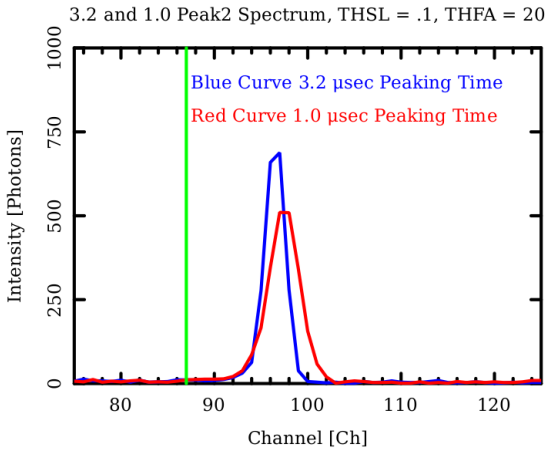

Fig. 6.10b

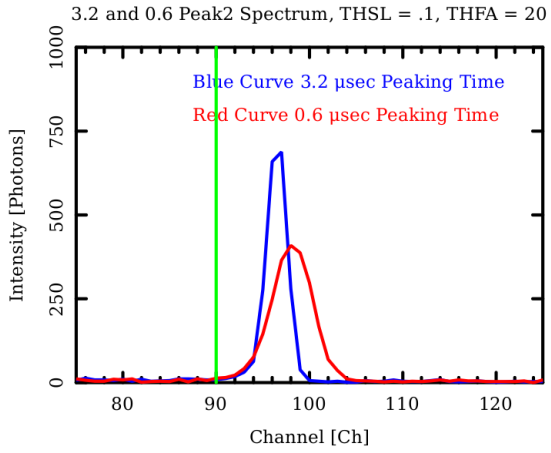

Fig. 6.10a

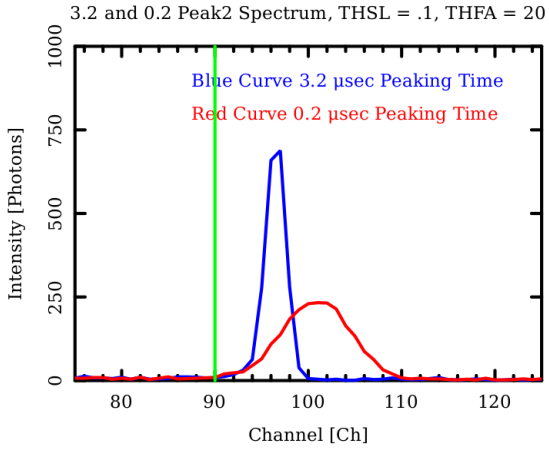

Fig. 6.10b

Figure 6.10: shows the spectrum for peak 2 at 14.4KeV. The blue curve represents Peak 2 spectrum at base line peaking time 3.2 μsec. The red curve represent four shorter peaking times: 3 μsec, 1 μsec. 0.6 μsec, and 0.2 μsec. The Slow and Fast Channel Thresholds were set at 0.1 and 20 respectively. As the peaking time decreases, the FWHM increases and the photo peak shifts to a higher energy.

When comparing the baseline peaking time 3.2μsec with the lower peaks, the FWHM was sufficient in calculating the intensities. The intensities match regardless of the peaking times. This widening of the FWHM as the peaking time decreases is a function of insufficient time to fully collect the charge generated from the photon. As for the shift in the photo peak, there is no clear physical reason why this should occur.

In summary, at lower energies, the photon peak maintains a Gaussian shape for all defined peaking times. As the peaking time decreases, the detector is not able to fully collect the charge which then widens then Gaussian curve. In addition, as the peaking time decreases, the zero channeling channel has shifted. This requires a recalibration of the detector to determine the channel/KeV.

Parameters to reduce Detector Pileup Reduction

The X123CdTe detector utilizes both the Fast Channel and the Slow Channel to detect and characterize the incident X-Ray Photon. To avoid pileup, the Slow Channel must have enough time to be able to fully collect and measure the induced charge generated from the photon before another photon arrives. If another photon arrives during this collection process, the Slow Channel will instead recorded both photon energies as a single photon energy. This error in recording the spectrum is called pileup. To understand how pileup can occur within this detector, we must look at how the Slow Channel's pulse shaper affects this process.

The slow channels pulse shaper depends on the peaking time plus the width of the flat peak. Therefore, the deadtime for this Detector is $\tau_{dead} = \tau_p + \tau_{flat} \approx 1.05 \times \tau_p$. The detector collects the induced charge from the photon over the duration of the deadtime τ_{dead}. The amount of charge collected at the end of this deadtime is recorded as the photon's energy. After the deadtime has expired, the detector is ready to detect a following photon with no risk of pileup.

As stated earlier, FAST has an adjustable 1 to 3MHz photo-cathode drive laser with a 0.33 picosecond laser pulse length. Therefore, the electron bunch length is equivalent to $\tau_{pulse-width} =$ 0.33 picoseconds. If the laser is running at 3MHZ, then the pulse gap is approximately τ_{gap} $\approx$ 1/3MHz = 0.33μ sec. If the laser is running at 1MHz, then pulse gap, the time between bunches, is $\tau_{gap} \approx 1\mu$ sec. Note, the time between pulse is $\tau_{pulse} = \tau_{pulse-width} + \tau_{pulse-gap}$. Since $\tau_{pulse-width} << \tau_{pulse-gap}$, we can comfortably say that $\tau_{pulse} \approx \tau_{pulse-gap}$. The macropulse duration of the RF wave ranges from 600 to 1000μ sec or 0.6 to 1 millisec respectively. Each

macropulse occurs at 1 to 5 Hz reprate.

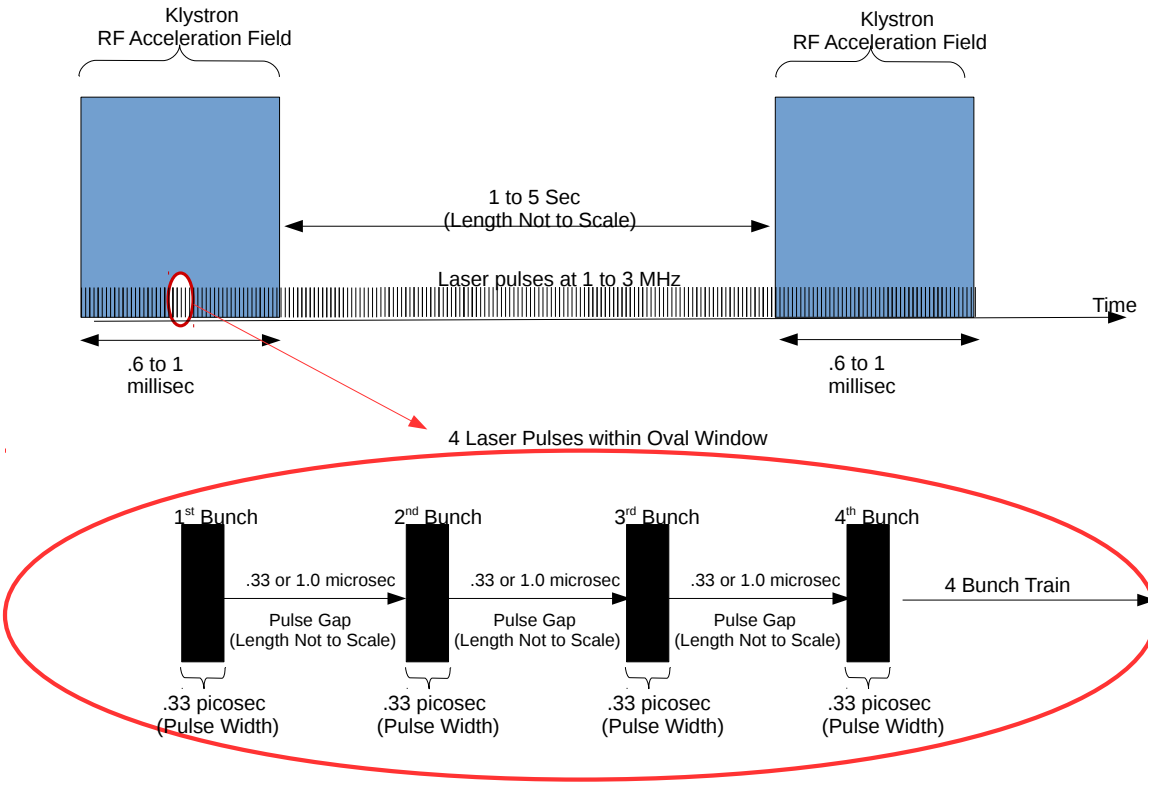

Figure 6.11: As the laser is generating pulses, the train of electron bunches are accelerated within a Klystron macro RF pulse. For a 1 millisec macropulse coupled with a 3 MHz laser, the maximum generated train of electron bunches would be 3000 with pulse gap of 0.33microsec between each bunch. This is then repeated again at 1 to 5 Hz reprate.

Figure 6.11 illustrate the mechanics in generating a train of bunches with each bunch separated by the defined pulse gap. In order to avoid pileup, the detector deadtime which is roughly $\tau_{dead} = 1.05 \times \tau_p$ must be less than the pulse gap, $\tau_{pulse-gap}$. Since peaking time τ_p is almost equal to τ_{dead}, we will use peaking time as the parameter to reduce both deadtime and pileup errors. If the pulse gap is 1μsec, then the peaking time must be less than 1μsec. For illustration purposes, we will choose a peaking time of $\tau_p = 0.5\mu$sec. Additionally, the deadtime is greater than a single

bunch interaction time with the crystal. The crystal is 169μ meters long and the bunch is traveling at approximately "c". The bunch's transit time through the crystal is 0.21 picosec. Therefore, a single bunch total interaction time with the crystal is approximately 0.54picosec = $\tau_{Pulse-width} + \tau_{interaction-time}$. During this 0.54 picosec, photons are generated from the bunch-crystal interaction primarily through Bremsstrahlung or Channeling Radiation. Even with an interaction time of .54picosec, it is 6 orders of magnitude smaller than the detector's deadtime/resolution time.

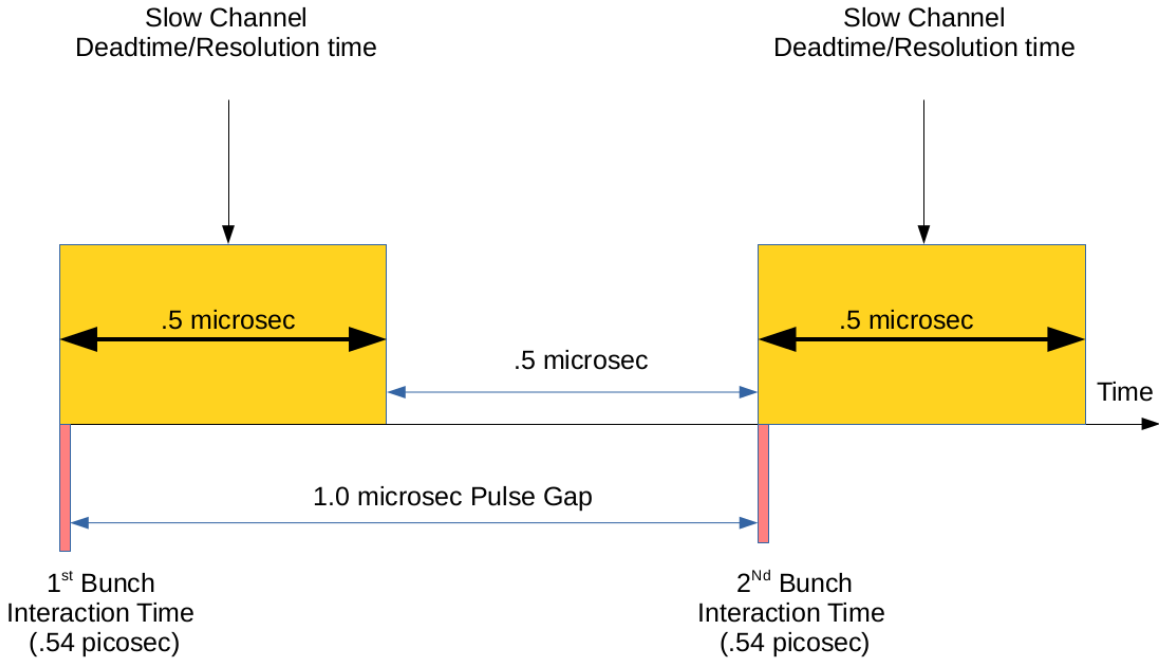

Figure 6.12: shows a train of two bunches interacting separately with the crystal. During the 1st bunch interaction with the crytstal, the interaction may generate photon or photons which triggers the detector to process the energy over the deadtime/resolution time interval of 0.5 μsec. After the 1st bunch interaction, no additional photons are generated until the 2nd bunch interacts with the crystal and the process starts all over again. With a laser of 1MHz, the pulse gap is 1μsec in this case.

Since the interaction time is 6 orders of magnitude smaller than the detector's deadtime, Figure 6.12 immediately shows that if a bunch generates more than one photon, then automatic pileup occurs. We call this automatic pileup. It is also clear that if the deadtime is greater than the pulse

gap, pileup will also occur. To eliminate these sources of pileup, the experiment must ensure that the peaking time is less than the pulse gap and that the number of electron's within the bunch is low enough to generate on average less than one photon per interaction. In addition, the detector does not receive any photons other than from the bunch interaction with the crystal.

Let us assume that under these accelerator conditions, each bunch will generate only one photon. If the reprate is 1 second with 240 bunch train within each macro RFpulse, then for a 300sec(5 min) run, the maximum number of photons detected should be 72,000 photon counts.

$$\text{Total Number Photons detected } (72K) = \left(\frac{1\,\text{photon}}{\text{Bunch}}\right)\left(\frac{240\,\text{Bunch}}{1sec}\right)300sec \tag{6.5}$$

However, if perhaps every bunch generated on average 3 photons per interaction, then the maximum number of photons detected and recorded will still remain at 72,000 in stead of the actual incoming photon count of 216,000. The three photons generated from a single bunch interaction would automatically pileup as just one photon measured by the detector.

This X123 CdTe detector has the ability to reject photons that arrive within the resolution time of the first photons arrival. The detector uses the Fast Channel with a resolution time of 120 nanosec. After a photon arrives at the detector, the fast channel detects the incoming photon count. The slow channel pulse shaper collects the photons induced charge and determines the energy of the photon. However, if a second photon arrives before the detector resolution time is completed, normally the slow channel will add this photon to the first photons signal and recorded it as pileup photon. Generally, the fast channel can eliminate this second photon early arrival. The fast channel detects the second photon and tells the detector to reject both the second and first photon's energy deposits if they are within the resolution time. The fast channel counts all incoming photons that arrive outside the fast channel's resolution time of 120 nanosec. This rejection of any photons that arrive within the slow channels resolution time is called pile up rejection (PUR) setting. If the PUR is on, the fast channel will trigger the rejection of any potential photons that would have pileup. With PUR on, the fast channel provides the incoming photons. The slow channel provides a count of only the photons that are accepted and used in the spectrum data.

In this experiment, the bunch interaction time is several orders of magnitude smaller than the fast channels resolution time. Consequently ,the bunch interaction time is less than both the Fast Channel and Slow channel resolution times. Because of this, in this experiment, the fast channel is not able to sift out the pileup photons. If the detector only receives photons from the bunch-crystal interaction, all the photons generated from a single bunch are automatically pileup and are considered by the detector as one photon. Therefore, assuming no photons are generated between the pulse gap, the the photon count for both the fast and slow channels should match exactly.

In order to generate sufficient number of photon counts and to avoid pileup for a viable spectrum, the accelerator must generate a large number of bunch interactions with the crystal and ensure that less than one photon on average is produced for each electron bunch.

Dark Current Considerations

Dark current generates significant background photons that will affect the fast count and slow count spectrum. During the Klystron's RF pulse which lasts one millisecond, dark current is accelerated down the beam pipe line. As the electrons are accelerated, some scrape the beam pipe itself and generate Bremsstrahlung radiation oriented down the beampipe and ultimately into the forward detector. In addition, the high emittance dark current interacts with the crystal and the thin brass that mounts the crystal onto the goniometer which also produces additional Bremsstrahlung into the forward detector. With a 1 MHz laser pulse, there is sufficient time for the detector to receive dark current generated photons between bunches. In addition, suppose the accelerator is set to only generate 20 bunches for each RF pulse. Then after the 20 bunch has has passed through the crystal, there still is 0.98 milliseconds remaining for the RF pulse to continue accelerating Dark Current into the crystal and mount which generates additional Bremsstrahlung radiation into the detector. Figure 6.12 and 6.13 illustrates the timing of this process.

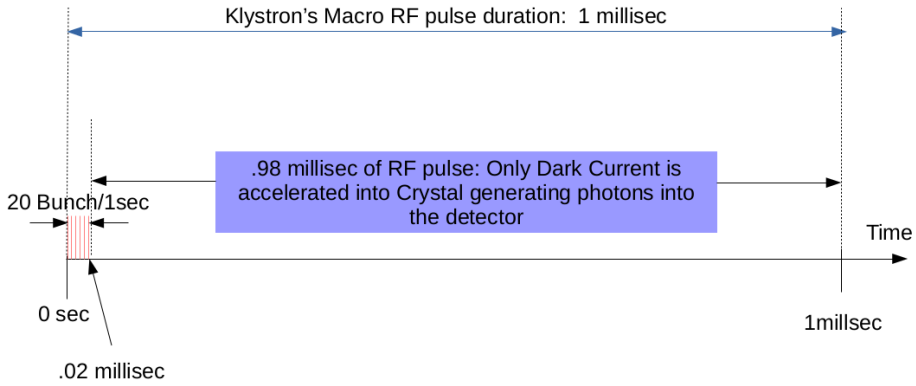

Figure 6.13: shows that after 20 bunch train generated within a one Klystron pulse has passed, there still remains 98 percent of the RF pulse to continue accelerating dark current into the crystal and crystal mount which generates Bremsstrahlung background photon counts.

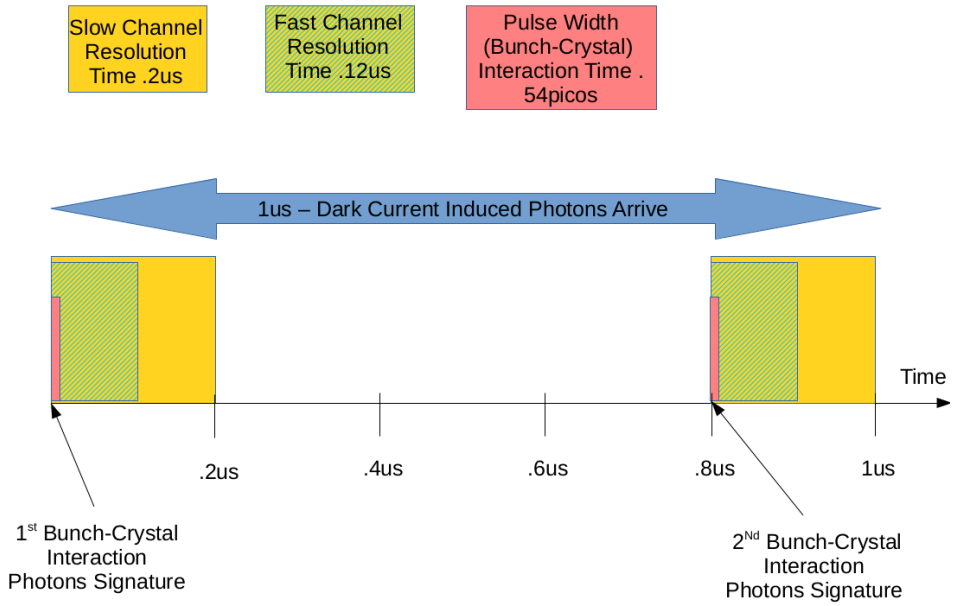

Figure 6.14: shows that between two bunches with a laser pulse gap of 1μ sec, there is also 1μ sec that dark current also generates bremstrahlung radiation into the detector.

We can see from Fig.6.13 and 6.14 that dark current could be the main contributor in generat-

ing Bremsstrahlung into the back ground spectrum signal. Efforts in this experiment were made to mitigate dark current contributions. Since a beam scraper was not installed in the chicane's beamline, the chicane was still used to reduce dark current. The dipole magnets within the chicane were used to manipulate the beam to slightly scrap along the beam pipe in order to reduce any beam halo as well as dark current contributions in generating Bremsstrahlung along the beamline. Since the chicane was not in-line with the forward detector, any Bremsstrahlung generated would miss the forward detector. For an acquisition time of 300 seconds, we were reducing the fast counts from approximately 2600 to 615 and sometimes even lower. However, we found that the dipole currents fluctuated throughout the experiment which caused fluctuation in the dark current which was not continuously measured. In addition, although the chicane's beamline was conveniently not in line with the forward detector, the Bremsstrahlung generated from the chicane was oriented towards the 90 degree detector. As a result, although shielding was placed to protect the detector from this radiation, it was not sufficient and thus the 90 degree detector was unusable for this experiment.

Detector Saturation

When too much energy is deposited into the detector due to excessive photon pileup, the detector's slow and fast channel outputs behave erratically. Too much energy deposited within the active detector volume creates a collected induced charge which may exceed the 2 Volts maximum input to the Detector's Analog Digital Converter (ADC)[36]. When the ADC input voltage is exceeded, the detector's outputs will be erratic and not reliable[36]. This study defines this condition as detector saturation. In particular, when the detector is in saturation, both the fast and slow channel's recorded photon counts should be erratic and unreliable.

As stated earlier, the fast channel primary function is to detect an incoming photon. Assume for purposes of illustration, that the detector detects photon $^{\#}1$ and then detects the second photon $^{\#}2$ some time later. When the fast channel detects the second photon, the detector's algorithm will determine whether the separation time exceeds the resolution time of the first photon's detection. If

the separation time between the second and first photon is less than the detector's resolution time, then the slow channel rejects both photons when PUR is on. In this scenario, the Fast Channel will record an output of two incoming photon counts. However, the slow channel will record an output of zero incoming photon counts. If PUR is set to off, the Fast channel will still record the two incoming photons. But, the slow channel will now record one incoming pileup photon instead of zero. Therefore, in an experiment, the fast channels should always be equal to or greater than the slow channel photon count.

In this study's experiment, other than photons generated from the bunch-crystal interaction, assume that no other photons are generated or present in the experiment area. Since all photons are generated from the bunch-crystal interaction within 54 picosec, these photons all arrive within the fast channels 120 nanosec resolution time. These bunch-crystal generated photons are automatically detector pileup photons. In addition, since each bunch separation time (pulse gap) is greater than the detector's resolution time, the detector will not reject any bunch-crystal generated photons. Whether the bunch generates one, two, five, twenty or 5000 photons, the fast channel will record the entire single bunch generated photons as one incoming pileup photon count.

If a pileup photon energy creates a detector saturation condition, then the fast channel may or may not record the incoming photons as a single count. AmpTek stated that in this condition, the fast channel's ability to properly record incoming pileup photons is unknown. Theoretical calculations for a bunch possessing 20 picocouloumbs, the bunch interaction with the crystal would generate over 1873 photons/bunch at 89.3KeV and 1767photons at 141.9KEV for a total of 3640 Photons/bunch. For the forward detector, at these photon numbers, saturation of the detector will most likely occur.

However, instead of being completely erratic and unpredictable when the detector is in saturation mode, the detector appears to consistently suppress the fast count numbers. Table 6.1 shows

fast count data generated from different bunch charge settings, 60 bunches per reprate and an acquisition time of 300 seconds. Table 6.1 shows that the detector is in saturation; and when in saturation it suppresses the fast count recordings. For example, suppose a 1pC bunch generates 0.5 photons on average when it interacts with the crystal. In this beam condition and interaction rate, the detector is not in saturation nor in an automatic pileup condition. In this case, we should expect 9,000 photons recorded in the fast count.

$$9000\,\text{photons} = \left(\frac{0.5\,\text{photon}}{\text{Bunch}}\right)\left(\frac{60\,\text{Bunch}}{1sec}\right)300sec \tag{6.6}$$

As we increase the bunch charge, we should expect the average count to increase. For example, lets hypothetically say at 37pC, the bunch interaction is generating on average 0.9 photons. We should then expect a fast count to increase to a total of 16,200 photons. Hypothetically, lets assume that at 63pC, each bunch interaction is generating 2 photons on average but the total energy of the two photons is insufficient to saturated the detector. In this situation, the two photons are automatic pileup and the detector records the sum of the two photon's energy as just one photon. In this case, the fast count should be at its maximum of 18,000. In all these cases, we are not seeing these performances within Table 6.1's data. In fact, as the charge increases in Table 6.1, we do not see any significant change in the fast counts; and in fact the fast count is significantly less then the maximum possible fastcounts of 18,000. The detector, therefore, must be in saturation mode and is on average consistently suppressing the fast counts. Table 6.1 indicates that the detector saturation is suppressing fast counts by 87.2% of the the maximum possible counts of 18,000.

Table 6.1: Detector Saturation Suppresses Actual Fast Count.

Diamond Lattice Crystal				
Bunch Charge	Duration	Bunch	Fast Counts	Predicted Fast Counts
1pC	300sec	60	2291	18,000
37pC	300sec	60	2285	18,000
63pC	300sec	60	2328	18,000
Aluminum Foil				
1pC	300sec	60	3228	18,000
35pC	300sec	60	2080	18,000
60pC	300sec	60	2059	18,000

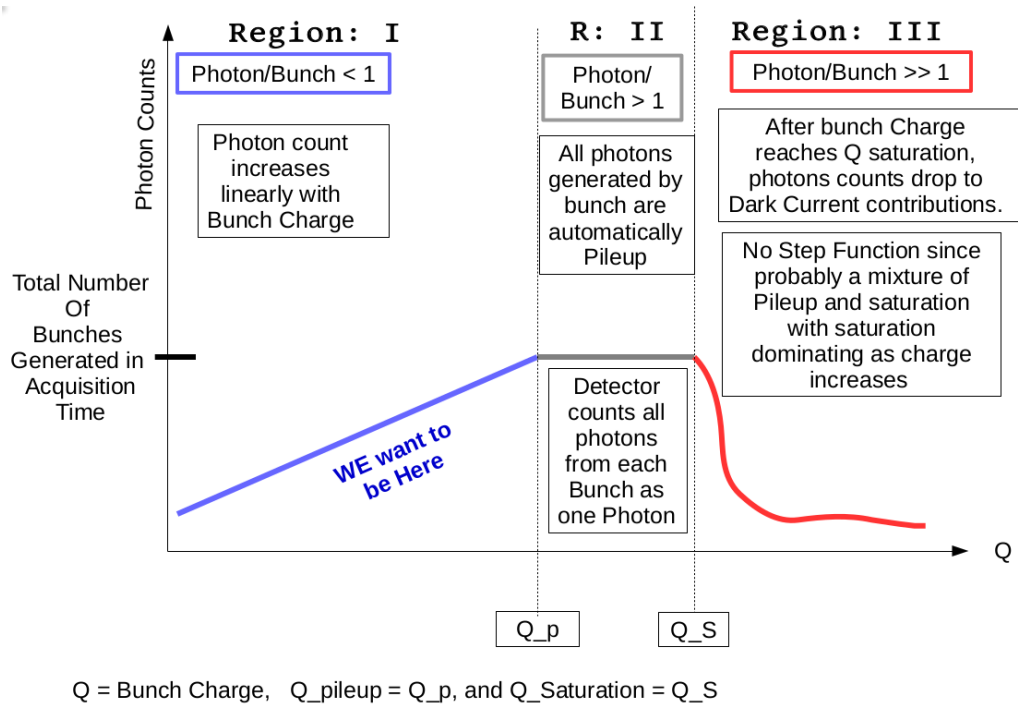

Figure 6.15: Detector's fast count vs bunch charge saturation curve.

Figure 6.15 outlines what is most likely occuring with the X123CdTe detector fast counts as the number of photon that are generated begin to approach and eventually go beyond the detector's saturation point. In Figure 6.15, Region I $\left\{Q < Q_{pileup}\right\}$ predicts a linear increase in fast counts as the bunch charge, Q, increases from zero charge to Q_{pileup} charge. Bunch charges at Q_{pileup} generate exactly one photon per bunch. At Q_{pileup}, the total number of fast counts is at its maximum for the detector. Region II $\left\{Q_{pileup} < Q < Q_{Saturation}\right\}$ predicts that the saturation curve flat lines to the number of photons equal to the total number of bunches produced during the acquisition time. Bunch charges above Q_{pileup} will generate, on average, more than one photon per bunch-crystal interaction. Since the photons generated from the bunch-crystal interaction are well within the fast channel's resolution time, these photons are automatically pileup photons. So long as the pileup photons do not exceed the ADC's 2 Volt limit, no matter how many photons that are generated, the detector will only record one photon per bunch. When the bunch charge is high enough for the pileup photons to deposit enough energy to exceed the ADC's 2 Volt limit, then the detector is in saturation mode. The bunch charge that generates enough photons, on average, to saturate the detector is called the $Q_{saturation}$ charge. Region III $\{Q_{Saturation} < Q\}$ represents drastic suppression of fast count for bunch charges above $Q_{Saturation}$.

Initial experimental results indicates that the detector fast count vs charge data agrees with Figure 6.15 detector saturation curve predictions. Figure 6.16 saturation curve plotted from experimental data nearly replicates the predicted curve illustrated in Figure 6.15 with some notable discrepancies.

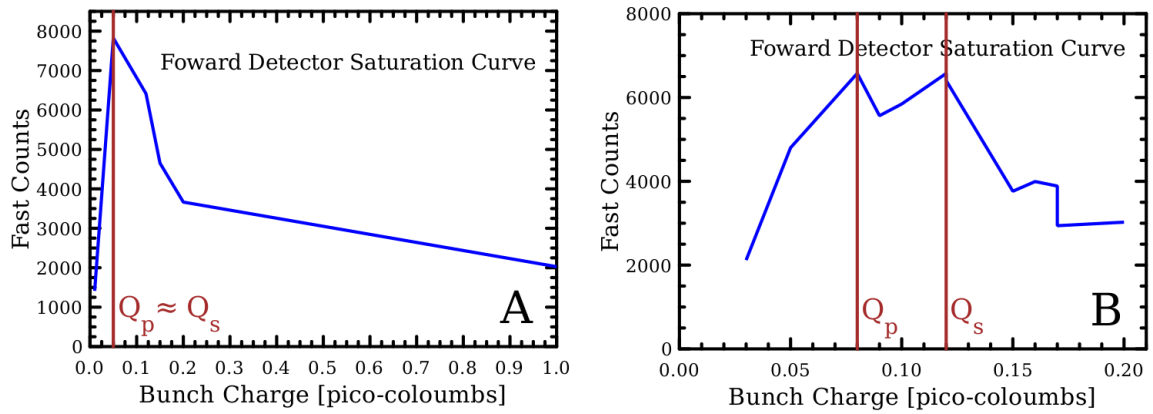

Figure 6.16: Plot "A" Forward Detector's saturation curve indicates at this charge resolution that $Q_p \approx Q_s$. Plot "B" shows experimental data with more refine charge resolution where $Q_p < Q_s$ as predicted. Acquisition time was 300 sec for both plots. 20 Bunches with reprate = 1 MHz for Plot B, unknown for Plot A

Both plots in figure 6.16 show a steady nearly linear rise to a charge pileup Q_p approximately somewhere between 0.05pC and .08pC bunch charge. In Fig.6.16B, after Q_p is reached, the fast counts appears to flatten out until we reach saturation charge $Q_s = 0.12$pC after which the fast counts are suppressed due to detector saturation. Although not recorded in Fig.6.16A, the number bunches per 1MHz reprate is 20 for Fig.6.16B. Therefore, for Fig.6.16B, we should expect a maximum of 6000 fast counts at the pileup charge,$Q_p = 0.08$pC. Instead, the fast counts are at 6576 which is a discrepancy of 576 fast counts in excess. In this calculation, Dark Current back ground signal were already removed from the fast count. However, it has been found, that dark current contributions to the fast count fluctuate over the run of the experiment which may account for this discrepancy. In addition, since the charge per bunch was operating at the extreme range of the FAST capabilities, charge error is evident but not measurable in this region.

Finally, as a last check on detector's predicted saturation curve, we measured the number of Fast counts generated per bunch. This is a great indicator on whether the bunch charge is in region I or II. If the bunch charge is in region III, we should have significant suppression of fast counts in the suppression range of 80% or more. In this check, three different laser frequencies were used: 3 MHz, 1 MHz, and 750 KHz. This in turn increased the pulse gap between bunches by

0.33μsec, 1μsec and 1.33μsec. All three experiments used the same bunch charge of 0.055pC which is approximately the Q_{pilup} charge as indicated in Fig. 6.16. During these three runs, dark current background contributions were removed from the Fast Count spectrum in Fig. 6.17.

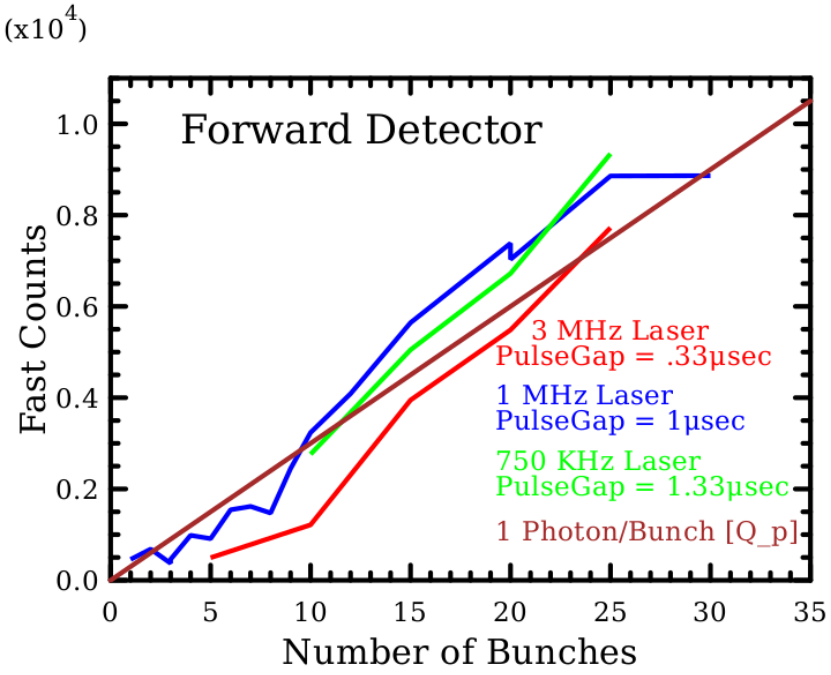

Figure 6.17: shows for a bunch charge of 0.055pC bunch $\approx Q_p$, fast counts were recorded as a function of number of bunches. Red curve depicts 3MHz pulse laser, blue curve is the 1MHz pulse laser, and the green curve represents 750Khz pulse laser. Since the forward detector's acquistion time for the spectrum was 300 sec and the reprate is 1Hz, the brown curve represents 300 fast counts/bunch which is equivalent to one photon generated per bunch-crystal interaction. Dark Current background was removed from this plot

From Figure 6.17, the actual curves for 1MHz and 750KHz Laser lies above the theoretical prediction of a one pileup photon generated per bunch-crystal interaction. These graphs lie approximately at the Q_{pileup} which is the transition point between Region I and II. Key is that there is no major suppression of fast counts, fast counts increase roughly linearly with bunch increase,

and the fast counts also roughly equal to number of total bunches generated in the acquisition time. Of note, as the pulse gap increases, the experimental curves positive error increases as well. The 3MHz curve shows better agreement with the theoretical max. In all three cases, there is no specific clear answer for why the as the pulse gap increases, there is more opportunity for dark current to inject photons into the detector. However, this is not the complete answer. If dark current was the sole source of error, we should see roughly the same error at 1 bunch as in 25 bunches per reprate. Determining the source of this error is still not fully understood. However, we can say that 0.055pC is still too high for executing the channeling experiment. Based on Fig.6.16 and Fig. 6.17, the analysis indicates fairly confidently that the bunch charge is at Q_{pilup} or some where in region II. To ensure that we are in region I, the charge must be reduced such that the curves lie consistently below the brown curve in Fig. 6.17. Unfortunately, since we are at the limits of physically collimating the forward detector, the accelerator is unable to lower the charge below $Q_p \approx$ 0.055pC consistently to conduct the channeling experiment using the forward detector.

Pileup and Deadtime Mitigation

Due the nature of how channeling photons are generated and detected in this experiment, this study can apply the algorithm developed by Y. Dannon, B. Sones and R. Block (DSB) to correct for pileup and deadtime errors in the spectrum[37]. For abbreviation purposes, this correction algorithm is designated as the DSB or DSB mitigation.

In order to apply DSB mitigation, the experiment must meet the following assumptions:

1) The detector resolving time is longer than the radiation's pulse width which means that only one photon can be be measured per pulse.
$\tau_{deadtime} > \tau_{pulse-width}$

2) The detector can fully recover and is ready to measure at the beginning of each radiation pulse which implies that detector resolving time must be shorter than the beam-off interval.
$\tau_{deadtime} < \tau_{pulse-gap}$

3) There is no measured background photons or noise in between the radiation pulses.

4) All Channeling radiation and Bremsstrahlung emissions follow the Poisson distribution.

For Poisson statistics, 'm' is defined as the average mean number of photons per X-ray pulse that can be detected by a detector with no dead time losses. No dead time losses means that no photon was loss due to deadtime. For the X123CdTe detector, deadtime losses can occur when the PileUp Rejection (PUR) is turned on. If the separation time of two arriving photons are less than the detector's deadtime $\approx$ peaking time, then both photons are not counted and are considered deadtime losses. The probability to detect 'n' photons during a single pulse is a function of the Poisson probability distribution.

$$P(n,m) = \frac{m^n e^{-m}}{n!} \tag{6.7}$$

Figure 6.18 displays a toy spectrum with four dominate peaks. This spectrum was generated stochastically.

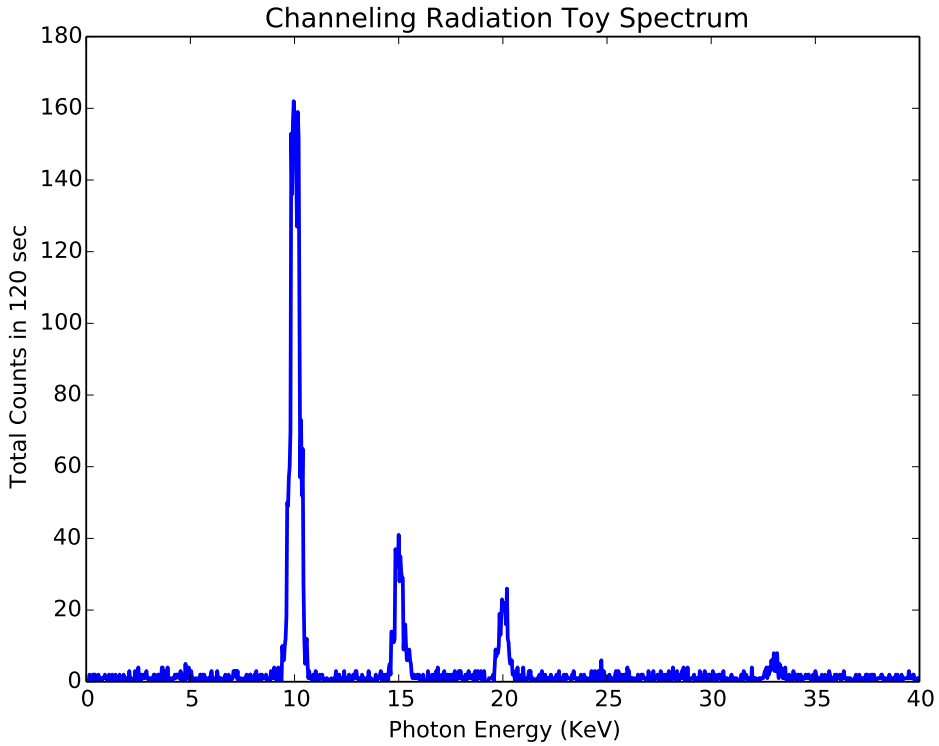

Figure 6.18: This artificially generated toyspectrum has Four Gaussian peaks and background noise.

In figure 6.18, the DSB algorithm can characterize each peaks photon detection and background count statistically. The probability of detecting one photon from Peak$^{\#}$1 and no background photons during a single pulse is

$$P_1 = P(1,m_1)P(0,m_b) = m_1 e^{-m_t} \tag{6.8}$$

where m_1 equals the average number of photons detected for Peak$^{\#}$1 with no dead time loss for a pulse. m_t equals the average total number of photons detected without loss to dead time for one pulse. Finally, $m_{b1} = (m_t - m_1)$ is the average background photon counts for Peak$^{\#}$1 without loss to dead time for one pulse. The probability to detect any photon without dead time loss during a single pulse is

$$P_t = 1 - P(0, m_t) \tag{6.9}$$

From these Poisson statistics, this DSB algorithm can define what the photon rates are for Peak$^{\#}$1 photons, total number of photon rates, and the actual rate.

Table 6.2: Observed and Actual Peak$^{\#}$1 and Total Photon Rates

Observed Rates	
r_1	$r_1 = fP_1 = fm_1 e^{-m_t}$: Observed Peak$^{\#}$1 photon rate in one second
r_t	$r_t = fP_t = f(1 - e^{-m_t})$: Observed total photon rate in one second.
Actual Rates	
n_1	$n_1 = fm_1$: Actual Peak$^{\#}$1 photon rate in one second.
n_t	$n_t = fm_t$: Actual total photon rate in one second.

where f is the laser pulse frequency. Since we can measure Peak$^{\#}$1's photon rate, (r_1), and the total photon rate, (r_t), we can determine the actual Peak$^{\#}$1's photon count, (n_1) and the actual total count, (n_t). In other words, we can take observed photon count rates and apply a deadtime correction factor to determine the actual photon count rates.

$$n_t = fm_t = fln\left(\frac{f}{f - r_t}\right) \tag{6.10}$$

$$n_1 = \left(\frac{f}{f - r_t}\right) r_1 \tag{6.11}$$

Therefore, the deadtime correction factor for Peak$^{\#}$1 is $\left(\frac{f}{f-r_t}\right)$.

In this particular toy spectrum scenario, Peak$^{\#}$3 is conveniently twice the energy of Peak$^{\#}$1. Two photons with energies of Peak$^{\#}$1 could arrive within a laser pulse and be counted as a single Peak$^{\#}$3 photon. This would be an automatic pileup. There also could be a Bremsstrahlung photon

plus a Peak#2 photon pileup equaling to Peak#3's energy. However, that is considered statistically unlikely. The probability of getting a photon count in Peak#3 is

$$P_3 = P(0, m_{b13})[P(2, m_1)P(0, m_3) + P(0, m_1)P(1, m_3)] \tag{6.12}$$

where $m_{b13} = m_t - m_1 - m_3$ is the average background photon count minus Peak#1 and Peak#3's photon counts. m_3 is the average number of photons detected for Peak#3 with no dead time loss for a pulse. To interpret $P(0, m_{b13})P(2, m1)P(0, m_3)$ in Equation 6.12, it is the probability of two photons from Peak#1, no photons from Peak#3, and no background photons arriving at the detector. Likewise, $P(0, m_{b13})P(0, m1)P(1, m_3)$ is the probability that no photons from Peak#1, one photons from Peak#3, and no background photons arrive at the detector.

Table 6.3: Observed and Actual Peak#3 Photon Rates

Observed Rates	
r_3	$r_3 = fP_3 = fe^{-m_t}\left(\frac{1}{2}m_1^2 + m_3\right)$: Observed Peak#3 Photon rate in one second
Actual Rates	
n_3	$n_3 = f\frac{r_3}{f - r_t} - \frac{1}{2}\left(\frac{r_1}{f - r_t}\right)^2$: Actual Peak#3 photon rate in one second.

From Table 6.3, the actual photon rates from Peak#3's n_3 equation is composed of the deadtime correction $\frac{r_3}{f - r_t}$ and the pileup correction $\frac{1}{2}\left(\frac{r_1}{f - r_t}\right)^2 = \frac{1}{2}m_1^2$.

The observed and actual photon rates for Peak#2 and Peak#4 have the the same form as depicted in Table 6.2 with the appropriate m_2 and m_3 average photons used instead.

DSB algorithm is tailored made for this experiment and should be used in adjusting the spectrum for both pileup and deadtime. In addition, in DSB study, they found that the average photon per bunch should not exceed $\frac{3}{4}$ per bunch. If this average is exceeded, the DSB algorithm errors begin to dominate.

6.1 Conclusion

There is a possibility for a second channeling experiment to be conducted at FAST. If this is the case, as originally planned, the 90 degree detector of the Compton scattering coupled with lead or brass collimation would lower the average number of bunches to less than one. Preferably, the 90 Degree detector should be position on the opposite side of the chicane to avoid both beam halo and dark current induced Bremsstrahlung radiation contamination. Likewise, the 90 degree detector should be heavily shielded from any other beam induced Bremsstrahlung upstream and from the beam dump. The positioning and shielding will ensure the rigid requirement that no photons arrive at the detector between pulse gaps. Using the Compton scattering disk, we should be able to reduce the average photons per bunch to less than 0.75 to meet the DSB algorithm requirement for adjusting for pileup and deadtime errors. This criteria also eliminates any possibility of automatic pileup, saturation or near saturation mode. Secondly, we now have an ability to characterize whether the X123CdTe is in saturation or not.

Chapter 7

Summary and Conclusion

In 2016 at the FAST/Fermilab facility, a collaborative group attempted to generate channeling radiation in the hard X-ray, 80 to 150 KeV region, using a 165 micron thick diamond crystal and a linear accelerator that is capable of generating almost 45 MeV beam energy. To predict the channeling radiation spectrum generated from a beam that is parallel to a [110] axial orientation or to a (110) crystal planar orientation, two models (2-D Axial and the 1-D Planar), have been used to predict axial and planar channeling radiation, respectively. Since Azadegan published excellent papers on 1-D Planar modeling for diamond, silicon, and germanium lattice along with publishing a working 1-D Planar Mathematica program to simulate planar channeling [4, 15, 26], the collaborative group chose to generate planar channeling radiation and use Azadegan's program with slight modifications [23] to numerically predict this planar channeling radiation. Although both the 1-D planar and 2-D axial models have had good agreement with their predictions with experimental results, this study believes that 1-D Planar model contains excessive approximations that could generate unphysical results. We believe that a 2-D model, such as the 2-D Axial model, is a much better approximation than any 1-D Planar model for any channeling radiation generated. But, we also are concerned that the 2-D Axial model's reliance on constructing single-string of ions continuum potential and the subsequent lattice potential construction also suffers from inadequate approximation errors and complexity. Therefore, the main focus in this research was to create

a 2-D Model that better reflects the actual physics and reduce the approximations which appear inherent in both the 1-D Planar and 2-D Axial model for predicting channeling radiation.

As discussed in chapter 4, the 1-D Planar model has excessive approximation and inconsistencies. The two dimensional Hamiltonian which describes the electron's transverse motion is strongly coupled. Consequently, information is lost or distorted when one of the degrees of freedom is averaged out unilaterally in the transverse space. As compared to our generic 2-D model or the 2-D Axial model, the number of eigenstates are severely reduced when using the 1-D Planar Model. This approximation is unnecessary and validity of this 1-D Planar model is suspect. In chapter 5.4, beam distribution f(p_x, p_y) has been shown to have great impact on the spectrum.

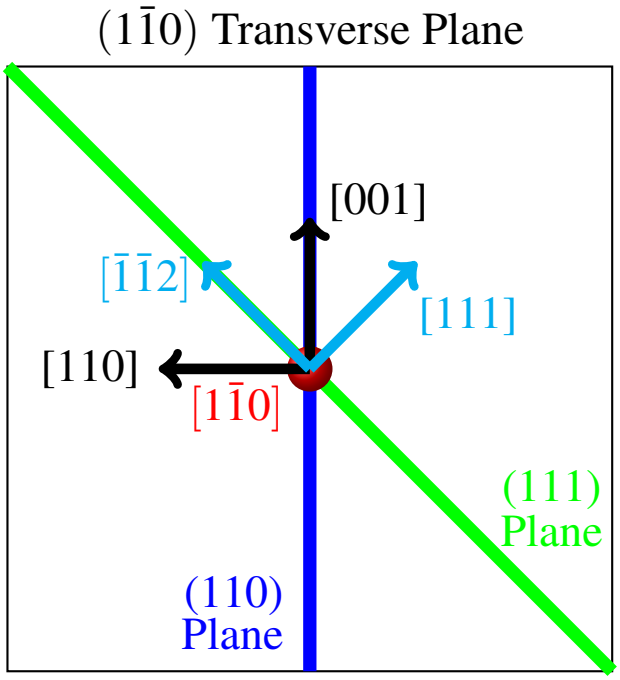

Figure 7.1: The square box represents the $(1\bar{1}0)$ transverse lattice plane which is the pancaked 3-D lattice due to Lorentz contraction along $[1\bar{1}0]$ axis. The beam $[1\bar{1}0]$, the red dot, is going into the page. Looking edgewise, the green line represents the (111) plane and the blue line represents the (110) plane. The beam $[1\bar{1}0]$ resides in both planes. As depicted in table 4.8 and 4.9, the two orthogonal axis, which are basis coordinates for the $(1\bar{1}0)$ Transverse Lattice plane, in this case is the $\vec{e}_x$ = [111] and $\vec{e}_y = [\bar{1}\bar{1}2]$; or it could be $\vec{e}_x$ = [110] and $\vec{e}_y = [001]$. For the (111) and (110) 1-D planar model, it averages out the coordinate axis $[\bar{1}\bar{1}2]$ and [001], respectively.

Suppose the beam has a round Gaussian distribution, in most cases with these small accelerator ex-

periments this is true, then the transverse momentum distribution is invariant under any coordinate system adopted within the beam's transverse plane. This invariance of the beam's transverse momentum distribution creates a problem for the experimenter. For example, what is the experimenter actually measuring in Fig. 7.1? In figure 7.1, the beam is traveling into the page with an axial direction $[1\bar{1}0]$. The transverse plane to this $[1\bar{1}0]$ beam is depicted as the square (the contracted cubic 3-D lattice to a 2-D lattice) where the transverse beam's motion resides within. The planes (111) and (110) are seen edgewise in this figure. The beam direction $[1\bar{1}0]$ resides in both planes which is where the two planes intersect. Since the distribution is invariant under any basis that spans the $(1\bar{1}0)$ transverse plane space, the distribution does not favor any particular coordinate axis system. Consequently, according to the 1-D Planar model, the electron beam is interacting simultaneously with the (110) plane and the (111) plane. Table 4.10 directly shows that the same beam direction [110], which is equivalent to $[1\bar{1}0]$, is generating 16.54 and 7.89 KeV X-rays peaks associated to the (110) planar model experiment and 11.07, 8.14 and 6.05 KeV X-rays peaks associated to (111) Planar model experiment. However, under this beam $[1\bar{1}0]$ direction, both experiments should be measuring all these X-ray spectrum signals simultaneously. This indicates inconsistency within this 1-D Planar model. Because of this excessive approximation and inconsistency within the 1-D planar model, this research focused on creating a new, generic 2-D model to be used in the FAST channeling experiment.

The 2-D Generic numerical model created in this research was an attempt to create a more accurate, less complex, and better phenomenological beam centric model than the existing 2-D Axial models.

Phenomenologically, the 2-D Generic Model made a clean break from the artificial construction of plane of ions or single-string of ions in explaining channeling radiation. Rather, the beam direction determines much of the physics of the problem. Along the beam direction, the three-dimensional lattice pancakes down into a two-dimensional transverse lattice plane. Within this transverse lattice plane resides the electron beam's transverse motion. Rather than artificially creating a lattice of single-string of ions, this approach looks at the contribution of each ion to the

lattice. Lorentz contraction allows us to readily determine any periodicity changes when transforming from a cubic 3-D lattice to a 2-D lattice plane. As illustrated earlier, determining the fundamental periodicity is absolutely critical in correctly solving the Schrödinger equation for this 2-D system. In addition, since the transverse motion lies within the transverse plane of the beam, one can also readily see the inconsistency with the 1-D Planar model (see Fig. 7.1). To expand further on a beam centric model, the lattice coordinates are rotated to align with the accelerator coordinates where z is the beam direction and the beam's transverse coordinates are x and y. When calculating the beam's occupation of eigenstates, the beam's emittance is used in lieu of the electron angle distribution around the critical angle [3]. Since accelerators are the primary drivers in generating relativistic electron beams, it makes sense to align the experimental measurements with accelerator coordinates and beam distribution emittance parameters. This also will provide a more standard approach in comparing channeling data produce from different facilities particularly since beam eigenstate occupation is dependent on both the beam emittance and Courant-Snyder's twiss parameters.

With the goal to make the 2-D Generic model more accurate than the 2-D Axial model, the new design also became less complex and thus more usable than the 2-D Axial approach. Although Lindhard's single-string of Ions was the initial impetus of channeling radiation, this construct is still an artificial configuration. Instead, this study followed along similar lines to Azadegan's development of the 1-D planar model[4] in developing the three dimensional lattice potential. In our Generic model and the Planar/Axial Models, both determined the ion's potential from electron scattering data of the ion[1, 2, 3, 5]. Based on each ion's location within each cubic lattice cell, we sum each ions contribution to generate a 3-D lattice cell potential. Then, without approximations, this study was able to sum exactly the contributions of all the lattice cells within a crystal lattice thus generating an overall lattice potential. This is an exact calculation of the lattice potential based on the ion's potentials. Now that the generic lattice potential has been determined, we then simply apply rotations to align the correct lattice orientation with the beam direction. In comparison, the 2-D Axial model development of the lattice potential is much more complex. Based on the single-

String of ions specific axial direction, each single-string located within a unit cell contributes to the overall unit lattice cells potential. Then, this technique must also sum the contributions of all the cell's potentials to generate the overall lattice potential. Although the steps are similar, in the 2-D Axial case, this model cannot apply rotation to its lattice potential to generate a new lattice potential based on a set of single-strings which lie along a different axial direction. Hence, since we can generate any lattice potential with ease, our generic model is less complex and can be applied in any orientation. In addition, our generic model should be more exact than the 2-D Axial model. Table 4.11 also clearly outlines the computational advantages that the 2-D Generic model has over the other two models. Surprisingly, as shown with the spectrum comparison in Figures (4.24, 4.25 and 4.26), the 2-D Axial model clearly predicts the channeling radiation spectrum much better than our Generic model. The question is why?

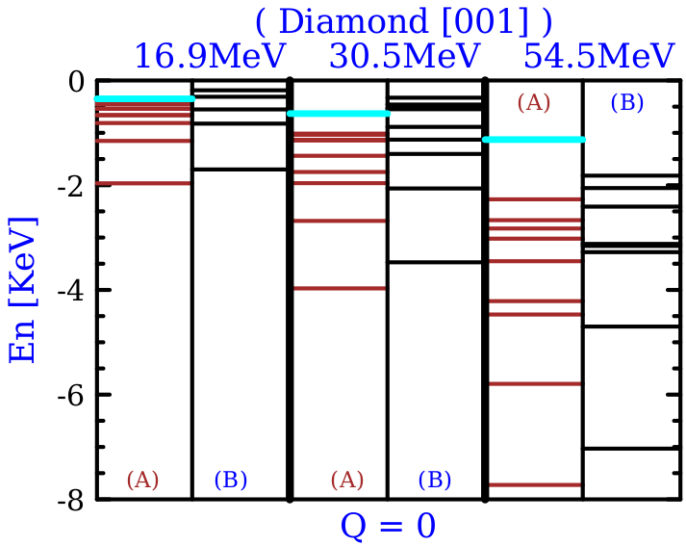

Figure 7.2: Visual comparison of Eigenenergies of our generic model depicted in red lines and Klein's predictions in black lines. For each beam energy 16.9, 30.5 and 54.5MeV, there are two columns: (A) and (B). Column (A) represents the Generic Model predicted eigenenergies in red lines. Column (B) is Klein's Axial Model's predicted eigenergies in black lines. $Q_1 = Q_2 = 0$ of the transverse motion in the beam rest frame diamond lattice along [001]. All Eigenenergies below the cyan line are bounded states.

One major contributor to our model not matching with measured results is the beam configu-

ration. Beam configuration can significantly impact on the probability that the beam will occupy a bound state or states. None of the experiments, where we compared our results with real experimental data, indicated what the experiment's beam configuration was. This omission of a key parameter's of beam emittance and twiss parameters certainly can skew how the spectrum is generated.

Since a rigorous error analysis was accomplished with the diagonalization of the Hamiltonian matrix, we are confident that this is not a source of the inconsistencies. The primary indicator of inconsistencies are the eigenenergy values for the bounded eigenstates. Table 4.3 and Figure 7.2 clearly illustrate that the transition energies, $\Delta E_{n,m} = E_n - E_m$ are not the same between Klein's 2-D Axial Model and our 2-D Generic model. However, there is a definite pattern that is common for both models. In all three energy cases depicted in Fig. 7.2, there is a distinct separation between E_1, E_2, and E_3 in both models. In addition, in both models, E_3 and E_4 separations are very close. This type of similarity is also consistent at higher eigeneneriges. Since solving for the eigenstates is not the problem, this disparity in eigenenergy separations indicates that the construction of the 2-D Generic potential is significantly different than the 2-D Axial model. Therefore, assuming beam emittance structure is not the source of the error, the most likely source of the discrepancy is the construction of the 2-D Generic potential.

a. Impact of using different fitting parameters for the scattering amplitude.

This study is using Doyle-Turner's fitting parameter of the electron scattering amplitude of the ions: carbon, silicon, and germanium [8]. Azadegan used Doyle-Turners fit data [4]. Andersen's paper used a four Gaussian better fit than the Doyle-Turner's four Gaussian fit parameters [1]. Genz used an improved fit of the numerical results of Doyle-Turner [5]. Using X-ray diffraction to determine the contribution of electrons, Klein used this information to apply corrections to the Doyle-Turner fit parameters [2]. Finally, Chouffani used a six Gaussian to improve the fit of the electron scattering amplitude [3]. In comparing our spectrum to data, we used Klein, Genz, and Andersen's published data. All three authors used a different scattering amplitude fit parameter

than our 2-D Generic model. Since we do not have these parameters, we will use Chouffani's improved six Gaussian fit parameters to measure how these new fit parameters perturb our 2-D Generic eigenenergies.

	16.9 MeV		30.5 MeV		54.5 MeV	
	Ch	DT	Ch	DT	Ch	DT
E_1	-59.82	-59.38	-67.42	-66.53	-73.89	-72.437
E_2	-34.64	-34.88	-44.52	-44.93	-54.00	-54.33
E_3	-24.87	-24.58	-33.29	-32.86	-42.18	-41.91
E_4	-20.10	-20.11	-29.14	-29.29	-39.01	-39.52
E_5	-19.95	-19.94	-24.14	-24.09	-32.66	-32.37
E_6	-16.25	-16.35	-19.24	-19.19	-28.24	-28.32
E_7	-13.99	-13.90	-19.04	-18.98	-26.68	-26.51
E_8	-12.15	-12.19	-17.22	-17.37	-24.95	-25.01
E_9	-11.85	-11.85	-16.85	-17.00	-21.31	-21.28

Table 7.1: This table displays the eigenenergies for the Diamond [001] 2-D Generic model at three different beam energies: 16.9, 30.5, and 54.5MeV. The rows define the eigenstate E_n. The columns define the fitting parameters used. "Ch" represents Chouffani's six Gaussian fit parameters of the electron scattering amplitude. "DT" represents Doyle-Turner's four Gaussian fit parameters.

Table 7.1 indicates that the Chouffani's fit parameters does not significantly perturb the eigenstates from the Doyle-Turner generated eigenstates. As a quick check, the lab frame's maximum and minimum potentials for Chouffani's fit is -10.735eV and -98.848eV. The labframe's maximum and minimum potential for the Doyle-Turner fit is -10.583eV and -93.477eV. This indicates that using the Chouffani fit for the diamond increases the depth of the potential. Preliminary data indicates that these fitting parameters do not have any significant impact on the Eigenenergy distributions. However, we should also examine silicon and germanium to determine whether this

consistent as well with these lattices.

b. Comparison of Labframe's Potential: Klein's 2-D Axial versus Our 2-D Generic

Klein Diamond [001] labframe 2-D Axial potential, using a different fitting parameters than Doyle-Turner, has a maximum potential of approximately 0eV and a minimal potential of approximately 86.5eV. Our potential has a much shallower minimum of -10.583 and a deeper maximum of -93.477eV. In addition, as discussed earlier, our Fourier expansion converges much slower for [110] and [111] compared to the 2-D Axial model. Yet, for the [001] case, our Fourier expansion converges faster than the 2D axial model. Consequently, this difference in Fourrier convergence rate indicates sufficient difference between the legacy 2-D Axial potential and this research 2-D Generic potential. This reinforces the idea that the 2-D Generic potential is still the main source of the discrepancy.

Conclusion

Assuming that the beam emittance structure is not the source for the lack of agreement in prediction of data, this 2-D Generic model's inadequate predictions is most likely due to the construction of its potential. From a physics perspective, the construction of the lattice potential is based on fundamental principles. Each ion provides is own contribution to the lattice cell and subsequently towards the overall lattice potential. Although unlikely, linebroadening contributions were not calculated in this study. Linebroadening corrections would not likely rectify the current deficiencies in this model's ability to generate the correct spectrum. Although it may not be the ultimate source of the problem, the next step would be to perturb the electron's scattering amplitude fit parameters to determine if this improves the comparison of the eigenenergies between the two models. If this does improve the model's performance, then a better fit of the scattering amplitude should be determined. Second, we should generate a three-dimensional error surface plot describing the error between the 2-D Axial and our 2-D Generic Potential. Depending on the

results, if the error indicates that our potentials are consistently deeper than the 2-D Axial, then perhaps there is some screening mechanism of the ion occurring within the lattice cell which is being suppressed in our model. This 2-D Generic model's lack of agreement to data is puzzling. Solving this discrepancy should shed more light into the physics of channeling radiation.

References

[1] J. Andersen, E. Bonderup, E. Laegsgaard, B. Marsh, and A. Sørensen, "Axial channeling radiation from MeV electrons," *Nuclear Instruments and Methods in Physics Research*, vol. 194, no. 1-3, pp. 209–224, 1982.

[2] R. Klein, J. Kephart, R. Pantell, H. Park, B. Berman, R. Swent, S. Datz, and R. Fearick, "Electron channeling radiation from diamond," *Physical Review B*, vol. 31, no. 1, p. 68, 1985.

[3] K. Chouffani and H. Überall, "Theory of low energy channeling radiation: application to a germanium crystal," *physica status solidi (b)*, vol. 213, no. 1, pp. 107–151, 1999.

[4] B. Azadegan, *Investigation of Planar Channeling Radiation on Diamond and Quartz Crystals at Electron Energies between 14 and 34 MeV and Probing the Influence of Ultrasonic Waves on Channeling Radiation*. PhD thesis, Technical University Dresden, 2007.

[5] H. Genz, L. Groening, P. Hoffmann-Stascheck, A. Richter, M. Höfer, J. Hormes, U. Nething, J. Sellschop, C. Toepffer, and M. Weber, "Channeling radiation of electrons in natural diamond crystals and their coherence and occupation lengths," *Physical Review B*, vol. 53, no. 14, p. 8922, 1996.

[6] "The FAST Facility Image Galleries."

[7] *Amptek Inc. - Dectector Efficiency FAQ*.

[8] P. Doyle and P. Turner, "Relativistic Hartree–Fock X-ray and electron scattering factors," *Acta Crystallographica Section A: Crystal Physics, Diffraction, Theoretical and General Crystallography*, vol. 24, no. 3, pp. 390–397, 1968.

[9] K. Chouffani, H. Überall, H. Genz, P. H. Stascheck, U. Nething, and A. Richter, "Low energy channeling radiation experiments in a germanium crystal," *Nuclear Instruments and Methods in Physics Research Section B: Beam Interactions with Materials and Atoms*, vol. 152, no. 4, pp. 479–493, 1999.

[10] D. S. Gemmell, "Channeling and related effects in the motion of charged particles through crystals," *Reviews of Modern Physics*, vol. 46, no. 1, p. 129, 1974.

[11] "Jefferson Lab Free Electron Laser."

[12] "Five Years of Illumination: SLAC's Linac Coherent Light Source."

[13] V. Baryshevsky, K. Batrakov, I. Feranchuk, A. Gurinovich, A. Grubich, A. Lobko, A. Rouba, B. Tarnopolsky, P. Safronov, V. Stolyarsky, *et al.*, *Experiments with Parametric X-Ray Radiation (PXR) from Non-Relativistic Electrons*. 2005.

[14] J. Lindhard, "Influence of crystal lattice on motion of energetic charged particles.," *Kgl. Dan. Vidensk. Selsk., Mat.-Fys. Medd., 34: No. 14, 64p (1965).*, 1965.

[15] B. Azadegan, "A Mathematica package for calculation of planar channeling radiation spectra of relativistic electrons channeled in a diamond-structure single crystal (quantum approach)," *Computer Physics Communications*, vol. 184, no. 3, pp. 1064–1069, 2013.

[16] J. Andersen, K. Eriksen, and E. Laegsgaard, "Planar-channeling radiation and coherent bremsstrahlung for MeV electrons," *Physica Scripta*, vol. 24, no. 3, p. 588, 1981.

[17] J. Andersen, E. Bonderup, and R. Pantell, "Channeling radiation," *Annual Review of Nuclear and Particle Science*, vol. 33, no. 1, pp. 453–504, 1983.

[18] R. Shankar, *Principles of quantum mechanics*. Springer Science & Business Media, 2012.

[19] J. D. Jackson, *Electrodynamics*. Wiley Online Library, third ed., 1999.

[20] M. P. Hobson, G. P. Efstathiou, and A. N. Lasenby, *General relativity: an introduction for physicists*. Cambridge University Press, 2006.

[21] C. Kittel, *Introduction to Solid State Physics*. John Wiley & Sons, eigth ed., 2005.

[22] C. Sanderson and R. Curtin, "Armadillo: a template-based C++ library for linear algebra," *Journal of Open Source Software*, vol. 1, no. 2, pp. 26–32, 2016.

[23] T. Sen and C. Lynn, "Spectral brilliance of channeling radiation at the ASTA photoinjector," *International Journal of Modern Physics A*, vol. 29, no. 30, p. 1450179, 2014.

[24] R. A. Carrigan Jr, "Phenomenological summary of dechanneling in aligned single crystals," tech. rep., 1987.

[25] V. Bazylev, V. Glebov, and V. Goloviznin, "Quantum theory of inelastic scattering of negatively charged particles in oriented crystals," *Zh. Eksp. Teor. Fiz*, vol. 91, pp. 25–36, 1986.

[26] B. Azadegan, W. Wagner, and J. Pawelke, "Dependence of the linewidth of planar electron channeling radiation on the thickness of the diamond crystal," *Physical Review B*, vol. 74, no. 4, p. 045209, 2006.

[27] M. Reiser, *Theory and design of charged particle beams*. John Wiley & Sons, 2008.

[28] S.-Y. Lee, *Accelerator physics*. World Scientific Publishing Co Inc, 2004.

[29] E. Wilson and E. J. Wilson, *An introduction to particle accelerators*. Clarendon Press, 2001.

[30] P. Piot, V. Shiltsev, S. Nagaitsev, M. Church, P. Garbincius, S. Henderson, and J. Leibfritz, "The Advanced Superconducting Test Accelerator (ASTA) at Fermilab: A user-driven facility dedicated to accelerator science\ & technology," *arXiv preprint arXiv:1304.0311*, 2013.

[31] "Conversation with Daren Crawford on June 28, 2016," June 2016.

[32] *Amptek Inc. - DP5 Programmers Guide Rev. A4*.

[33] D. Mihalcea, C. Bohn, B. Terzić, M. Conde, and C. Eyberger, "Multiresolution simulations of photoinjectors," in *AIP Conference Proceedings*, vol. 877, pp. 220–226, AIP, 2006.

[34] G. F. Knoll, *Radiation detection and measurement*. John Wiley & Sons, fourth ed., 2010.

[35] *Amptek Inc. - X-123 User Manual Rev A0, X-123 Complete X-Ray Spectrometer with CdTe Detector, User Guide and Operating Instructions*.

[36] "Email from Bob Redus dated June 27, 2016," June 2016.

[37] Y. Danon, B. Sones, and R. Block, "Dead time and pileup in pulsed parametric X-ray spectroscopy," *Nuclear Instruments and Methods in Physics Research Section A: Accelerators, Spectrometers, Detectors and Associated Equipment*, vol. 524, no. 1, pp. 287–294, 2004.

Appendix A

Determining Schrödinger Equation's Eigenstates with Rotationally Symmetric Potentials

Solving for eigenstates with Schrödinger Equations possessing rotationally symmetric potentials is done through separation of variables techniques. For a three dimensional rotationally symmetric potential $V(r,\theta,\phi)$, the solution takes the form of

$$\Psi(r,\theta,\phi) = R(r)Y(\theta,\phi) \text{ where } r \in [0,\infty),\ \theta \in [0,\pi), \text{ and } \phi \in [0,2\pi) \tag{A.1}$$

Similar but not exactly like the spherically symmetric three dimensional potential, the two dimensional cylindrical potential takes the form of $V(r,\phi) = V(r)$ Using separation of of variables,

$$\Psi(r,\phi) = R(r)Y(\phi) \text{ where } \phi \in [0,2\pi) \tag{A.2}$$

we solve for the two dimensional Schrödinger equation, $\mathscr{H}$.

$$-\frac{\hbar^2}{2m}\left[\frac{1}{r}\frac{\partial}{\partial r}\left(r\frac{\partial}{\partial r}\right)+\frac{1}{r^2}\frac{\partial^2}{\partial\phi^2}\right]\Psi_n(r,\phi)+V(r)\Psi_n(r,\phi) = E_n\Psi_n(r,\phi) \tag{A.3}$$

where the solution is

$$\Psi_n(r,\phi) = \mathscr{R}_n(r,l)e^{il\phi} \text{ where } Y(\phi) = e^{il\phi} \tag{A.4}$$

From Eqn. A.4, the probability density for all eigenstates is independent of the rotational angle ϕ.

$$|\Psi_n(r,\phi)|^2 = |\Psi_n|^2(r) = \mathscr{R}_n(r,l)^*\mathscr{R}_n(r,l) \text{ Probability Density} \tag{A.5}$$